The Pennsylvania State University
The Graduate School

DESIGN, ANALYSIS, AND TESTING OF LEADING-EDGE PROTECTION TAPES FOR WIND TURBINE BLADES

A Thesis in
Aerospace Engineering
by
Desirae Major

Submitted in Partial Fulfillment
of the Requirements
for the Degree of

Master of Science

May 2019

The thesis of Desirae Major was reviewed and approved* by the following:

Jose Palacios
Assistant Professor
Thesis Co-Advisor

Sven Schmitz
Associate Professor
Thesis Co-Advisor

Amy Pritchett
Department Head of Aerospace Engineering

*Signatures are on file in the Graduate School.

Abstract

One of the sources of wind turbine blade damage is erosion of the surface at the leading edge. Depending on the location, wind farms are exposed to various environmental hazards. The impact of particles such as sand or rain at the blade leading edge during operation erodes the surface over time. High rotational speeds and a high impact count make the leading edge at the outboard 40% of the blade the most susceptible to severe damage. Besides posing structural concerns, leading-edge erosion degrades the aerodynamic performance of the blades by notably decreasing lift and increasing profile drag. Aerodynamic degradation of eroded blades results in notable annual energy production (AEP) losses for utility-scale wind turbines. To avoid these losses and protect the blades, leading-edge protection (LEP) tapes have so far proven to be a reliable and affordable solution. Tapes impact AEP as well, though losses are notably smaller than those for eroded blades. The mechanisms that degrade rotor performance when LEP tape is applied is not, however, a well-studied phenomenon for utility-scale wind turbines.

Research was conducted in conjunction with 3M, an industry leader in LEP tapes, to identify the performance degrading mechanism and develop new tape designs that minimize the impact of LEP tapes on wind turbine AEP. Cross-sectional parameters of the LEP tape such as maximum thickness at the center of the tape, width of the maximum thickness, minimum height of the backward-facing step at the tape edge, and taper angle from the maximum thickness to the minimum height are varied. Numerical CFD models are developed to estimate the effect of both standard and new tape designs on lift, drag, and c_l/c_d for a NACA 64-618 airfoil, a common wind turbine tip section airfoil. With transition modeling included, CFD predicts that the performance of LEP tapes compared to a clean airfoil is independent of height and width of maximum thickness, but is controlled by the height of the backward-facing step. Standard LEP tapes, with a backward-facing step height of 350 μm or 500 μm, increase drag 40% to 115% and

decrease c_l/c_d by 25% to 55% relative to a clean airfoil. For tapered LEP tapes, with a 75 μm backward-facing step height by comparison, drag increases 1% to 15% and c_l/c_d decreases only 5% to 10% compared to a clean airfoil. CFD models predict that below a certain backward-facing step height the boundary layer does not trip, minimizing the aerodynamic degradation compared to a clean 2-D airfoil.

Two tapered LEP tape designs are manufactured by 3M for experimental verification on a full-scale chord model at Re = 1x10^6, 2x10^6, and 3x10^6, and at $\alpha = 0°$. Wake probe measurements of profile drag show a 50% and 80% increase in profile drag for a 350 μm and 500 μm backward-facing step, respectively. Comparatively, a prototype tapered LEP tape with a 75 μm backward-facing step increased the profile drag of the full-scale chord model by 30%, though oil visualization of the flow over the model revealed that - when applied cleanly - tapered LEP tapes do not transition the boundary layer at the tape step.

A critical transition criterion for the backward-facing step of a LEP tape is determined from experimental data using the method of Knox and Braslow. Using experimental data for a 350 μm backward-facing step, the critical roughness height Reynolds number required for premature boundary-layer transition at the backward-facing step height is estimated to be $Re_{k,crit} = 200$. The computed local roughness height Reynolds number at the height of the backward-facing step for a tapered LEP tape falls well below the critical transition criterion for the range of free-stream Reynolds numbers observed along the span of a representative 1.5 MW utility-scale wind turbine rotor blade.

The wind turbine design and analysis code XTurb-PSU is used to predict the power output of a representative utility-scale 1.5 MW wind turbine with the various LEP tape designs applied to the rotor to estimate how the impact on wind turbine AEP changes by tapering the cross-section of LEP tapes. Under eroded conditions, notable lift decreases and profile drag increases result in a 5% AEP decrease compared to a clean rotor. Applying a standard LEP tape improves AEP output, though AEP still decreases by 2% to 3%, for a 350 μm and 500 μm backward-facing step height respectively. By tapering LEP tapes and reducing the height of the backward-facing step to 75 μm, AEP loss due to tape application is eliminated for a representative 1.5 MW pitch-controlled wind turbine rotor. Examining the trend of percent change in AEP versus average percent change in profile drag, AEP decreases linearly with increasing profile drag in the range examined in this work. Even for damaged tapered LEP tapes, the experimentally observed 30% increase in profile drag is predicted to result in only a 1% decrease in AEP compared to a clean rotor, still less than half the AEP loss associated with standard LEP tapes on the market today.

Table of Contents

List of Figures **vii**

List of Tables **xii**

List of Symbols **xiii**

Acknowledgments **xvi**

Chapter 1
Literature Review **1**
1.1 Introduction 1
1.2 Wind Turbine Leading-Edge Erosion 3
1.2.1 Particle Impact and Damage Mechanics 3
1.2.2 Observed Leading-Edge Erosion 12
1.3 Aerodynamics of Rough Surfaces 15
1.4 Aerodynamic Impact of Eroded Wind Turbine Blades 23
1.5 Leading-Edge Tapes for Erosion Protection 30
1.5.1 Leading-Edge Protection Materials 30
1.5.2 Aerodynamics of Leading-Edge Protection Tapes 33
1.6 Thesis Objectives 39
1.7 Chapter Summaries 40

Chapter 2
Numerical Modeling of Leading-Edge Protection (LEP) Tape Performance **41**
2.1 Baseline Airfoil Selection 41
2.2 Computational Method and Domain 43
2.2.1 Grid Verification 44

2.3 Design Matrix for Parametric Study of LEP Tapes 47
2.4 Analysis of Tape Designs 50
2.4.1 Tape Grid Verification 50
2.4.2 Aerodynamic Performance of LEP Tapes 53
2.4.2.1 Lift, Drag, and c_l/c_d 53
2.4.2.2 Pressure Coefficient Plots 58
2.5 Transition Modeling 61
2.5.1 Grid Refinement for Transition Cases 63
2.5.2 Aerodynamic Performance with Transition 65
2.5.2.1 Velocity, Pressure Distributions, and Intermittency 65
2.5.2.2 Transition Pressure Coefficient Plots 69
2.5.2.3 Lift, Drag, and c_l/c_d 71

Chapter 3
Verification of Numerical Models **75**
3.1 Experimental Verification 75
3.1.1 Wind Tunnel 76
3.1.2 Wake Probe 76
3.1.3 Full-Scale Chord Model 77
3.1.4 Testing Procedure 80
3.1.5 Results 83
3.2 Critical Roughness Height Model 87

Chapter 4
Impact on Annual Energy Production of a Wind Turbine **93**
4.1 Wind Turbine Definition 93
4.2 Power Estimates 96
4.2.1 Clean Baseline 96
4.2.2 Eroded Blades 97
4.2.3 Tape Performance 101

Chapter 5
Conclusion and Future Work **105**

Bibliography **111**

List of Figures

1.1 Local collection efficiency definition [1] 4
1.2 Variation in particle trajectory with size. [1] 4
1.3 Variation in local collection efficiency with particle size. [2] 5
1.4 Local collection efficiency variation with airfoil profile [1] 6
1.5 Local collection efficiency variation with local angle of attack [1] . . 6
1.6 Change in local collection efficiency with air flow velocity [3]. 7
1.7 Change in local collection efficiency with airfoil chord length [3]. . . 7
1.8 Normalized particle impact count for a wind turbine blade, pressure side (left) and suction side (right) [4]. 8
1.9 Variation in local collection efficiency along the span of a wind turbine blade [4]. 9
1.10 Local collection efficiency at the tip of a wind turbine blade [3]. . . 9
1.11 Normalized damage count for **a)** the NREL 5 MW blade, pressure surface (left) and suction surface (right) [4], and **b)** an optimized blade, suction surface (left) and pressure surface (right) [5]. 11
1.12 Examples of observed leading-edge erosion over the lifetime of a utility-scale wind turbine blade [6]. 12
1.13 Front view of the progression of leading-edge erosion on a wind turbine blade [7]. 13
1.14 Depiction of the chord-wise extent of each stage of leading-edge erosion on the upper surface of a blade [8]. 14
1.15 Stages of a boundary layer transition from laminar to turbulent [9]. 17
1.16 Critical transition Reynolds number as a function of roughness location [10]. 19
1.17 Variation in minimum drag coefficient versus roughness height for subsonic flow [11]. 19
1.18 Pressure coefficient distribution around an airfoil under clean and two roughness conditions at Re = $0.43 \text{x} 10^6$ (left) and $1.3 \text{x} 10^6$ (right) [12]. 20

1.19 Variation in lift coefficient with angle of attack and Reynolds number [13]. 21
1.20 Power curves for clean and rough conditions of a 1 MW wind turbine [14]. 22
1.21 Lift coefficient for a clean and rough airfoil with 3-D effects included [15]. 22
1.22 Sample pitting erosion pattern [16]. 23
1.23 Effect of pits of various sizes, h, on c_l/c_d [16]. 24
1.24 Effect of pit size, h, on the velocity field around an airfoil: (a) h = 0.1mm and (b) h = 1.5mm [16]. 24
1.25 Effect of pit density, l, on (a) c_l and (b) c_d [16]. 25
1.26 Example delamination of the leading edge of a NACA 64-618 airfoil [17]. 25
1.27 Lift and drag polars for the NACA 64-618 under clean, rough, and eroded conditions [17]. 26
1.28 Wind turbine power curves for various blade conditions [17]. 27
1.29 Degradation of AEP and revenue lost for rough or damaged wind turbine blades [17]. 27
1.30 Effect of erosion on normalized lift and drag versus angle of attack for (a) Stage 1 erosion and (b) Stage 5 erosion [7]. 28
1.31 Measured effect of (a) Type A, (b) Type B, and (c) Type C leading-edge erosion on lift and drag of the DU 96-W-180 airfoil [8]. 29
1.32 Sample tape coverage on the DU 96-W-180 for x/c = 30% upper surface and x/c = 20% [18]. 33
1.33 Effect of LEP tape on Cl and Cd for a fixed lower surface and varying upper surface tape extent [18]. 34
1.34 Effect of LEP tape on airfoil lift and drag performance [18]. 35
1.35 Different tape configurations studied by Giguere and Selig [19]. 36
1.36 Loss of $C_{l,max}$ for the SG6042 airfoil for one or two layers of tape and as a function of Reynolds number [19]. 36
1.37 NACA 64-618 with a taped leading edge [17]. 37
1.38 Lift and drag polars for the NACA 64-618 under clean and coated configurations [17]. 38

2.1 Comparison of the digitized cross-section of the full-chord model to different airfoil shapes. 42
2.2 Computational domain and domain mesh. 43
2.3 Overset mesh distribution for the clean airfoil. 44
2.4 Refinement of the C-type structured mesh distribution around the clean airfoil (a) Coarse mesh and (b) Fine mesh. 45

2.5 CFD lift and drag data at Re = $3x10^6$ compared to XFoil and experimental data (experimental surface data with surface roughness are taken at Re = $6x10^6$)[20]. 46
2.6 Tape cross-sectional design parameters of interest. 48
2.7 Example applications of a standard and a tapered LEP tape on the leading edge of the NACA 64-618. 50
2.8 Mesh refinement over the backward-facing step of the 350-6-0 tape for (a) no refinement left and right of the step the step (b) one cell across the step with a 1.2 growth rate left and right (c) two cells across the step with a 1.2 growth rate. 51
2.9 Structured C-type mesh for and airfoil with LEP tape including mesh specifics for a (a) 75 μm, (b) 200 μm, (c) 350 μm, and (d) 500 μm step height 52
2.10 Aerodynamic performance of 200 μm thick tapes compared to the 200 μm baseline tape (a) $\%\Delta c_l$ vs α (b) $\%\Delta c_d$ vs α, and (c) $\%\Delta c_l/c_d$ vs α, fully turbulent, Re = $3x10^6$. 54
2.11 Aerodynamic performance of 350 μm thick tapes compared to the 350 μm baseline tape (a) $\%\Delta c_l$ vs α (b) $\%\Delta c_d$ vs α, and (c) $\%\Delta c_l/c_d$ vs α, fully turbulent, Re = $3x10^6$. 54
2.12 Aerodynamic performance of 500 μm thick tapes compared to the 500 μm baseline tape (a) $\%\Delta c_l$ vs α (b) $\%\Delta c_d$ vs α, and (c) $\%\Delta c_l/c_d$ vs α, fully turbulent, Re = $3x10^6$. 55
2.13 Aerodynamic performance of 200 μm thick tapes compared to clean baseline (a) $\%\Delta c_l$ vs α (b) $\%\Delta c_d$ vs α, and (c) $\%\Delta c_l/c_d$ vs α, fully turbulent, Re = $3x10^6$. 56
2.14 Aerodynamic performance of 350 μm thick tapes compared to clean baseline (a) $\%\Delta c_l$ vs α (b) $\%\Delta c_d$ vs α, and (c) $\%\Delta c_l/c_d$ vs α, fully turbulent, Re = $3x10^6$. 57
2.15 Aerodynamic performance of 500 μm thick tapes compared to clean baseline (a) $\%\Delta c_l$ vs α (b) $\%\Delta c_d$ vs α, and (c) $\%\Delta c_l/c_d$ vs α, fully turbulent, Re = $3x10^6$. 57
2.16 C_p distributions for 350 μm thick tapes compared to the clean airfoil at Re = $3x10^6$ and $\alpha = 6°$. 59
2.17 Pressure coefficient distribution for baseline tapes at Re = $3x10^6$ and $\alpha = 6°$. 59
2.18 Pressure coefficient distribution for two tapered tape configurations at Re = $3x10^6$ and $\alpha = 6°$. 60
2.19 Fully-turbulent and Transition c_p for the clean NACA 64-618 airfoil at $\alpha = 6°$, Re = $3x10^6$. 62

2.20 Refined overset mesh distribution for the clean airfoil for transition modelling. . . . 63
2.21 Refined overset mesh distribution for taped airfoils suitable for transition modelling and step meshes for (a) 75 μm, (b) 350 μm, and (c) 500 μm. . . . 64
2.22 Comparison of numerical CFD data for lift and drag with transition modeling included to experimental data from XFoil and Abbott and von Doenhoff [20]. . . . 64
2.23 (a) Velocity and (b) pressure distributions over the clean airfoil at $\alpha = 6°$. . . . 66
2.24 Clean NACA 64-618 boundary layer intermittency distribution. . . . 66
2.25 Velocity flow field over (a) 350 μm and (b) 500 μm step 67
2.26 Pressure contours over (a) 350 μm and (b) 500 μm step 67
2.27 Boundary layer intermittency over (a) 350 μm and (b) 500 μm step 68
2.28 Velocity flow field over a 75 μm step for a tape of (a) 350 μm and (b) 500 μm maximum thickness 68
2.29 Pressure contours over a 75 μm step for a tape of (a) 350 μm and (b) 500 μm maximum thickness 69
2.30 Boundary layer intermittency over a 75 μm step for a tape of (a) 350 μm and (b) 500 μm maximum thickness 69
2.31 Comparison of c_p distributions between the clean, baseline, and down-selected tapered designs for 350 μm and 500 μm thick tapes at $\alpha = 6°$ and Re = 3x10^6. . . . 70
2.32 Aerodynamic performance of baseline and tapered tapes compared to the clean NACA 64-618 (a) c_l vs α (b) c_d vs α, and (c) c_l/c_d vs α with transition modeling at Re = 3x10^6. . . . 72
2.33 Aerodynamic performance of tapered tapes compared to their baselines (a) c_l vs α (b) c_d vs α, and (c) c_l/c_d vs α with transition modeling at Re = 3x10^6. . . . 73
2.34 Percent change in c_l/c_d of LEP tapes compared to a clean NACA 64-618 airfoil for fully turbulent and transition modeling at Re = 3x10^6. . . . 74

3.1 Schematic of the PSU low-speed, low-turbulence, subsonic wind tunnel. . . . 76
3.2 Wake probe schematic 77
3.3 Full-scale chord wind tunnel model 78
3.4 Schematic of the wind tunnel model top (left) and bottom (right) mounting plates. . . . 79

3.5 Complete assembly of the full-scale chord model in the PSU low-speed, low-turbulence wind tunnel. 79
3.6 Standard 3M LEP tape applied to the wind tunnel model. 81
3.7 Measured profile drag of the clean model as a function of Reynolds number. 83
3.8 Percent change in Cd relative to the clean model as a function of Reynolds number. 84
3.9 Oil visualization of transition location on the upper surface at $\alpha =$ $0°$ and Re = 3x10^6 for a) clean, b) 350-6-0, and c) 500-2-G. 85
3.10 Blasius solution for the boundary-layer velocity profile over a flat plate [9]. 88
3.11 Roughness Reynolds number as a function of roughness height for a 6-in wide LEP tape. 90
3.12 Comparison of Re_k as a function of roughness height, k, for 5-in and 10-in wide LEP tapes. 91

4.1 Wind turbine airfoil definition at each spanwise location [21]. 94
4.2 spanwise torque distribution for the PSU 1.5 MW wind turbine. . . 94
4.3 Power curves for PSU 1.5 MW and the new PSU-Tape-Clean wind turbine. 97
4.4 Power curves for a wind turbine blade with leading-edge erosion compared to a clean blade 98
4.5 Power curves for a wind turbine blade with leading-edge erosion compared to a clean blade 99
4.6 Power curves for a wind turbine blade with leading-edge erosion compared to a clean blade 100
4.7 Effect of various LEP tape configurations on wind turbine power output. 101
4.8 Weibull probability distribution of wind speeds for k = 2, λ = 8 m/s. 102
4.9 Percent change in AEP as a function of average percent change in Cd. 104

List of Tables

2.1 Convergence of lift, drag, and pitching moment at $\alpha = 0°$ for increasing number of wrap-around points over the airfoil. 45
2.2 Baseline tape configurations, with no tapering, for additional performance comparison. 47
2.3 Matrix of designs for $T_{thick} = 200\ \mu m$ 49
2.4 Matrix of designs for $T_{thick} = 350\ \mu m$ 49
2.5 Matrix of designs for $T_{thick} = 500\ \mu m$ 50
2.6 Change in aerodynamic lift coefficients for mesh refinement across the backward-facing tape step. 52
2.7 Down-selected tapered LEP tape designs for further analysis and testing. 61

4.1 Technical summary of the PSU-Tape wind turbine [21]. 95
4.2 Change in lift coefficient, drag coefficient, and c_l/c_d of the NACA 64-618 airfoil due to an eroded leading edge. 99
4.3 Effect of erosion and different tape configurations in wind turbine AEP. 103

List of Symbols

α	angle of attack
β	local collection efficiency
η	non-dimensional height above the surface in the boundary layer
ρ	density
μ	absolute viscosity
δ	boundary layer thickness
ν	Poisson's ratio
v_D	damage threshold velocity
K	fracture toughness of a material
d	droplet diameter
E	Young's modulus
F_i	impact force of a particle
m	mass
v_i	particle impact velocity
F_D	damage force
n_w	number of impacting water particles
x	stream-wise distance from the airfoil leading edge

V_o	free-stream velocity
C_l	2D lift coefficient
C_d	2D drag coefficient
C_m	2D pitching moment coefficient
C_p	2-D pressure coefficient
L/D	2-D lift to drag force ratio
Re	free-stream Reynolds number
c	airfoil chord length
Re_k	Reynolds number based on roughness conditions
Re_x	local Reynolds number based on conditions outside the boundary layer
u_k	local stream-wise velocity inside the boundary layer
u_x	local stream-wise velocity outside the boundary layer
k	height of a roughness element
s	stream-wise distance from the forward stagnation point
l	distance between consecutive pits
h	pitting erosion depth
T_{thick}	Maximum thickness at LEP tape center
W_{thick}	Width of maximum thickness region
T_{thin}	Thickness at the edge of the LEP tape
θ_{taper}	Taper angle from maximum thickness to minimum thickness
ε_t	wind tunnel blockage correction factor
D	2-D drag force
V	velocity in the wake
S	unit section of a wind tunnel model

H_o	total head in the free-stream
H	total head in the wake
p_o	free-stream total pressure
p	wake total pressure
y	distance normal to the surface
P	power
Ω	angular rotor velocity
dQ	incremental torque of a rotor element
B	number of blades
ϕ	blade flow angle
r	span-wise distance from the root of the rotor blade
P(V)	rotor power generated at a wind speed V
p(V)	Weibull distribution probability of a wind speed V occurring in one day

Subscripts:

t	target surface
w	water particle
o	free-stream conditions
k	conditions at height of roughness particle
x	local conditions outside the boundary layer
crit	conditions required for transition

Acknowledgments

Thank you to my advisers, Dr. Palacios and Dr. Schmitz, for pushing me intellectually, expanding my knowledge of the fundamentals, and providing the best guidance throughout the course of our research efforts.

I am grateful to 3M for the opportunity to conduct such impactful research - both on my academic career and, hopefully, on the future of wind energy. Many thanks to Benton Free at 3M for your work pursuing this project with us and advising us every step of the way on the specifics of the tape design process.

Dr. Maughmer, your experimental and aerodynamic expertise were instrumental in telling the whole story. You challenged me to used fundamentals and approach the problem from another direction, which allowed me to paint a more complete picture in this work.

Thank you to the Pennsylvania State University Machine Services department for your assistance to manufacture and assemble the wind tunnel model. Rick Auhl, thank you for your invaluable assistance and expertise while developing and installing the wind tunnel model.

EverPower Wind Holdings Inc., thank you for providing the wind turbine blades for experimental testing.

Dedication

Mom, none of this would have been possible without your love, encouragement, and support every step of the way.

Chapter 1

Literature Review

1.1 Introduction

Wind turbines are one of the world's leading sources of renewable energy. As of 2017, wind energy became the United States' leading renewable energy market at 6.3% of total U.S. power production [22]. As leaders in both new capacity installations and total installed capacity in 2017, almost 5% of China's total power production comes from wind energy [23]. In Europe, wind energy supplied 11.6% of the EU's total electricity demand in 2017 [23]. In the future, these numbers are only expected to grow.

Despite the already wide-spread implementation of wind turbines as an alternative energy source, climate change and its effects on the environment remains an immediate global concern. Average global land and sea temperature is estimated to have already warmed 1°C above pre-industrial levels [24]. Drastic increases in the concentrations of carbon dioxide, methane, and nitrous oxide in the atmosphere are extremely likely to be the cause of the measured warming trend [24]. Decreased crop yield, species loss and displacement, and an increase in the number and duration extreme weather events such as drought, wildfires, flooding, and cyclones have all been attributed to the rise in global temperatures [24]. Unless atmospheric concentrations of greenhouse gases are reduced in the near future, the detrimental effects to people and the environment already observed will become irreversible.

In 2015, world leaders and Heads of United Nations Member States came together to develop Sustainable Development Goals (SDGs) - an aggressive, collaborative plan to achieve prosperous and sustainable living for people and planet by 2030 [25]. Related to renewable energy and sustainable living is SDG7: Affordable and Clean Energy. The goal of SDG7 is to dramatically increase the percentage of global energy provided by renewable sources, double the global rate of improvement in energy efficiency, and increase investments in new renewable energy technology [25]. Moving forward, efforts must be made to increase the number of installations and improve the overall performance of wind turbines to meet established global renewable energy goals towards mitigating greenhouse emissions.

To meet these goals and improve on the steady growth the wind energy sector has seen in the last decade, wind farms are being commissioned in more climatically diverse locations to take advantage of cost-effective wind resources. The United States saw the commissioning of its first offshore development in 2016 [26]. Globally, offshore developments have seen rapid growth with an 87% increase in the number of installations from 2016 to 2017 [23]. In many of the northern-most countries, such as Denmark, both onshore and offshore turbines operate in colder climates. Several African and Middle Eastern nations, where the climate is more arid, have also entered the wind energy market in the last decade, and are expected to see new growth in the near future [23].

Though these sites possess economically beneficial wind resources, they also expose the wind turbines to damaging environmental factors. Cold climates come with the risk of freezing rain impact and ice accumulation. Offshore installations are exposed to corrosive salt water. Installations in places with moderate climates may see frequent rains and insect impacts. Wind installations in the Middle East and Northern Africa are frequently exposed to sand-bearing winds. Despite the benefits of these wind resources, harsh climactic conditions damage the leading-edge of the blade surface over time in these regions. Damaged blades decrease the aerodynamic performance of the rotor, which reduces energy produced over the lifetime of the machine. Under damaged conditions, wind turbines are less efficient as they fail to operate at the designed capacity. Reduction in wind turbine efficiency due to the aerodynamic penalties of damaged rotor blades hinders achieving the goal of advancing clean energy sources set forth by SDG7.

1.2 Wind Turbine Leading-Edge Erosion

The blades of a wind turbine are the most frequently repaired and replaced component at 41.4% of reported damage cases [27]. Not only is it the most frequently damaged component, but the blades are also the most expensive to repair and replace; and, the downtime required for such maintenance also leads all other sources of turbine unavailability [27]. Common sources of blade damage include fatigue, extreme loads, manufacturing defects, as well as erosion of the blade leading edge from foreign particle impingement.

In the case of leading-edge erosion, it not only contributes to increased downtime and maintenance costs but also significantly effects power production. Occasionally, the rotor under-performs relative to the manufacturer's estimates. Measured power coefficients deviate as much as 10% - 15% from the expected value provided by the manufacturer [28]. These discrepancies are due to the sensitivity of the rotor blades to any change in the surface characteristics. Rotor blades - depending on their operating environment - experience ice, dust, or insect accumulation over their lifetime. Over longer periods of time, impacts from abrasive particles like rain, sand, and hail lead to erosion and damage of the blade surface at the leading edge.

Erosion of the blade surface or accretion of foreign particulates represent geometrical modification of the blade cross-section. These modifications pose structural concerns and affect the flow over the rotor blades [27]. The magnitude of the effect of surface modifications on the aerodynamic performance of both two-dimensional (2-D) airfoils and full wind turbine blades is well-studied across the spectrum of rotor blade surface contamination issues. Studying this phenomenon provides a foundation for understanding the importance of the effect of leading-edge erosion on wind turbine lifetime aerodynamic performance.

1.2.1 Particle Impact and Damage Mechanics

Understanding erosion patterns on wind turbine blades begins with the collection efficiency of an airfoil. Local collection efficiency, β, is a ratio of the mass impinging the airfoil surface area to the mass per unit area passing through the inlet boundary. Though typically used as a measure of aircraft ice accretion, the local collection efficiency parameter is generally a measure of how effective an object's surface is at capturing a stream of oncoming particles (Fig. 1.1).

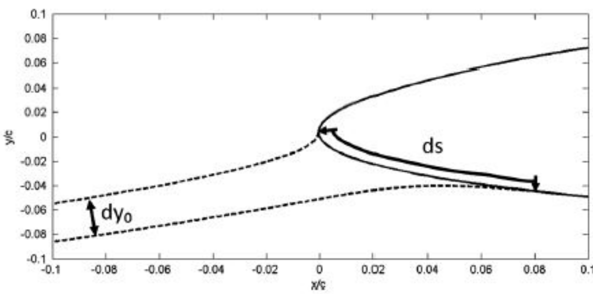

Figure 1.1. Local collection efficiency definition [1]

Collection efficiency generally peaks near the leading edge of an airfoil and falls off to zero downstream in the chord-wise direction. The exact 2-D collection efficiency profile for an object varies depending on the shape and orientation of the body, distribution of particles in the air, free stream velocity, and the mass of the impinging particles. Several studies [1, 2, 3, 29] investigate how changes in these parameters effect the peak and spread of the β distribution.

Wilcox and White [1] developed numerical models to predict how airfoil shape and particle size effect the impingement pattern on 2-D airfoils for insect impact. Both the peak and width of the β plot were found to change with particle size. Smaller particles, like fruit flies, tend to follow streamlines with little deviation because they have less inertia [1].

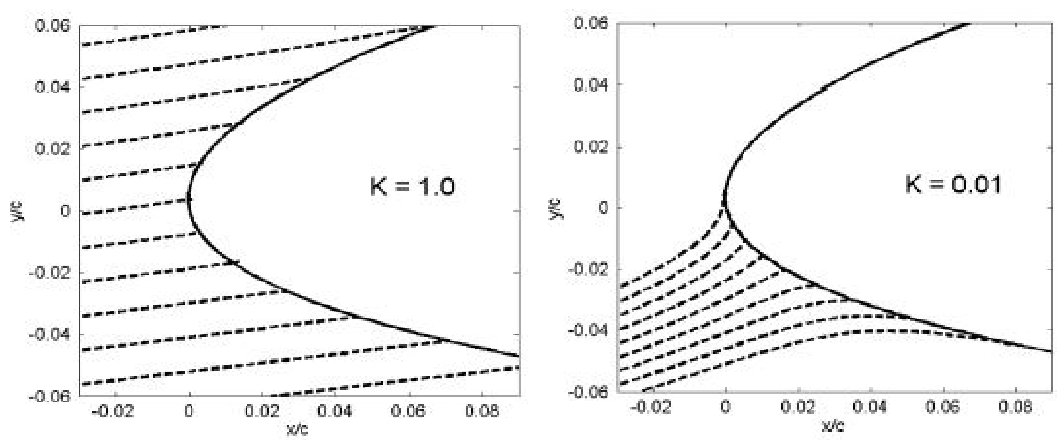

Figure 1.2. Variation in particle trajectory with size. [1]

Trajectories of larger particles, like ice and sand, see little influence from the local flow field due to their high inertia. As a result, larger particles will deviate from the flow field and impinge more of the airfoil surface (Fig. 1.2). Here, Wilcox and White [1] use the dimensionless parameter K as a measure of the inertia of the particle. High values of K indicate large particles, while low K values represent small particles.

For the same airfoil held at a constant angle of attack and with constant freestream velocity, as particle size increases, it has been shown that both peak collection efficiency and the extent of the impinged surface increase [1, 2, 29]. As mass and inertia increase for larger particles, the number of un-deflected streamlines increases (Fig. 1.3), resulting in a wider collection efficiency interval. The increased particle momentum is also responsible for a larger peak collection efficiency observed in the figure below.

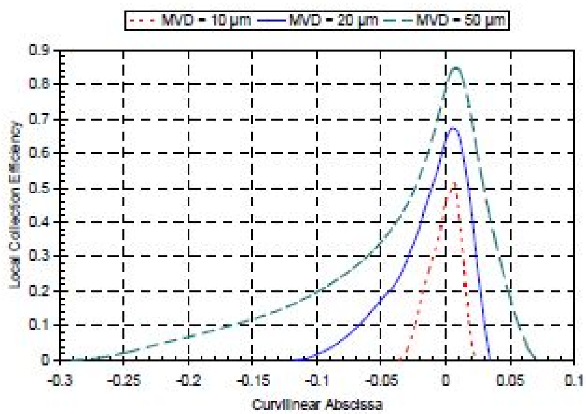

Figure 1.3. Variation in local collection efficiency with particle size. [2]

Airfoil shape also has a strong impact on the local collection efficiency profile. Both the impingement limits and the maximum collection efficiency change with airfoil thickness (Fig. 1.4). As airfoil thickness increases, the impingement limits increase and maximum collection efficiency decreases.

Local angle of attack changes along the span of a wind turbine with changes in inflow velocity and local twist angle. Since the collection efficiency profile is dependent on the surface area exposed to the flow, changes in local angle of attack will have an effect on the expected collection efficiency profile at various locations along the blade span. This, in turn, effects erosion patterns.

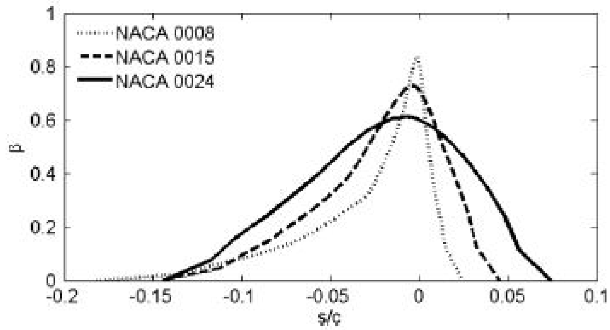

Figure 1.4. Local collection efficiency variation with airfoil profile [1]

As Wilcox and White [1] found, changes in angle of attack shift the impingement limits while peak collection efficiency remains relatively stable (Fig. 1.5). As angle of attack increases, the upper surface impingement limit moves toward the leading edge. Consequently, the lower surface limit increases as more of the pressure side is exposed to the oncoming, particle-laden flow.

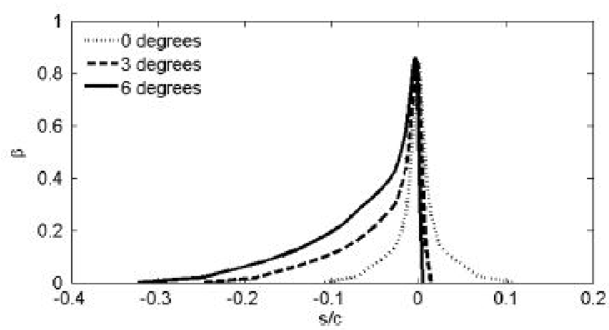

Figure 1.5. Local collection efficiency variation with local angle of attack [1]

The work of Hu et al. [3] goes further by developing an Eulerian numerical model for collection efficiency. After sufficient verification, the model is used to quantify the effect of air flow velocity and chord-length on the collection efficiency profile for the S809 airfoil. Just as increasing particle size increases both impingement limit and peak collection efficiency, increasing the air flow velocity has the same effect (Fig. 1.6). Though the effect is small for the S809 airfoil, Hu et al. conclude that the increased kinetic energy imparted to the oncoming particles with higher air flow velocities also makes the particles more difficult to deflect.

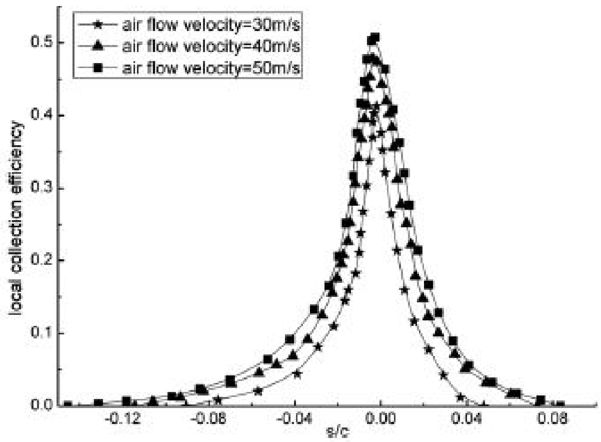

Figure 1.6. Change in local collection efficiency with air flow velocity [3].

By changing the chord length of the airfoil, collection efficiency limit and peak collection efficiency decrease as chord length increases (Fig. 1.7). Airfoils with longer chords have a smaller relative thickness [3], so the impact of chord length is similar to the result of changing airfoil thickness from Wilcox and White's work.

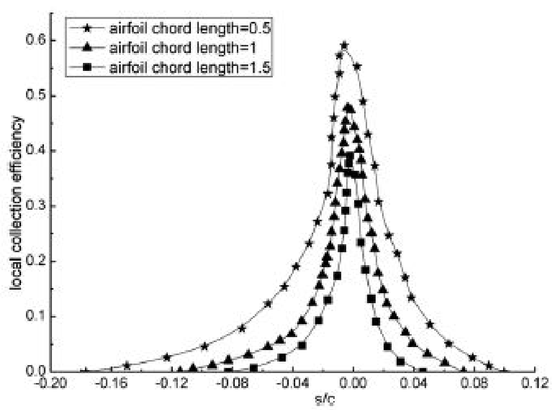

Figure 1.7. Change in local collection efficiency with airfoil chord length [3].

From the observed trends in collection efficiency above, the impact profile of particles on a wind turbine blade can be determined. Peak collection efficiency and impingement limits are expected to be highest in the tip region of a wind turbine blade, where relative inflow velocities are highest and the chord is smallest. The airfoils are also thinner in the tip region, so higher collection efficiency is expected at the leading edge and with slightly smaller impingement limits.

This estimated blade collection efficiency profile is nearly consistent with the work of Castorrini et al. [4]. Based on the blade orientation, geometry of the cross-sections, operating conditions, and using rain as the working particle, the highest impact count is observed on the suction side (upper surface) of the blade in the tip region (Fig. 1.8). From the analysis of the effect of local angle of attack on collection efficiency, we would expect the pressure side to have the higher impact count since the local angle of attack is typically between 0° and 6° in the blade tip region. However, the effect of airflow velocity seems to dominate here, causing the shift in collection efficiency peak to the suction side where velocities are highest.

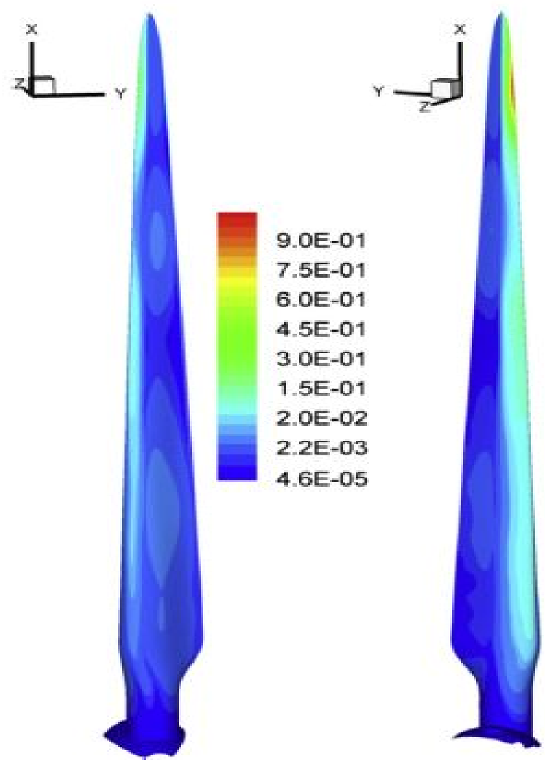

Figure 1.8. Normalized particle impact count for a wind turbine blade, pressure side (left) and suction side (right) [4].

Castorrini et al. breakdown the 3-D result in Fig. 1.8 into collection efficiency plots at discrete spanwise locations (Fig. 1.9). The largest peak collection efficiency is observed near 90% span, which also has the smallest impingement limits. Further in-board, peak efficiency drops and impingement limits increase. Interestingly, the highest impact count is not located exactly at the tip of the blade (where the largest air flow velocities are observed) because of the three-dimensional (3-D) effects that 2-D collection efficiency models do not include.

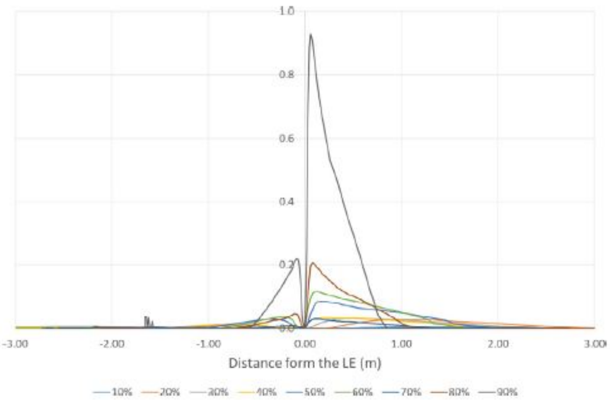

Figure 1.9. Variation in local collection efficiency along the span of a wind turbine blade [4].

Hu et al. [3] also investigated the impact of 3-D effects on local collection efficiency. Out at the blade tip, the cross-flow from the upper to the lower surface and the swirling flow of the tip vortex change the flow field such that peak collection efficiency goes to zero very rapidly near the tip (Fig. 1.10). Particle impact, and consequently erosion potential, is relatively insignificant in the tip region.

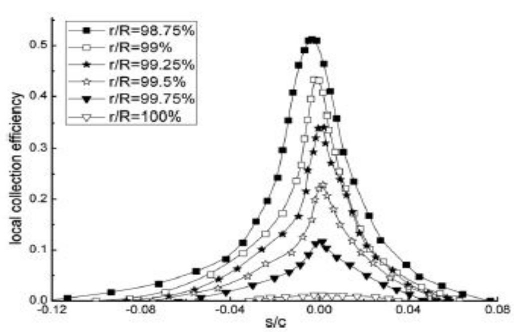

Figure 1.10. Local collection efficiency at the tip of a wind turbine blade [3].

The β parameter only gives an idea of particle impact limits and where to estimate erosion potential. The magnitude and dispersion of physical surface erosion depends on the impact mechanics of the impinging particles and the material properties of the blade surface.

Corsini et al. [5] give several simple relations to estimate damage potential of an impacting particle in their work that developed a numerical model as a design tool to explore the sensitivity of large-scale wind turbine blades to erosion. The damage threshold velocity is the minimum impact velocity a particle must have to damage a target surface, and is given by

$$v_D = c_w 1.41 \left(\frac{K_t^2 c_t}{\rho_w^2 c_w^2 d_w} \right)^{\frac{1}{3}} \tag{1.1}$$

Damage, in this model, is dependent on the properties of the material (given by the subscript, t) and the properties of the impacting particle (subscript w, for rain particles). The rain droplet properties of importance are the density, ρ_w, droplet diameter, d_w, and the wave speed of the particle, c_w. The target surface properties of interest are the fracture toughness, K_t, and the Rayleigh wave velocity, given by

$$c_t = \left(\frac{0.862 + 1.14\nu_t}{1 + \nu_t} \right) \left[\frac{E_t}{2(1 + \nu_t)\rho_t} \right] \tag{1.2}$$

which depends on Poisson's ratio, ν_t, Young's modulus, E_t, and the density of the target material, ρ_t.

The potential for surface damage is related to the force of impact through

$$F_i = \frac{m_w v_i^2}{d_w} \tag{1.3}$$

while the force required for damage, based on the damage threshold velocity, is given by

$$F_D = \frac{m_w v_D^2}{d_w} \tag{1.4}$$

Finally, the magnitude of damage caused by an impacting particle to the target surface is approximated by the ratio of the impact and damage force, scaled by number of impacting particles, via

$$Damage = n_w \frac{F_i}{F_D} \tag{1.5}$$

From the above equations, impact velocity determines the extent of the blade surface damage, and that velocity is highly dependent on the blade configuration. From Eq. 1.5, it is expected that the location of highest particle impact is most susceptible to the highest levels of damage. Based on local collection efficiency profiles, the highest particle impact count is at the leading edge, confirming that it is most susceptible to damage.

The work of Castorrini et al. [4] focuses on the numerical prediction of the expected erosion pattern using the National Renewable Energy Laboratories (NREL) 5 MW wind turbine blade as a baseline (Fig. 1.11a). The occurrence of damage is concentrated at the leading edge along the whole span of the blade. Highest levels of damage are observed in the blade tip region, corresponding to the highest impact count (Fig. 1.8a) and the highest blade inflow and droplet velocities [5].

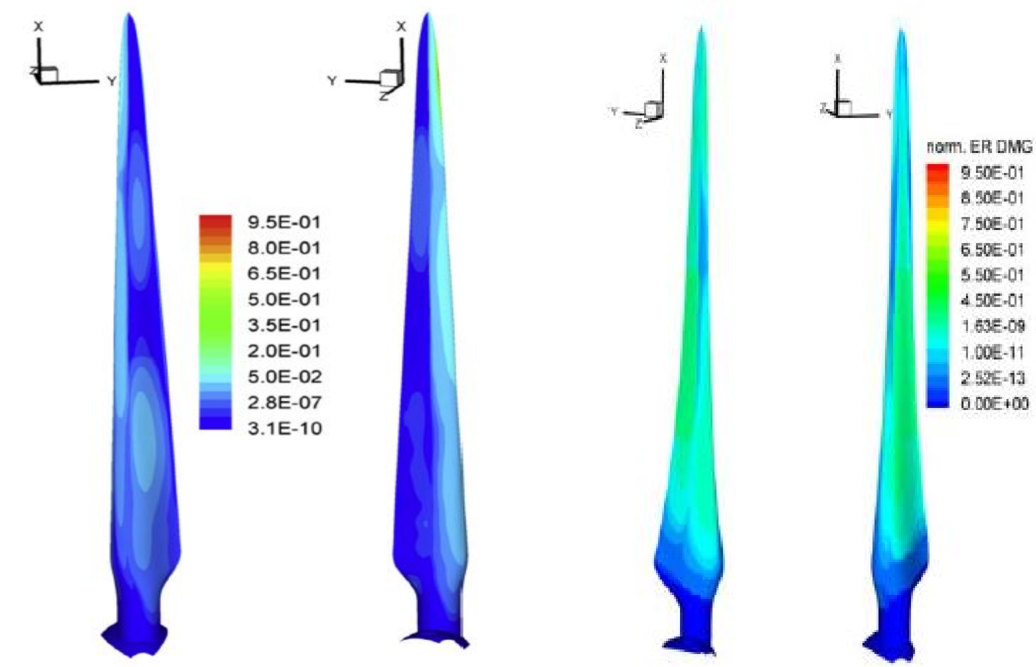

Figure 1.11. Normalized damage count for **a)** the NREL 5 MW blade, pressure surface (left) and suction surface (right) [4], and **b)** an optimized blade, suction surface (left) and pressure surface (right) [5].

It is also observed that blade geometry effects the distribution of damage, just as it effects local collection efficiency. Corsini et al. [5] use the damage model outlined above to predict the erosion rate for a geometry similar to the NREL 5 MW blade but with airfoil, chord, and twist optimization. The work is a follow up to Castorrini et al. [4], where the standard blade damage pattern is given in

Fig. 1.11a. Unlike the damage profile for the standard blade geometry, the erosion is more distributed around the surface of the optimized blade with a large region of damage around mid-span (Fig. 1.11b). Corsini et al. attribute this difference in damage patterns to the change in air flow over the blades as a result of the optimized airfoils, indicating the strong dependence of wind turbine blade erosion on the velocity distribution over the blade.

1.2.2 Observed Leading-Edge Erosion

Through these impact and damage mechanics, harsh operating environments erode the material at the leading edge of wind turbine blades. Rain, sand, hail stones, and other sizable particles impinge the leading edge of wind turbine blades at high velocities. Damage patterns predicted in Fig. 1.11 does not happen immediately. Over time, impact from particles at high enough velocities creates small damages to the leading edge surface that grow with continued impingement from natural sources (Fig. 1.12).

Figure 1.12. Examples of observed leading-edge erosion over the lifetime of a utility-scale wind turbine blade [6].

Based on observed examples of operational wind turbines, several studies [8, 7, 28] have categorized the severity of leading-edge erosion throughout the operational lifetime of a wind turbine. Erosion of the leading edge begins with the formation of small pits/pin holes within the first year of operation. Further impact from abrasive particles causes the small pits to grow until they combine and form gouges. Those gouges increase in surface area and depth until sections of the leading edge are delaminated. After 10 or more years in operation, the entire leading edge will be delaminated.

Gaudern [7] provides a visualization of the progression of erosion at the leading edge (Fig. 1.13). In this progression, Stage 1 erosion is the initial formation of pits at the leading edge. Stages 2 and 3 represent the formation and growth of gouges from the pits in Stage 1. Stage 4 erosion is the growth of the gouges into local regions of delamination, while Stage 5 erosion is complete delamination of the leading edge.

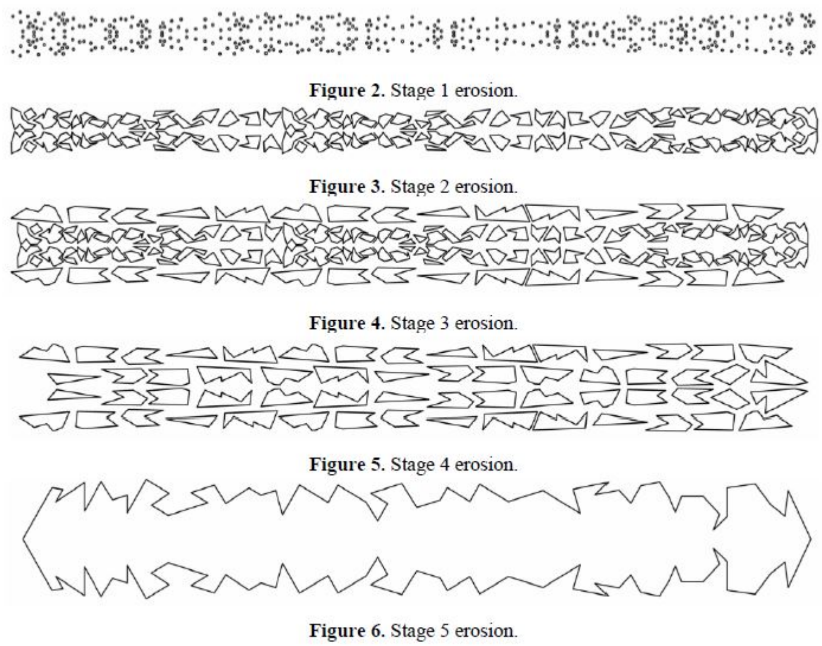

Figure 1.13. Front view of the progression of leading-edge erosion on a wind turbine blade [7].

As observed in the photos of eroded blades and predicted in the collection efficiency analysis, erosion is not confined to the very leading edge but extends along the chord-wise direction of the blade. The three stages of erosion do not exist independently as, for example, a blade with gouging will also have small pits that are either new or have not yet grown into gouges.

Through the same method of observing photos of operational wind turbine blades with erosion, Sareen, Sapre, and Selig [8] extended the model of leading-edge erosion in Fig. 1.13. They estimate that the chord-normalized extent of leading-edge erosion was $x/c = 0\ \%$ - 13% of the surface, which matches the extent of the local collection efficiency impingement limits (Fig. 1.14). Observation shows that pits and gouges exist in the full range of the eroded area, while leading-edge delamination only extends to at most x/c = 4% of the upper and lower surfaces.

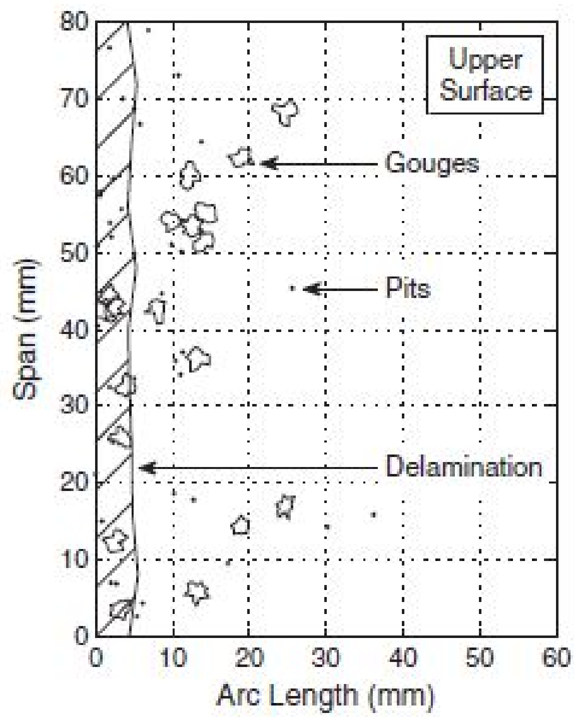

Figure 1.14. Depiction of the chord-wise extent of each stage of leading-edge erosion on the upper surface of a blade [8].

Besides chord-wise variation in the extent of each stage of erosion, pits and gouges vary in size/diameter and density, and delamination varies in depth across the spectrum of erosion. Sareen, Sapre, and Selig [8] estimate that nominal pit and gouge depth/diameter is 0.51 mm and 2.54 mm, respectively. Delamination depth was estimated at 3.81 mm. The density of the pits and gouges, meanwhile, increases with operational time in the field. Regardless of the extent, size, and density of the leading-edge erosion, even the earliest stages of erosion change the surface characteristics of a wind turbine blade. And it is these surface deformations that impact the aerodynamic performance of wind turbines over their operational lifetime.

1.3 Aerodynamics of Rough Surfaces

The fundamentals of boundary-layer theory inform our understanding of how leading-edge erosion degrades the aerodynamic performance of rotor blades. For a given flow over an aerodynamic body, the resultant force on that body depends on whether the boundary layer is laminar or turbulent [9]. The boundary layer is a thin layer of flow close to the surface of the body where viscous effects act to satisfy the no-slip boundary condition [9]. The properties of the boundary layer are highly dependent on the Reynolds number, Re, of the flow over the body and is given by

$$Re = \frac{\rho V_o c}{\mu} \tag{1.6}$$

where U is the free-stream flow velocity, ρ is the fluid density, μ is the fluid dynamic viscosity, and L is the characteristic length of the aerodynamic body. The Reynolds number is also a ratio of the inertial to the viscous effects acting in the flow. The result is that when Re is large, viscous effects are negligible, and the boundary layer near the body is thin [9]. The extent of the boundary layer normal to the surface is taken to be when the flow reaches 99% of the outer free-stream conditions [9]. The height of a laminar boundary layer, or the boundary-layer thickness, δ, is a function of distance from the leading-edge of the body, x, and is approximated by

$$\delta(x) \sim \sqrt{\frac{\mu x}{\rho V_o}}. \tag{1.7}$$

Non-dimensionalizing by the characteristic length of the body, which is the chord length for an airfoil, the boundary layer thickness can be related to the free-stream Reynolds number [9].

$$\frac{\delta(x)}{c} \sim \frac{1}{\sqrt{Re}}\sqrt{\frac{x}{c}} \tag{1.8}$$

This confirms that as Re increases, the boundary-layer thickness decreases - a trend that will be important in understanding how the effect of surface roughness on aerodynamics of a body changes with flow conditions. It is also the case that, regardless of Reynolds number, the boundary-layer thickness increases with distance from the leading edge.

Boundary layers can be either laminar, turbulent, or both, and Reynolds number also plays a role in dictating the flow regime. A laminar boundary layer is characterized by distinct layers of flow with little interaction between the layers in the direction normal to the surface and are shear dominated [9]. Turbulent boundary layers are marked by a significant increase in the boundary-layer thickness due to the increased transverse mixing and irregular motions that are characteristic to turbulent flow [9].

Along the surface of a body, the boundary layer begins as laminar at the leading-edge and naturally transitions to turbulent when the Reynolds number along the body reaches a critical value, Re_{crit}. Over an airfoil, the natural transition occurs earlier than for a flat plate due to the added adverse pressure gradient in the stream-wise direction due to the surface curvature [9]. Hermann Schlichting's famous Stability Theory [9] discusses what flow properties influence transition and how this transition from a laminar to turbulent boundary layer occurs.

Schlichting developed his theory with the idea that the dependence of the boundary layer characteristics on the Reynolds number is a stability problem. The viscosity of the flow, μ, acts as a perturbation damper. At low-enough Reynolds numbers, μ is dominant enough to suppress any small perturbations in the boundary-layer flow so it remains laminar. When the Reynolds number goes beyond a critical value, the effect of viscosity is no longer sufficient to damp those perturbations, so they grow un-inhibited until the boundary layer is fully turbulent.

The transition from a laminar to turbulent boundary layer depends on the Reynolds number, pressure distribution of the outer flow, the surface characteristics, and the turbulence levels in the free-stream flow [9]. From experimental observation of free flow over a plate at zero-incidence, Schlichting developed a general pattern of the laminar-to-turbulent transition (Fig. 1.15). The transition process is as follows: 1) stable laminar flow, 2) formation of unstable Tollmien-Schlichting waves, 3) 3-D wave and vortex formation (Λ-structures), 4) vortex decay, 5) formation of turbulent spots, and 6) fully turbulent flow.

Besides Reynolds number, the adverse pressure gradient over the body controls the transition location. For an airfoil, the region of pressure decrease over the surface (where flow accelerates) generally remains laminar, but any increase in pressure (beyond the location of maximum thickness) induces transition [9]. The type of boundary layer over a body determines the forces acting on it. The impact of the laminar-turbulent transition is such that it is accompanied by a notable increase in friction drag. An airfoil with a long run of laminar flow, with the transition region as far back as possible in the stream-wise direction, will exhibit significantly reduced friction drag.

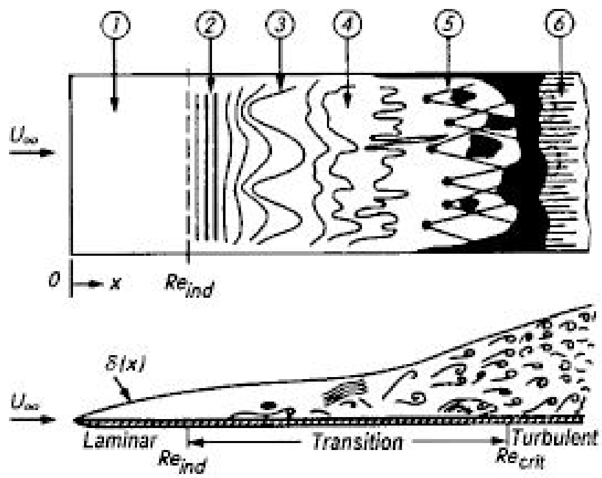

Figure 1.15. Stages of a boundary layer transition from laminar to turbulent [9].

Of interest going forward is the effect of wall roughness on the laminar-turbulent transition process. In the presence of wall roughness, transition occurs at lower Reynolds numbers, indicating that rough walls favor the transition process [9]. The additional surface roughness generates new large-amplitude instabilities to the boundary-layer flow, which reduces the critical Reynolds number, according to nonlinear perturbation theory [9]. Schlichting notes, however, that not all roughness elements induce premature transition.

The critical roughness height is the height of a surface roughness element above which premature transition of the boundary layer is induced by the roughness [30]. Past research efforts [10, 11, 30] have focused on computing both the critical transition Reynolds number and corresponding critical height of a roughness element required to induce early transition.

Knox and Braslow [30] developed a simplified method to determine the critical roughness height of a 3-D roughness element that will induce early transition for both sub- and supersonic flows. The model is a single equation that relates the roughness height to the local Reynolds number based on the roughness height and local flow characteristics. The final relationship between roughness element Reynolds number, Re_k, and the non-dimensional critical roughness height, η_k, is given by

$$\frac{Re_k}{\sqrt{Re_x}} = 2\eta_k \left(\frac{u_k}{u_x}\right)\left(\frac{\mu_o \rho_k}{\rho_o \mu_k}\right) \tag{1.9}$$

where Re_x is the local Reynolds number at a stream-wise location x. The variables u_k, μ_k, and ρ_k are the velocity, viscosity, and density inside the boundary layer at the height of the roughness element. Similarly, u_x, μ_o, and ρ_o are the local velocity, viscosity, and density outside the boundary layer.

Using Knox and Braslow's method, for a given critical transition Reynolds number, $Re_{k,crit}$ and stream-wise location of the roughness element, x, the critical roughness height, $\eta_{k,crit}$, can be determined. This method will be applied later on in this work to estimate whether or not certain leading-edge protection (LEP) tape designs cause early transition of the boundary layer.

The next step is determining the critical Reynolds number at which early-onset transition occurs. Horton and Von Doenhoff [10] determined the critical transition Reynolds number as a function of type and location of the roughness element. From the experimental data, there is a critical Reynolds number at each location along the chord of the airfoil below which the roughness elements do not induce early transition (Fig. 1.16).

The upper curve is of importance here, as the bottom one is simply the normalized version based on nominal heights of the different roughness elements tested. Along most of the body, the critical Reynolds number required for transition at the roughness element height is fairly constant at Re_{crit} = 600. However, forward of s/c = 0.025, where s is the downstream distance from the forward stagnation point, the boundary layer is thin. A thin boundary layer is more susceptible to transition from even the smallest particles, so the critical transition Reynolds number increases significantly.

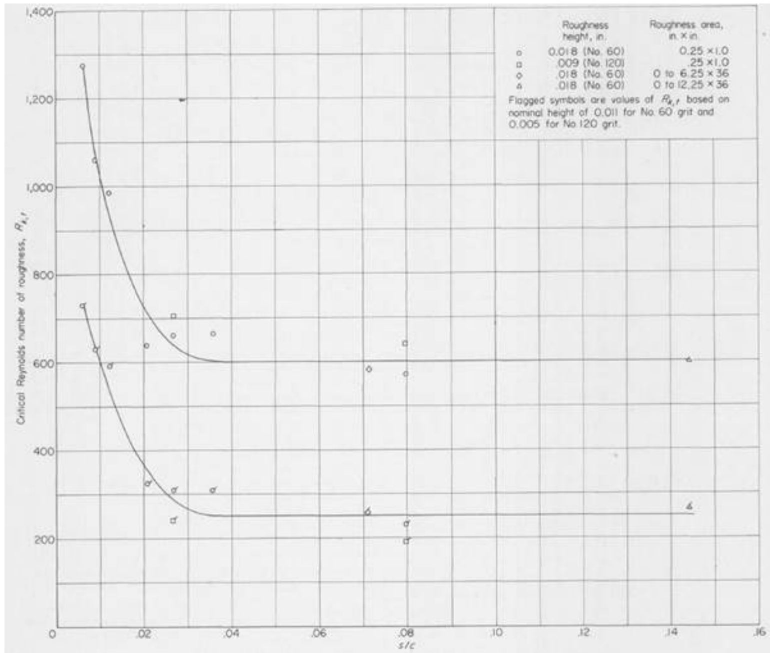

Figure 1.16. Critical transition Reynolds number as a function of roughness location [10].

With this fundamental understanding of boundary-layer theory and how roughness effects the transition of the boundary layer from laminar to turbulent, we can look at how that is reflected in the forces on and pressure distribution around an airfoil. As a follow up to the model for determining critical roughness height, Braslow, Hicks, and Harris [11] investigated the impact of roughness height on minimum airfoil drag, $C_{d,min}$ (Fig. 1.17).

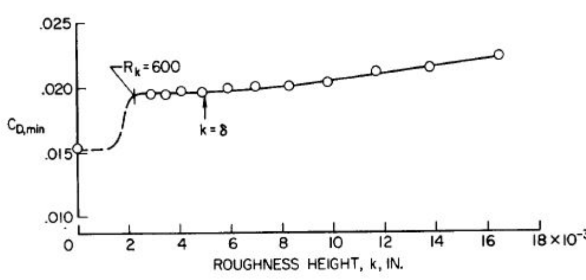

Figure 1.17. Variation in minimum drag coefficient versus roughness height for subsonic flow [11].

At the location where the roughness is placed and for a sufficiently high free-stream Reynolds number, there is a sharp increase in $C_{d,min}$ when the critical roughness height is sufficient to achieve $Re_{k,crit} = 600$. Beyond that roughness height, however, the effect plateaus and there is very little variation in the minimum drag value. Thus, any surface roughness above the critical height required to cause transition has a significant effect on the drag force acting on the body, as Schlichting predicted.

Pressure around the surface of the body is also affected by forced transition due to surface roughness, as Soltani, Askari, and Sadri find [12]. Applying 0.5 mm height roughness particles to the entire upper surface of an airfoil affected the pressure distribution of both the upper and lower surface (Fig. 1.18). For the figure below, the data are taken at AoA = 12°. It is clear that roughness significantly reduces the suction peak and the area of separated flow increased, moving toward the leading edge [12]. It is also observed that loss in suction peak increases with Reynolds number. In contrast, when the Reynolds number is held constant and angle of attack is changed, the loss in suction peak also increases with increasing angle of attack [12].

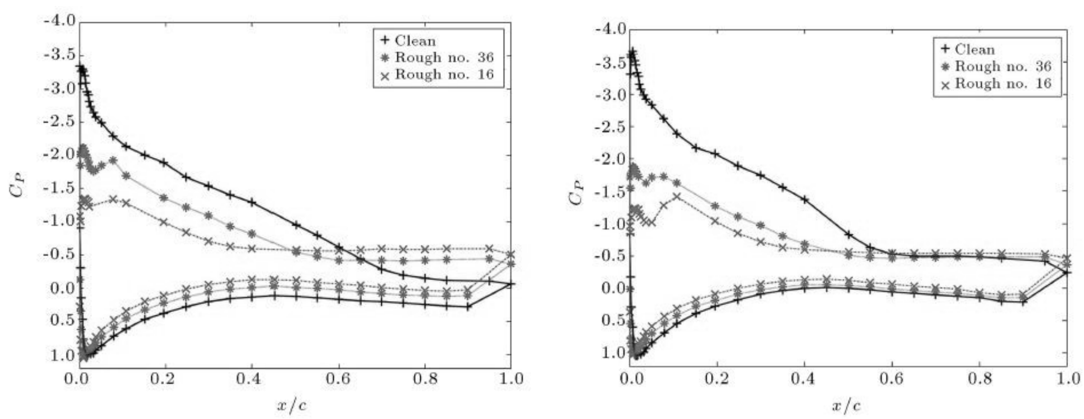

Figure 1.18. Pressure coefficient distribution around an airfoil under clean and two roughness conditions at Re = 0.43x10^6 (left) and 1.3x10^6 (right) [12].

The change in the surface pressure coefficient distribution with the presence of surface roughness beyond the critical roughness height also indicates changes in the lift coefficient. Applying a realistic contamination model to the surface of an airfoil, Soltani, Birjandi, and Moorani [13] used experimental wind tunnel data to generate aerodynamic polars of lift coefficient versus angle of attack at different Reynolds numbers (Fig. 1.19). The loss in lift coefficient for the realistic contamination model is as much as 35% of the clean lift coefficient, but it does not change significantly with Reynolds number for this airfoil [13]. Another interesting feature is the smooth stall profile caused by the change in the pressure distribution in both the wake and over the surface of the airfoil at high angles of attack [13].

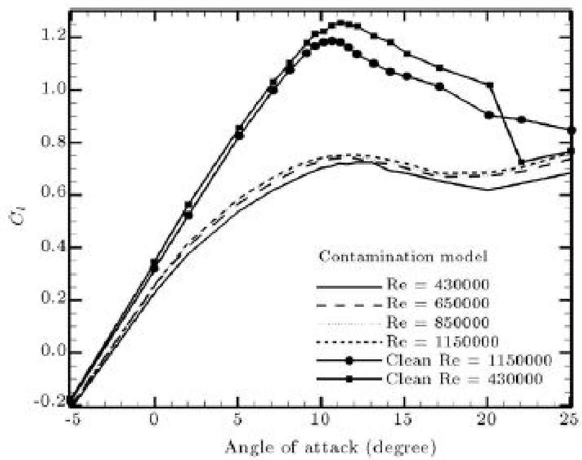

Figure 1.19. Variation in lift coefficient with angle of attack and Reynolds number [13].

Extrapolating these results to full wind turbine blades, the significant loss in lift and increase in drag due to the presence of roughened surfaces leads to a notable loss in power. Using Blade Element Momentum theory, Darbandi et al. [14] estimated the loss in power a wind turbine experiences under rough conditions (Fig. 1.20). For this pitch-controlled wind turbine, rough conditions see a shift in rated power from 12 m/s to 17.7 m/s [14]. This shift results in a loss in power generated compared to the clean case, as well as annual energy production (AEP). Though the results will differ for different roughness conditions, wind turbine sizes, and operating conditions, roughness resulted in a loss of 430 MWh of energy production, or a 25% reduction in AEP for this particular scenario.

Also relevant to wind turbine performance is how the impact of surface roughness changes along the span of the blade and how 3-D effects change the results we expect from 2-D boundary-layer theory. Van Rooij and Timmer [15] investigated the effect of surface roughness on several mid-span airfoils common to wind turbines with thicknesses ranging from 25% - 30% and low roughness sensitivity, which makes these airfoils susceptible to significant performance degradation due to surface roughness.

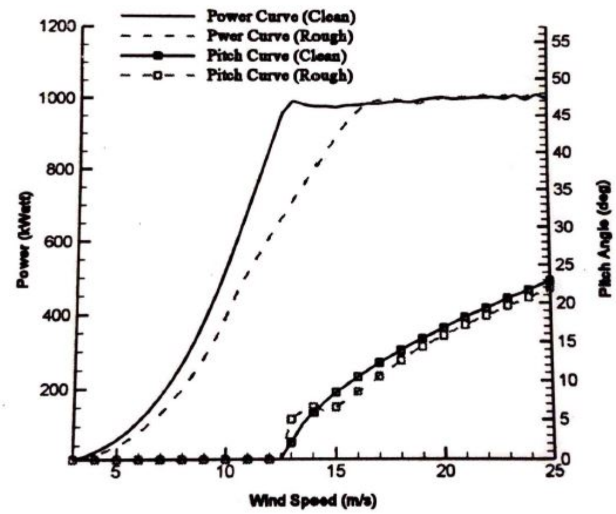

Figure 1.20. Power curves for clean and rough conditions of a 1 MW wind turbine [14].

From their experiments, airfoils at mid-span experience significantly earlier transition and increased separated flow over the airfoil surface, which de-cambers the airfoil and results in a notable loss in lift [14]. However, 3-D effects due to rotation of the blades mitigate this effect for these inboard airfoils (Fig. 1.21). For this airfoil, the effect of roughness is almost completely eliminated when rotational effects are included.

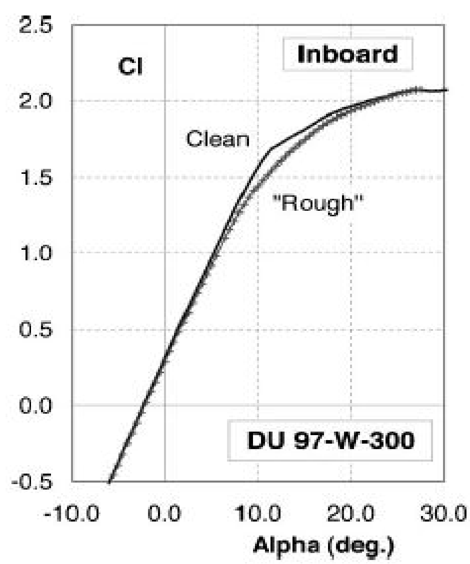

Figure 1.21. Lift coefficient for a clean and rough airfoil with 3-D effects included [15].

1.4 Aerodynamic Impact of Eroded Wind Turbine Blades

Surface roughness is a geometric feature that protrudes from the surface of a wind turbine blade. Thus, the analysis in the previous section is generally valid for the accretion of ice, dust, or insects on the blade surface. Leading-edge erosion of a wind turbine blade, however, removes material from the blade surface, creating indentations rather than protrusions. As a result, the mechanism of transition and the magnitude of the effect on the aerodynamic performance changes.

The leading-edge erosion phenomenon occurs in various stages. Wang et al. [16] studied pitting - the earliest stage of erosion - by varying pit properties to investigate which factors have the greatest influence on leading-edge pitting erosion. Pitting, in this work, is modeled with semi-circular cavities extending to some +/- x/c around the leading edge (Fig. 1.22). The depth, h, and spacing between pits, l, are varied to investigate the effect of pits on lift and drag for the S809 airfoil.

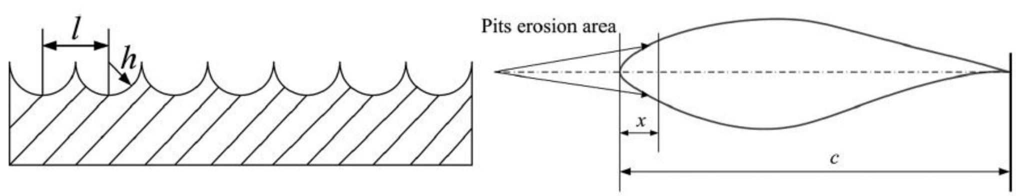

Figure 1.22. Sample pitting erosion pattern [16].

As pit size, h, increases, c_l/c_d drops significantly (Fig. 1.23). Maximum lift decrease, across all pit sizes, is 6.2% while maximum drag increase is more significant at 43.1% [16]. The effect of pit size on lift reduction and drag increase approaches a limit around h = 0.5mm [16], suggesting this is a critical value of erosion depth at this particular Re.

Looking at velocity contours over the airfoil body for various pit sizes, such as the ones in Fig. 1.24, it is easy to see why h = 0.5mm is a critical value. At small pit depths (Fig. 1.24a), the flow separation at the trailing edge, as a result of the pits draining momentum from the boundary layer, increases rapidly with increasing pit size [16]. At h = 0.5mm, the separated flow region already spans about one-third of the upper surface.

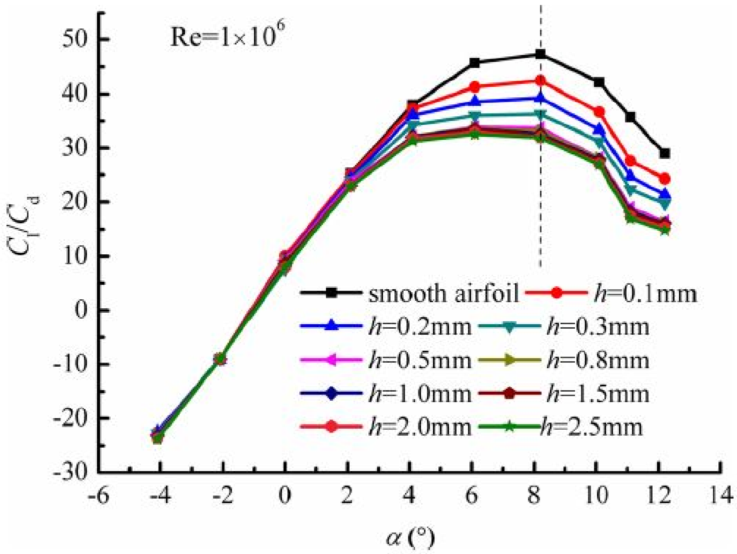

Figure 1.23. Effect of pits of various sizes, h, on c_l/c_d [16].

For pit sizes larger than h = 0.5 (Fig. 1.24b), the region of separated flow grows more slowly until around half of the upper surface is separated [16]. As boundary-layer theory dictates, it is also this separated flow as a result of a turbulent boundary layer that causes the decrease in lift and significant increase in pressure drag.

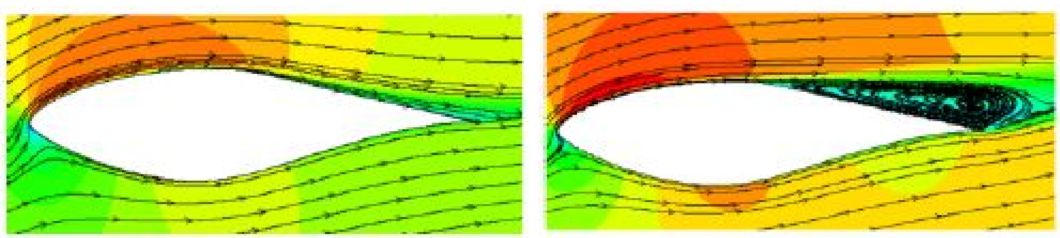

Figure 1.24. Effect of pit size, h, on the velocity field around an airfoil: (a) h = 0.1mm and (b) h = 1.5mm [16].

For a fixed pit depth of h = 0.5mm, the S809 airfoil is particularly sensitive to the effect of pit density [16]. As pit spacing decreases from l = 8d to 1d, drag increases ranging from 3% to 18%, and lift decreases anywhere from 0.6% to 5.5% (Fig. 1.25). This trend also reflects how erosion will effect a wind turbine blade over time as the pitting develops on the surface. Damage does not happen immediately, but starts as small pin holes - equivalent to the pits of spacing l =

8d - and eventually grows into larger pits with increased density - similar to the spacing of l = 2d. Though the effect of leading-edge erosion on lift and drag may start small, the performance degradation grows over time as the size, shape, and density of the erosion increases.

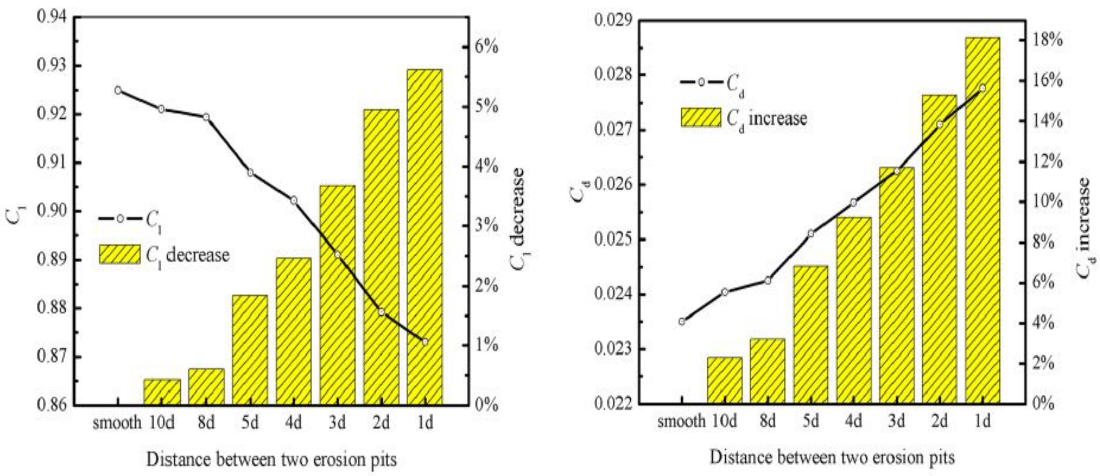

Figure 1.25. Effect of pit density, l, on (a) c_l and (b) c_d [16].

Further coalescence of the pits into gouges eventually results in complete delamination of the leading edge, effectively changing the shape of the airfoil over the delaminated region. Schramm et al. [17] used numerical methods to investigate the effect of delamination on a NACA 64-618 airfoil - another common wind turbine tip airfoil, which is also the airfoil of primary interest to the body of this work. Though pitting, gouging, and delamination do not exist independently for eroded wind turbine blades, Schramm et al. only include delamination for simplicity of modeling (Fig. 1.26).

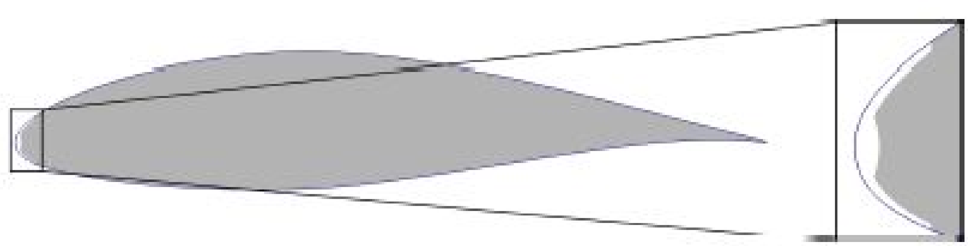

Figure 1.26. Example delamination of the leading edge of a NACA 64-618 airfoil [17].

Airfoils with significantly eroded leading edges incur larger lift decreases and drag increases compared to rough blades (Fig. 1.27). At small angles of attack, for this airfoil, the effect on both lift and drag is small. As angle of attack increases, the magnitude of the aerodynamic degradation increases for both lift and drag compared to rough airfoils. These results indicate, as suspected, that erosion cannot simply be modeled as surface roughness. Whereas surface roughness is a small protrusion from the airfoil surface into the boundary layer, the most severe cases of erosion such as this one alter the airfoil shape, leading to significantly more performance loss.

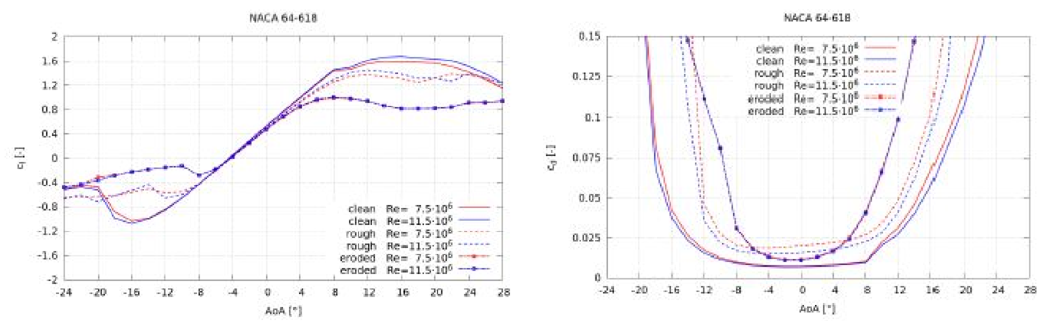

Figure 1.27. Lift and drag polars for the NACA 64-618 under clean, rough, and eroded conditions [17].

Due to the decreased lift and increased drag, a 5 MW wind turbine equipped with the delaminated airfoil in Fig. 1.26 sees power losses at all wind speeds, with the most significant occurring in Region III (Fig. 1.28). At the rated wind speed of $V_o = 11.4$ m/s, power losses are nearly 9% due to leading-edge erosion [17]. The reason for the insignificant difference between the rough and eroded cases is due to the operating angle of the NACA 64-618 airfoil in the tip section for this 5 MW wind turbine, which is around 4° or 5° [17]. At this angle of attack, the difference between the eroded, rough, and clean blades is small (Fig. 1.27), resulting in very little deviation in the power curves between all three cases. Higher power losses are possible, however, for different operating conditions and airfoils that are more sensitive to roughness or erosion at lower angles of attack [17].

The table below, from Schramm et al., summarizes the total impact of roughness and erosion on wind turbine AEP and annual revenue (Fig. 1.29). Despite having significantly different impacts on 2-D lift and drag over the full operating range of the airfoil, both rough and eroded wind turbine blades result in an 8%

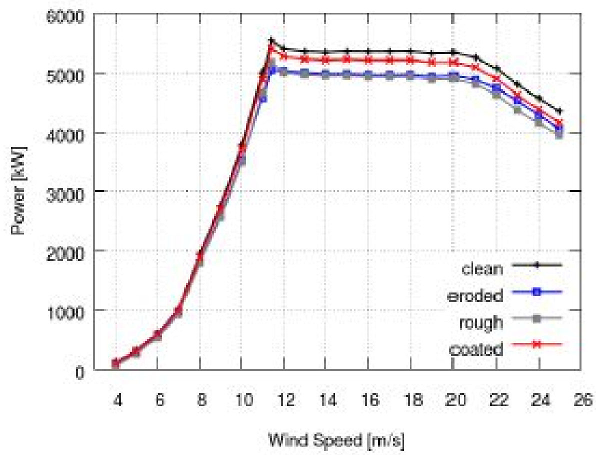

Figure 1.28. Wind turbine power curves for various blade conditions [17].

reduction in AEP. Using two different estimates for the price of electricity, the revenue lost as a result of the reduced energy produced is also estimated. Though these numbers depend on site conditions (in the case of AEP) and market fluctuations, these costs can be used for a trade-off cost analysis between blade repair, replacement, and preemptive protection solutions, as discussed later.

			Yearly Loss of Revenue	
Blade Type	**AEP (MWh/Year)**	**Difference in AEP (%)**	**with 3 ct/kWh (EUR/Year)**	**with 5 ct/kWh (EUR/Year)**
clean	16,800	0	0	0
eroded	15,600	−7.10	−37,500	−62,500
rough	15,400	−8.30	−42,000	−70,000

Figure 1.29. Degradation of AEP and revenue lost for rough or damaged wind turbine blades [17].

Gaudern [7] experimentally studied the effect of more irregular and realistic leading-edge erosion patterns in a comparative study between models of leading-edge erosion and airfoils with tripped flow. The goal of the work was to develop methods for accurately predicting the aerodynamic impact of different erosion stages on wind turbine performance for accurate cost-benefit analyses of blade repair and protection. The front-view of the different stages of erosion was already presented in Fig. 1.13. These patterns were applied via thin film to 18% thick Risø and Vestas airfoils to compare how airfoil shape effects the results.

For the various stages of leading-edge erosion, represented by the plots below

(Fig. 1.30), the level of lift reduction and drag increase generally increases with successive stages of erosion. The only exception is the transition from Stage 4 to Stage 5 erosion [7]. Though the leading edge of the airfoil is completely delaminated in Stage 5, it is also smooth, unlike the Stage 4 leading-edge erosion(Fig. 1.13). The smooth leading edge in Stage 5 has a smaller impact on the boundary layer compared to the highly irregular edge seen in Stage 4 erosion [7]. Despite this, the impact on lift and drag for the most severe stage are still significantly larger compared to early erosion. Average lift decrease between all airfoils tested is 4% and 6% for Stage 1 (Fig. 1.30a) and Stage 5 (Fig. 1.30b), respectively. Drag increases similarly ranging from 49% to 89% for Stage 1 and Stage 4 erosion. Stage 5 drag increase is comparable to that observed with Stage 4 erosion at 86%.

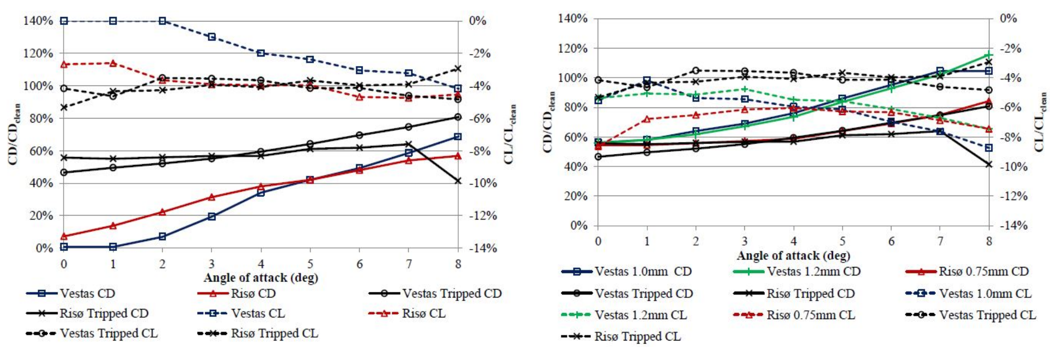

Figure 1.30. Effect of erosion on normalized lift and drag versus angle of attack for (a) Stage 1 erosion and (b) Stage 5 erosion [7].

Also of interest is the comparison between tripped and eroded cases, and the ability of tripped airfoils to predict the actual effects of leading-edge erosion. Tripped leading edges show lift losses of the same magnitude as the losses observed for early stages of erosion, but drag tends to be over-predicted at these stages of erosion [7]. For higher levels of erosion and higher angles of attack, the tripped leading edge tends to under-predict the impact of erosion [7]. Trips can be used as a guideline for estimating lift loss and drag increase due to leading-edge erosion, but realistic models are required if more accurate aerodynamic data are required [7].

The most comprehensive study of leading-edge erosion was done by Sareen, Sapre, and Selig [8]. In their leading-edge erosion model (Fig. 1.14), pits, gouges, and delamination are included in different combinations and to varying degrees to best simulate the stages of erosion a wind turbine blade experiences over its lifetime. Type A erosion consists of only pits and includes three sub-stages of increasing pit density over the leading edge. Type B erosion adds gouges, with three sub-stages of both increasing pit and gouge density. Type C, the most severe stage of erosion, includes three stages of leading-edge delamination, as well as various densities of pits and gouges. Chord-wise extent of the pits and gouges is fixed at x/c = 10% and 13% on the upper and lower surfaces, respectively. The pits and gouges are distributed over the surface with a Gaussian approximation, similar to the distribution of the local collection efficiency. Various stages of delamination extend from (in increasing severity) x/c = 1%, 2% and 3% on the upper surface and x/c = 1.3%, 2.6%, and 3.9% on the lower surface.

Type A has the smallest impact on airfoil performance, though the magnitude of lift and drag degradation increases rapidly with increasing pit density (Fig. 1.31a). Though the overall effect on lift is small, at higher angles of attack the lift degradation due to Type A erosion is notably significant [8]. Type B (Fig. 1.31b) and Type C (Fig. 1.31c) have similar trends. Performance degradation worsens as the number of pits, gouges, and leading-edge delamination extent increase. Lift losses are anywhere from -0.07 (least severe Type A erosion) to -0.17 (most severe Type C erosion) [8]. Drag increases are more significant across the erosion spectrum, ranging from 6% to 500% [8].

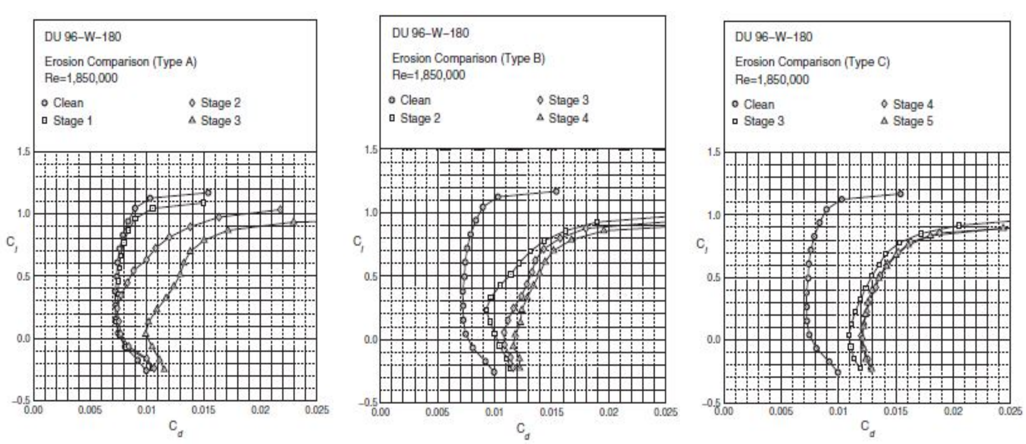

Figure 1.31. Measured effect of (a) Type A, (b) Type B, and (c) Type C leading-edge erosion on lift and drag of the DU 96-W-180 airfoil [8].

With a 2.5 MW variable-speed wind turbine as the baseline, the wind turbine design code PROPID was used to estimate the power production and AEP of the wind turbine for a variety of site conditions and blade erosion states. The turbine operates with active control systems, which means the turbine will reach rated power at different wind speeds for each erosion case [8]. The power lost by reaching rated power at higher wind speeds is what results in AEP degradation under eroded conditions. For light, Type A erosion, AEP losses were around 5%, while severe erosion can lead to AEP losses of up to 25% [8].

Previous studies on the effect of various degrees of leading-edge erosion on wind turbine AEP indicate that losses could be anywhere from 8% [17] to 25% [8]. Even for the earliest stages of erosion, an 8% power loss means tens-of-thousands of dollars per turbine in annual revenue lost [17]. In the case of severe erosion that causes structural concerns, additional costs are incurred to either repair or replace the damaged blades so that the wind turbine can continue functioning for the remainder of its operational lifetime. The downtime required to perform the maintenance on a damaged turbine also means additional losses in energy produced and revenue. Leading-edge protection solutions are therefore key to minimizing these losses, while simultaneously prolonging the lifetime of the wind turbine blades.

1.5 Leading-Edge Tapes for Erosion Protection

To combat the degenerative effects of leading-edge erosion, reinforcement or protection of the blade leading edge is necessary. Not only can proper leading-edge treatments prolong the lifetime of the blades, wind turbines also see improvements in annual energy production (AEP) compared to eroded blades. With this in mind, industry leaders such as 3M are working to develop leading-edge protection (LEP) devices for this purpose that balance cost of the protection mechanism, erosion protection efficiency, and aerodynamic performance.

1.5.1 Leading-Edge Protection Materials

Wind turbine leading-edge erosion is caused by surface fatigue from repeated impacts due to rain and other particles. To counter this effect and prolong blade lifetime, protective materials can be applied to the leading edge of the blades. These materials should reduce the pressure caused by particle impact with the blade surface and enlarge the safe area by having adjustable compressive stresses and hardness [31]. This fatigue failure resistance, and thus erosion protection, can be achieved through careful selection of a leading-edge material that reduces impact pressure from the particles and shifts the number of stress cycles required for fatigue failure to higher stress levels [31].

Appropriate materials for rain erosion protection can be determined using the methodology behind the impact and damage model discussed in section 1.2.1. Rather than using the properties of wind turbine blade materials as the target surface properties, other materials can be chosen that display higher resistance to the damage of an impacting rain droplet by increasing the value of the damage threshold velocity in Eq. 1.1 [32]. At present, the industry promotes polyurethane based materials for erosion protection [32]. As an elastomeric material, polyurethane based options have great erosion resistance to particles impacting at high angles, as rain tends to do at the leading edge of an airfoil [32].

To characterize the erosion resistance potential of several polyurethane based materials, Valaker and Wilson [32] investigated four (4) erosion protection coatings in a droplet-erosion test rig. The parameter for performance evaluation was material loss of each coating (in mg) after 20 min of testing at an impact velocity of 100 m/s. Wind turbines frequently sustain 100 m/s impact velocities for hours over the lifetime of the rotor. To sufficiently model abrasive rain droplet impact on wind turbine blades, however, longer testing times are required.

One of the coatings tested was an industrial protection tape. Though it was the only one to experience adhesive failure, Valaker and Wilson were optimistic about the erosion resistance potential of industrial tapes. Production methods used to develop polyurethane-based erosion protection tapes make them desirable because the mechanical properties of the tapes can be well-controlled [32]. They hypothesized that, if the adhesion had not failed, the erosion resistance of the tape would have exceeded the already excellent performance of the other coatings tested.

A review of potential wind turbine erosion protection coating technologies by Slot et al. [31] also concludes that polyurethane and other elastomers are among the best materials for erosion protection. To improve blade lifetime with respect to erosion, the maximum stress at the leading edge must be less than the fatigue endurance strength [31]. From the review by Slot et al., polyurethane coated surfaces displayed stresses and strains well below values that induce material failure. However, polyurethane-based coatings are more susceptible to high cycle fatigue failure [31]. For a polymer or elastomeric coating of a certain thickness, both maximum stress and pressure induced by droplet impact are sufficiently damped due to the very low stiffness of these materials, making them ideal for LEP devices [31].

For LEP application, there are two methods for integration of the protection material with wind turbine blades: in-mold and post-mold. In-mold application, where a gel-coat is applied during the liquid composite molding process, is advantageous due to the ease of integration of the coating with the manufacturing process and the reduced cost of application [6]. Post-mold products typically include tapes and are generally polyurethane-based, making them more ideal for erosion protection [6].

The main difference, and what makes post-mold applications more suitable for erosion protection, is in the material used for each application. In-mold applications typically use materials similar to the material matrix of the wind turbine blade, making them rigid, brittle, and they have a high modulus since they are typically epoxy- or polyester-based [6]. Post-mold tapes, as mentioned earlier, tend to be polyurethane-based. These coatings are developed specifically for leading-edge erosion protection and have a low macroscopic elastic modulus, high ultimate strain, and high stress [6]. As the analysis from Slot et al. noted, these properties make post-mold LEP tapes excellent erosion protection devices due to their ability to reduce stresses at the impact surface and dampen stress waves generated by droplet impact [6].

Of interest to this work is the 3M$^{\text{TM}}$ Wind Protection Tape 2.0 W8750. According to the technical bulletin for the product [33], the tape is easy to apply and shows no embrittlement with time, so the erosion resistance does not change over time. The tape has a thickness of 350 μm [34]. Unlike coatings, tape thickness is well-controlled [33], which translates to consistent results for erosion protection across multiple tape applications. Additionally, their tape boasts a permanently tacky, self-healing adhesive layer. If small areas of separation occur between the tape and the blade surface, the adhesive is able to re-connect itself, prolonging the lifetime and performance of the tape [33]. While the application of tape such as this to the leading edge of a wind turbine blade may prolong blade lifetime by delaying erosion, it has been shown that these tapes also impact the aerodynamic performance of wind turbine blades.

1.5.2 Aerodynamics of Leading-Edge Protection Tapes

As a follow-up to their work investigating the effect of erosion on wind turbine blade performance, Sareen, Sapre, and Selig [18] partnered with 3M to investigate the impact of applying LEP tape to wind turbine airfoils. The parameter of interest to their performance investigation was the chord-wise extent of the tape on the upper and lower surface, and how that effected lift and drag of the airfoil, as well as AEP for a 2.5 MW wind turbine.

The airfoil used for testing was the DU 96-W-180, an 18% thick airfoil commonly used for wind turbine tip sections. The tape applied was the 350 μm thick polyurethane 3M^{TM} Wind Blade Protection Tape W8607. The tapes were applied and tested in a wind tunnel in six different configurations with varying chord-wise extents on the upper and lower surfaces. For three cases, the chord-wise extent of the tape on the upper surface was fixed x/c at = 10% while the extent of the tape on the lower surface was either at x/c = 10%, 20%, or 30%. The remaining three cases fixed the lower surface extent at x/c = 20% and varied the upper surface at x/c = 10%, 20%, or 30% (Fig. 1.32).

Figure 1.32. Sample tape coverage on the DU 96-W-180 for x/c = 30% upper surface and x/c = 20% [18].

Airfoil c_l is plotted versus c_d at Re = 1,850,000 for tapes with a lower surface coverage of x/c = 10% and varying upper surface coverage (Fig. 1.33). The clean baseline data is included for visual comparison. Sareen, Sapre, and Selig note the small increase in drag, compared to the clean c_l vs c_d data, due to the presence of the tapes. They attribute it to the backward-facing step that causes early flow transition - as boundary-layer theory indicates is true for a step height of a certain size. Additional results for all tape configurations are summarized in the table below (Fig. 1.34).

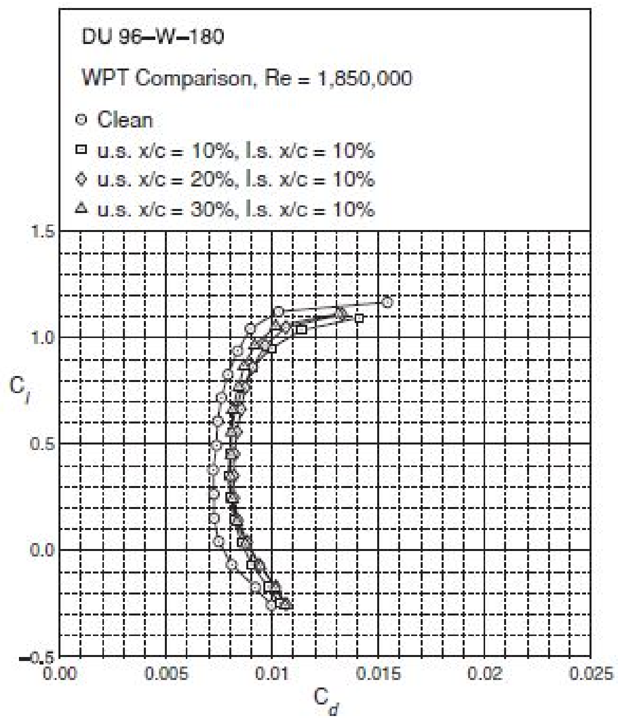

Figure 1.33. Effect of LEP tape on Cl and Cd for a fixed lower surface and varying upper surface tape extent [18].

For a fixed lower surface percent coverage, drag increases as the tape extent on the upper surface moves toward the leading edge. The same can be said if the the upper surface coverage is fixed and the lower surface coverage changes. Since the backward-facing step trips the flow, it causes the boundary layer to transition from laminar to turbulent at the tape step. In general, the closer the tape is to the leading edge on either surface, the more turbulent flow there is in the boundary layer over the airfoil and the higher the drag force on the body [18].

Configuration (upper / lower)	ΔC_d	ΔC_l
10% / 10%	+15%	–0.03
20% / 10%	+12%	–0.02
30% / 10%	+6%	–0.01
10% / 20%	+13%	–0.03
20% / 20%	+8%	–0.02
30% / 20%	+5%	–0.00

Figure 1.34. Effect of LEP tape on airfoil lift and drag performance [18].

Using the data for lift and drag and the PROPID wind turbine design code, Sareen, Sapre, and Selig also estimated the effect of different tape configurations on wind turbine AEP performance. With the x/c = 20% upper and lower surface as the representative case, AEP for a 2.5 MW wind turbine decreased by anywhere from 0.3% - 0.5%, depending on the average turbine site wind speed [18]. These AEP losses, while not insignificant, are drastic improvements compared to the estimated AEP losses of almost 25% for eroded blades that Sareen, Sapre, and Selig presented in their earlier work [8].

Another relevant work on LEP tape aerodynamics is that of Giguere and Selig [19]. Rather than just testing different chord-wise tape extents, Giguere and Selig also performed tests on different airfoils, changed the total thickness of the tape, and even stagger layers of tape. Wind tunnel tests were performed on five (5) different airfoils of varying thickness and camber ratios. Tape used for testing was the 3M^{TM} 8672 polyurethane 200 μm thick tape. Several different tape configurations were considered, including one or two layers of tape, varying chord-wise extent between x/c = 5% and 30% on the upper and lower surfaces, and staggering tape layers for a two-layer case where the top layer covers x/c = 5% on the upper and lower surface, while the bottom layer covers x/c = 5% and 15% on the lower and upper surfaces, respectively (Fig. 1.35).

For one layer of tape extending to x/c = 5% and 15% chord, early transition was induced at 40% and 30% chord, respectively [19]. Note that transition does not occur at the tape step, but some distance downstream. According to boundary-layer theory, this indicates that the step for one layer is not sufficiently large to trip the boundary layer, but it does introduce enough instability into the flow to cause slightly premature transition downstream.

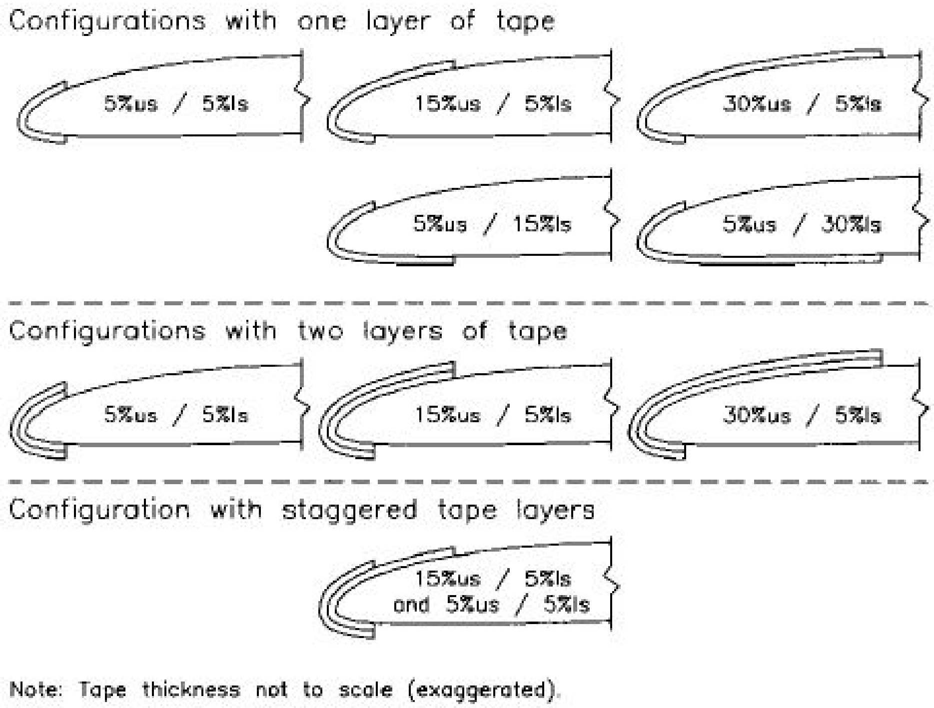

Figure 1.35. Different tape configurations studied by Giguere and Selig [19].

Looking at the effect of tape thickness, the magnitude of the aerodynamic impact increases with increasing thickness (Fig. 1.36). For the same airfoil operating at the same Reynolds number (Re = 300,000), two layers of tape have a higher drag penalty and see an additional 10% - 14% reduction in c_l/c_d compared to one layer of tape [19].

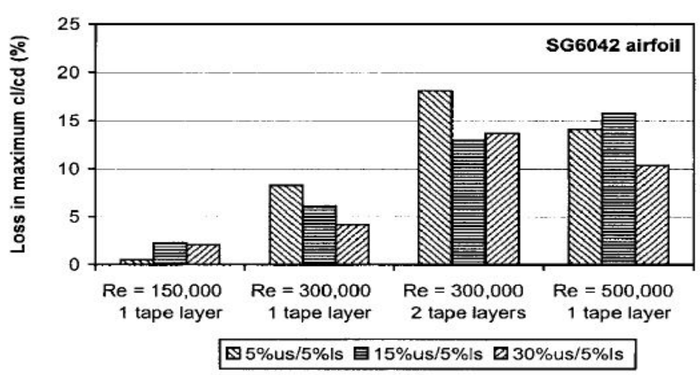

Figure 1.36. Loss of $C_{l,max}$ for the SG6042 airfoil for one or two layers of tape and as a function of Reynolds number [19].

Another interesting result is the effect of staggering the tape for cases with two layers applied. When compared to the data for one layer ending at x/c = 5% and two layers at x/c = 15% upper and lower surfaces, the data for the staggered case are comparable to both. Giguere and Selig attribute this result to the fact that the size and location of the first backward-facing step controls the drag rise [19]. They suggest that staggering the layers minimizes the size of the first disturbance and reduces the drag penalty [19]. Giguere and Selig, from their experiments with several different airfoils, note that the effect of LEP tape on wind turbine performance will vary with the size and operating conditions of the machine [19]. When it comes to the performance of a 5 kW wind turbine, losses in power coefficient are generally small since the tapes do not have a significant effect on lift [19]. Though still relatively small, losses in power coefficient jump significantly as the tape thickness increases, so Giguere and Selig recommend staggering or reducing the size of the first tape step to minimize the power coefficient penalty.

In the same study by Schramm et al. [17] referenced in section 1.4 on the impact of leading-edge erosion on wind turbine performance, the authors also include a study on the effect of leading-edge protection. The leading-edge protection tape modeled has a maximum thickness of 0.2%c at the center of the leading edge and is 0.1%c thick at the ends of the tape (Fig. 1.37).

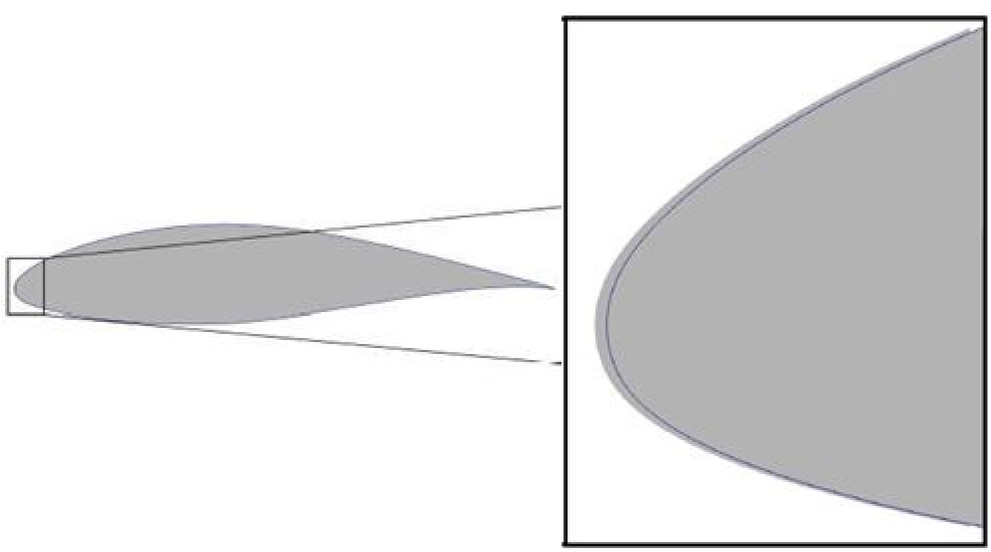

Figure 1.37. NACA 64-618 with a taped leading edge [17].

Across the range of angles of attack, the coated airfoil does not significantly under-perform compared to the clean one (Fig. 1.38). Lift reduction is observed near $c_{l,max}$ and in the post-stall region, while a slight drag increase is observed at almost all angles of attack. However, these differences are on the order of 8% - insignificant differences compared to the losses observed for eroded blades in Fig. 1.27 from the same study [17]. Compared to a 8% AEP loss and as much as 70,000 EUR/year in revenue lost to the effects of leading-edge erosion, LEP tapes only reduce AEP by 1.8%, which equates to a 15,000 EUR/year loss in revenue (using the same price per kWh of electricity) [17].

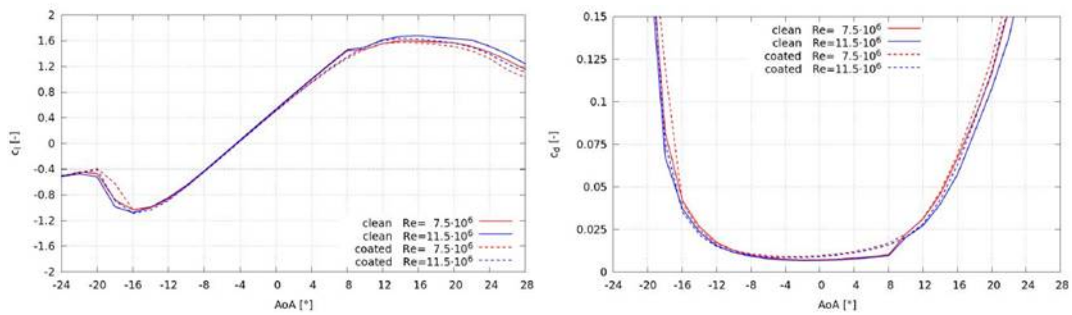

Figure 1.38. Lift and drag polars for the NACA 64-618 under clean and coated configurations [17].

Overall, compared to eroded wind turbine blades, LEP tapes do not have a significant aerodynamic impact. However, for tapes of certain configurations, the backward-facing step of LEP tapes is sufficient enough to trip the boundary layer, resulting in drag increases and lift losses, which results in notable wind turbine AEP losses. Both papers referenced above make suggestions for minimizing the aerodynamic impact of LEP tapes. Based on the same thought behind staggering tape layers to reduce the magnitude of the first backward-facing step, Giguere and Selig recommend using thinner tape, as a smaller step will minimize the additional transition-inducing instabilities introduced to the boundary-layer flow. Sapree, Sareen, and Selig recommend eliminating the backward-facing step altogether, as the sudden growth in momentum thickness in the boundary layer at the tape step is enough to initiate premature transition. Using these ideas, combined with boundary-layer theory, it may be possible to design a LEP tape with almost no impact on both 2-D airfoil aerodynamics and wind turbine AEP.

1.6 Thesis Objectives

With little literature available on the aerodynamic effect of Leading-Edge Protection (LEP) tapes on wind turbine performance, this topic is not well-studied for utility-scale wind turbines. This work seeks to investigate how changing the cross-sectional design of LEP tapes effects the aerodynamic performance and annual energy production (AEP) of a representative 1.5 MW wind turbine. The following tasks will be completed to achieve this goal:

1. Develop numerical and analytical tools to model lift, drag and pitching moment of a 2D airfoil with erosion protection tape applied to the leading edge.
2. Use the numerical model to perform a parametric aerodynamic study of erosion protection tapes by varying the following tape parameters:
    (a) Maximum thickness
    (b) Width of maximum thickness
    (c) Slope of the taper from max. thickness to minimum thickness
3. Complete wind tunnel testing using a full-scale chord model to verify the numerical predictions of standard erosion protection tapes and two (2) down-selected designs.
4. Estimate the impact on AEP of a 1.5 MW wind turbine due to the application of standard and down-selected tape designs using the wind turbine design and analysis code XTurb-PSU.
5. Compare the aerodynamic performance of tapered tapes to that of standard tapes and make final recommendations for future tape designs.

Results of the study proposed above seek to identify the tape parameter responsible for the degradation of the aerodynamic performance of rotor blades. The critical value of the design parameter at which aerodynamic performance degradation can be determined with further study, impacting the design, development, and marketing of future LEP tapes. If an aerodynamically efficient LEP tape is feasible, the expected improvement in wind turbine AEP will notably impact the success of the global wind energy market.

1.7 Chapter Summaries

Chapter 2

A Computational Fluid Dynamics (CFD) numerical model is developed to estimate the aerodynamic performance of seventeen (17) LEP tape designs. Comparisons of each design to both the clean airfoil and a standard baseline tape are presented. From the results, two (2) designs are selected based on aerodynamic performance and erosion protection capabilities. These designs are used for further numerical analysis and experimental testing.

Chapter 3

Two (2) down-selected designs are manufactured and applied to a full-scale chord model wind-turbine blade section for verification of the numerical models. Estimates for drag are compared to a clean model and a model with the standard LEP tape on the market today from 3M. A critical roughness height model is developed using wind tunnel data to quickly size the height of the backward-facing tape step for various rotor applications to prevent premature boundary layer transition for all operating conditions.

Chapter 4

Numerical aerodynamic data for the down-selected designs are used to estimate the effect of LEP tape on the AEP of a utility-scale wind turbine. Analysis is performed with the wind turbine design and analysis code XTurb-PSU. Comparisons are made to the AEP for clean blades, a turbine equipped with standard leading-edge tape designs, and a blade under eroded conditons to determine the improvement in wind turbine AEP.

Chapter 5

Using the numerical estimates of 2-D aerodynamic coefficients and annual energy production (AEP) estimates, final conclusions are made on the effect of the design parameters of interest on the performance of leading-edge protection tapes. A final recommendation for a viable tape design is made based on evidence presented. Future work to finalize the development of the new tapered LEP tape is discussed.

Chapter 2

Numerical Modeling of Leading-Edge Protection (LEP) Tape Performance

The aim of this work is to investigate, using numerical methods, the effect of changing tape cross-section parameters on the aerodynamics of an airfoil equipped with novel LEP tape designs. Using the science of boundary-layer theory and the results from previous studies of LEP tape aerodynamics, design parameters of interest are carefully chosen to determine whether or not it is feasible to design new LEP tapes to minimize or even eliminate the aerodynamic degradation of lift and drag observed with traditional LEP tapes. For this work, numerical models are developed using Computational Fluid Dynamics (CFD) to estimate 2-D lift, drag, and c_l/c_d, and how different 2-D LEP tape applications change airfoil performance.

2.1 Baseline Airfoil Selection

For later verification of the numerical estimates, EverPower Wind Holdings Inc. provided two tip sections of a utility-scale wind turbine blade. Wind tunnel models were constructed from the blade sections for subsequent testing. The effect of LEP tape is airfoil dependent [19], so to ensure accurate correlation between the wind tunnel and numerical results, the cross-section of the tip section was digitized and used as the 2-D baseline airfoil for all numerical simulations.

Coordinates of the digitized cross-section are scaled such that the airfoil has a reference chord length of c = 1 m. Use of a unit chord length allows for easy non-dimensionalization of tape parameters, such as tape extent and thickness, as well as scaling of the aerodynamic data to different Reynolds numbers. Coordinates of common tip-section wind turbine airfoils were compared to the digitized coordinates to determine the cross-sectional profile.

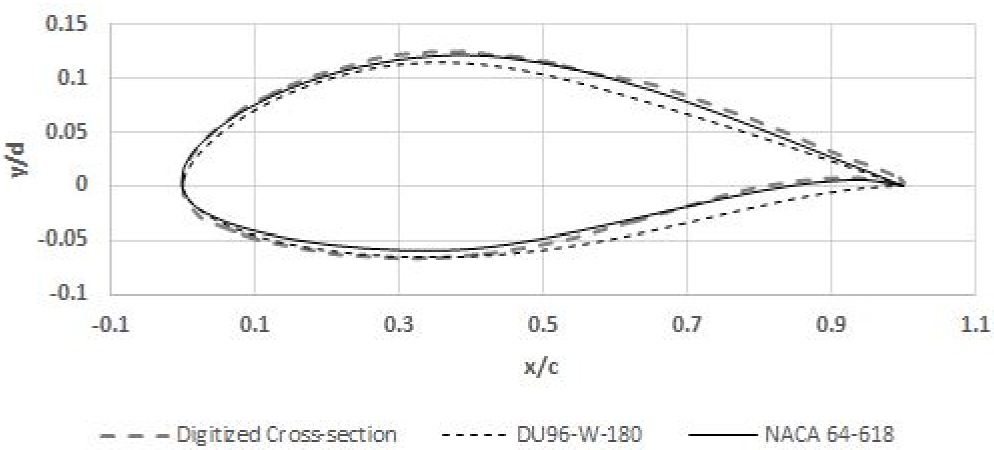

Figure 2.1. Comparison of the digitized cross-section of the full-chord model to different airfoil shapes.

The closest matches, in terms of thickness, leading-edge radius, and trailing-edge camber, are the DU 96-W-180 and the NACA 64-618 (Fig. 2.1). It should be noted that there may be some inaccuracy in the selection due to digitization error. However, based on the resulting digitized cross-section and a comparison with the DU 96-W-180 and NACA 64-618 airfoils, the closest match is the NACA 64-618. Though slight deviations are observed between the two shapes, the NACA 64-618 most closely matches the leading-edge radius, location of maximum thickness, and the trailing-edge camber of the digitized shape. The following numerical simulations will thus concern the effect of LEP tape application on the leading edge of a NACA 64-618 airfoil with wind turbine blade tip applications.

2.2 Computational Method and Domain

Estimates for lift and drag coefficients are computed using the 2-D, incompressible Reynolds-Averaged Navier Stokes equations. Numerical integration of the equations within the computational domain is performed using the commercial CFD software STAR-CCM+ [35]. The segregated solver and the $k-\omega$ SST turbulence model, without transition, are used to solve the equations and close the turbulence problem. The two-equation $k-\omega$ SST turbulence model is chosen over the other available options in STAR-CCM+ (Spalart-Allmaras, $k-\epsilon$, and the Reynolds Stress Transport model) because previous studies [16, 36] show this model is well-suited for computations related to surface roughness and boundary layer studies at a relatively low computational cost.

The computational domain is a square region of side length s = 100c (Fig. 2.2), so that there are 50 chord-lengths upstream and downstream of the airfoil leading edge to accurately approximate an airfoil in free-stream airflow. This sufficiently eliminates the effect of the far-field boundary conditions on the flow around the airfoil. The Reynolds number for all simulations is fixed at Re = $3\text{x}10^6$.

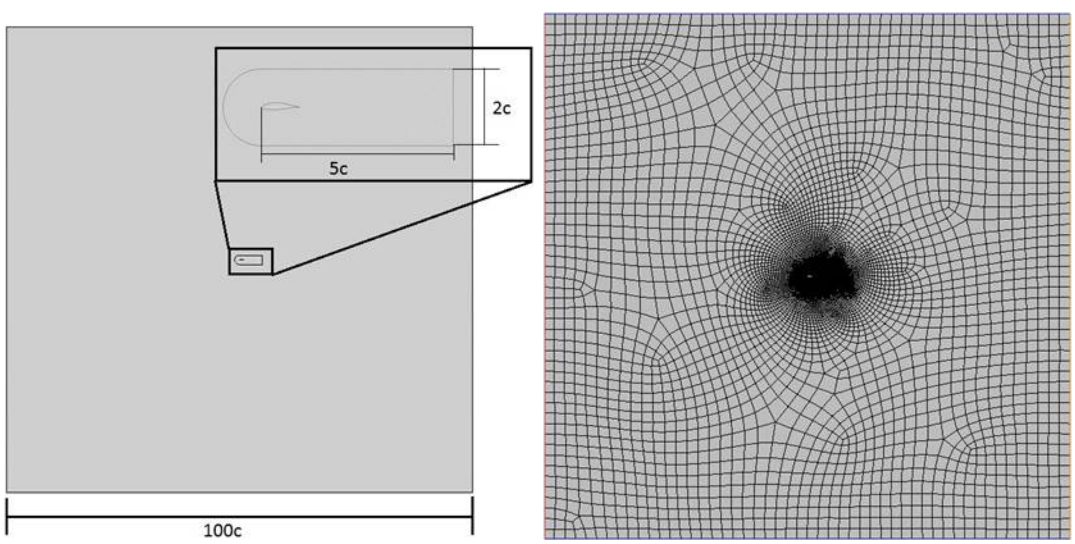

Figure 2.2. Computational domain and domain mesh.

Most of the the computational domain is discretized with an unstructured quadrilateral mesh. Total number of unstructured cells in the domain is 120,863. The unstructured mesh includes an oval-shaped surface refinement at the center of the domain around the airfoil. The size of the refined region is controlled by the angle of attack range for this study. The unstructured mesh in the refinement region gives way to a structured C-type mesh (Fig. 2.3).

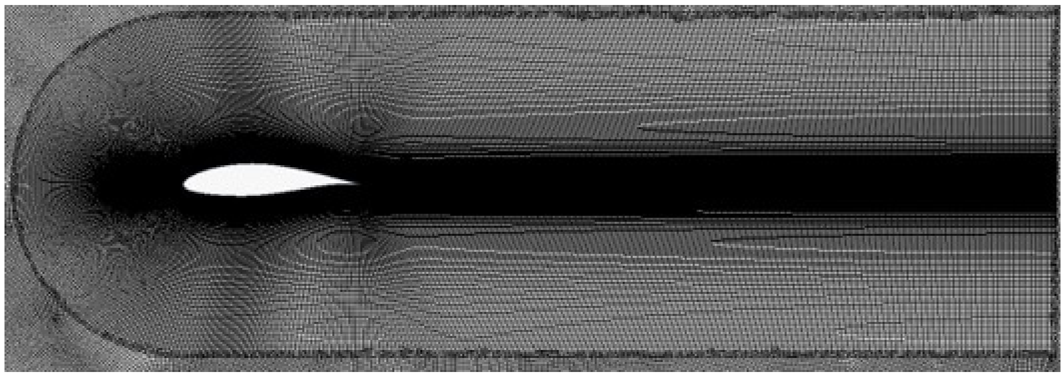

Figure 2.3. Overset mesh distribution for the clean airfoil.

The area of the C-type mesh extends for 5c from the leading edge of the airfoil and 1c above and below the airfoil. This allows for sufficient capture of the wake characteristics as well as the variant flow profile over the upper and lower surface of body with the structured mesh. Cells at the boundary of the C-type region are controlled to be of the same order of magnitude as the cells in the refinement region. The structured mesh and the unstructured mesh are merged at the C-type boarder using a least-squares approximation.

2.2.1 Grid Verification

Use of a structured mesh allows for accurate control of the first cell spacing at the surface of the airfoil, the density of the cells at the leading and trailing edges, the total number of cells around the airfoil, and the density of the wake cell count. Refinement of these parameters in the structured C-type mesh is performed until there is no appreciable change in the lift, drag, and pitching moment coefficients with further changes to the cell count. This ensures grid-independence of the results.

First cell spacing near the wall and the number of points around the airfoil were refined until no further change in the aerodynamic coefficients was observed. Initial mesh properties include 178 cells around the airfoil and a first cell spacing of 0.001 m (Fig. 2.4a). For the purposes of turbulence modeling, a wall y^+ between

30 and 45 is necessary when using the All y^+ Wall Treatment function in STAR-CCM+. The first cell height of 0.001 m corresponds to a wall y^+ near 100 for Re = $3\text{x}10^6$. To ensure a wall y^+ in the limit of that required for accurate computation using the $k - \omega$ SST turbulence model, the height of the first cell was reduced to $2\text{x}10^{-4}$ m (Fig. 2.4b) for a new wall y^+ value of 20.

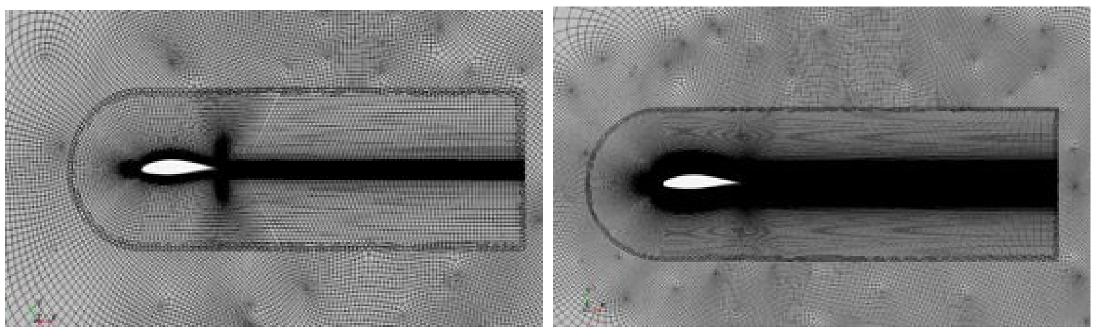

Figure 2.4. Refinement of the C-type structured mesh distribution around the clean airfoil (a) Coarse mesh and (b) Fine mesh.

Convergence of the airfoil aerodynamic coefficients for increasing number of cells around the airfoil is shown in Table 2.1. There is no change observed in c_l, c_d, and c_m when increasing the number of cells from 384 to 512. To save computation time, 384 cells are used around the airfoil.

# Wrap-Around Points	178	384	512
c_l	0.4332	0.4338	0.4338
c_d	0.012	0.01191	0.01191
c_m	-0.1062	-0.10626	-0.10626

Table 2.1. Convergence of lift, drag, and pitching moment at α = 0° for increasing number of wrap-around points over the airfoil.

With grid independence confirmed, the final number of cells in the C-type structured region is 116,280, for a total of 237,143 cells in the domain. A polar, used as a baseline for later comparison, is then generated from α = -2° to 8°. Data for a wide range of angles of attack is not necessary for the purpose of this work. The operational angle of attack for the tip section of a wind turbine blade is anywhere between -2° to 8° across the range of wind speeds. Computational time is also saved by only generating data in this limited range of angles of attack.

For initial verification of the chosen numerical models and discretization scheme of the computational domain, the generated polar is compared to the experimental wind tunnel data presented by Abbott and von Doenhoff (Fig. 2.5)[20]. Compared to the experimental data, also taken at Re = $3x10^6$, lift coefficient is well-predicted by the CFD model at low angles of attack (Fig. 2.5a).

Across the range of angles of attack considered, the numerical model significantly over-predicted the drag coefficient. For early analysis, transition modeling is not included in the computational scheme due to the high computational time cost required. The NACA 6-series airfoils, to which the NACA 64-618 belongs, are designed for long runs of laminar boundary-layer flow over the upper and lower surfaces. The result is an airfoil with a relatively high $C_{l,max}$ and low $C_{d,min}$ due to the long laminar boundary layer. Without a transition model, the boundary layer over the airfoil is assumed to be fully turbulent. From boundary-layer theory, a turbulent boundary layer increases the friction drag over the body. The higher drag predicted by the numerical scheme can thus be attributed to the additional friction drag due to a turbulent boundary layer. Abbott and von Doenhoff also provide data for the NACA 64-618 with surface roughness applied, which is included in Fig. 2.5b. The numerical data for the fully-turbulent boundary layer matches the experimental surface roughness data at low angles of attack. There are discrepancies, however, for $c_l \approx 1$ and higher.

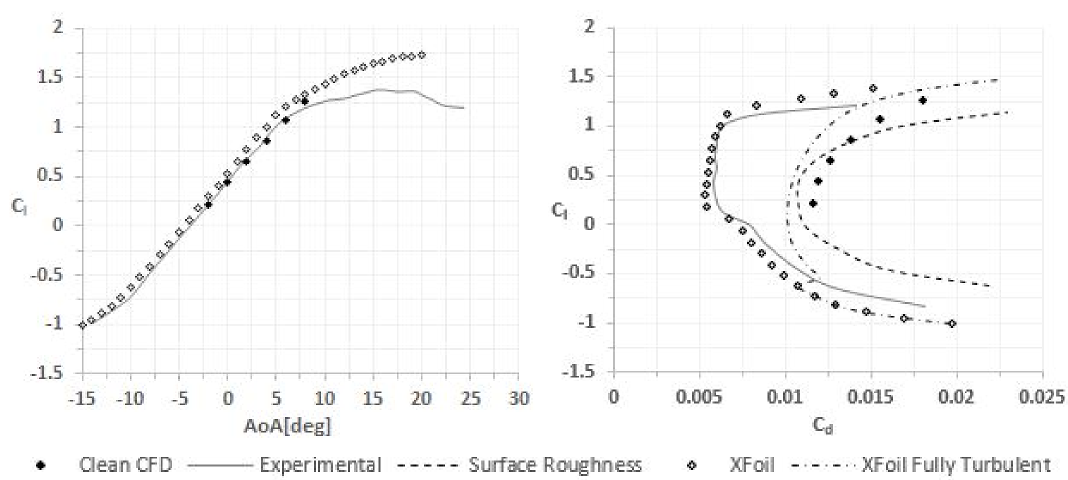

Figure 2.5. CFD lift and drag data at Re = $3x10^6$ compared to XFoil and experimental data (experimental surface data with surface roughness are taken at Re = $6x10^6$)[20].

For the purpose of this work, the numerical model is sufficiently verified. Performance of the LEP tapes, in later sections, is quantified by the percent change in lift (%Δc_l), drag (%Δc_d), and c_l/c_d ratio (%$\Delta c_l/c_d$) compared to the clean baseline airfoil data. With grid independence achieved and fairly good agreement with the verified experimental data, computation of deltas to the clean baseline data will remain consistent across the range of angles of attack and tapes tested.

2.3 Design Matrix for Parametric Study of LEP Tapes

The standard LEP tape on the market today from 3M is a tape of constant 350 μm thickness and varying widths, where the 6-in wide version is used for this study. In addition to the clean NACA 64-618 airfoil, this tape will be used as another comparison baseline to determine how the novel tape shapes perform compared to a standard tape. Two other baselines are developed for comparison and are listed in Table 2.2. Each baseline tape configuration will be used to evaluate the performance of novel tape shapes of the same maximum thickness.

W_{thick} [in]	6		
T_{thick} [μm]	200	350	500

Table 2.2. Baseline tape configurations, with no tapering, for additional performance comparison.

From boundary-layer theory and previous studies of LEP tapes, it was identified that the chord-wise extent of the tape and the height of the backward-facing step are the two parameters that dictate the impact of the tape on the aerodynamics of an airfoil. Partnering with 3M, an industry leader in LEP tape production, several cross-sectional parameters of the tapes were identified based on this methodology (Fig. 2.6). Excluded from the design matrix, however, are variations in the total chord-wise extent of the tape, W_{total}. Manufacturing methods limit width, so all tape designs considered have a fixed width of 6 inches. Should the proposed designs below eliminate the transition-inducing effect of the backward-facing step for a tape of this width, the chord-wise extent no longer impacts the performance of the tapes.

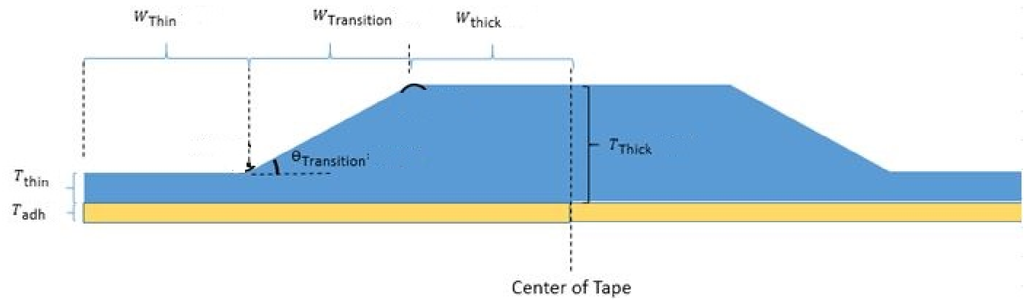

Figure 2.6. Tape cross-sectional design parameters of interest.

Parameters of interest for this parametric study are W$_{thick}$, T$_{thick}$, θ_{taper}, and T$_{thin}$. Ideally, to eliminate the effect of LEP tapes on airfoil aerodynamics, a thin tape is necessary. However, thin tapes reduce the erosion protection ability. Combining the need for erosion protection lifetime and reduced impact on the boundary layer, the novel tape designs include a region, W$_{thick}$, of sufficient thickness, T$_{thick}$, for erosion protection centered at the leading edge and taper to a thinner profile, T$_{thin}$, to reduce the effect of the tape on the boundary layer with a taper angle θ_{taper} (Fig. 2.6).

For this study, it was determined that the thickness of the thin region be fixed at T$_{thin}$ = 75 μm for all tapes. It is predicted that a step of this height should be sufficiently thin to not trip the flow at the x/c limits for a 6-inch-wide tape. Because the height of the step has an impact on the boundary-layer behavior, three different heights of T$_{thick}$ are tested to see if the same behavior will be observed. The standard tape thickness of 350 μm is chosen as one T$_{thick}$ value. To isolate a trend from increasing or decreasing the maximum thickness compared to the standard tapes, 200 μm and 500 μm are chosen as the two additional test cases.

Different values of W$_{thick}$ are also chosen with erosion protection in mind. Based on the extent of peak impact location from local collection efficiency and observed erosion patterns on operational wind turbine blades, W$_{thick}$ = 1 inch is chosen as the minimum width needed for erosion protection. To see if the chord-wise extent of the maximum thickness region, and increasing the erosion protection capability of the tape, also has some effect on the aerodynamics, a second W$_{thick}$ value of 2 inches is also chosen for analysis.

Values for θ_{taper} are chosen to determine trends in the degree of severity of the step transition from T$_{thick}$ to T$_{thin}$. With a sudden change in thickness, the effect of a step transition along the tape is similar to the transition from the tape to the airfoil, as already investigated by Giguère and Selig with their staggered tape configuration [19]. To minimize the effect of the transition from maximum to minimum thickness, relatively shallow taper angles are chosen. The taper angle is referenced from a line drawn along T_{thin} as shown in Fig. 2.6. The most severe angle chosen for testing is 5°, which is gradual enough to not trip the boundary layer but may still have some effect on the profile drag of the airfoil. The most shallow taper angle chosen is one in which $W_{thin} = 0$ and the tape gradually transitions from T_{thick} to T_{thin} at the very edge of the tape. This angle varies by tape design depending on the width and height of the maximum thickness region. A final angle for analysis of $\theta_{taper} = 0.5°$ is chosen between the two values to determine any trends in the effect of transition angle between the steep and gradual values.

Tape design combinations are tabulated below in Tables 2.3, 2.4, and 2.5. To simplify referencing one of the many different tape designs for the remainder of the work, the following notation is used: T_{thick}-W_{thick}-θ. The first three-digit number for T_{thick} will be either 200, 350, or 500. The second number, W_{thick}, can be either 1, 2, or 6, where 6 denotes a baseline, un-tapered tape. The final number, θ, indicates the taper angle from maximum thickness to $T_{thin} = 75\ \mu m$. Options for θ include 5, 0.5, 0 (for the baseline tapes with no tapering), or G, where G denotes the tapes with a gradual transition from maximum to minimum thickness. For example, a tape with $T_{thick} = 350\ \mu m$, $W_{thick} = 2$ inches, and a gradual taper is denoted as 350-2-G.

T_{thick} [μm]	200					
W_{thick} [in]	1			2		
θ_{taper} [deg]	5.0	0.5	0.134	5.0	0.5	0.160

Table 2.3. Matrix of designs for $T_{thick} = 200\ \mu m$

T_{thick} [μm]	350					
W_{thick} [in]	1			2		
θ_{taper} [deg]	5.0	0.5	0.295	5.0	0.5	0.351

Table 2.4. Matrix of designs for $T_{thick} = 350\ \mu m$

T_{thick} [μm]	500					
W_{thick} [in]	1			2		
θ_{taper} [deg]	5.0	0.5	0.456	5.0	0.543	—-

Table 2.5. Matrix of designs for T_{thick} = 500 μm

2.4 Analysis of Tape Designs

When applied to the leading edge of the NACA 64-618 airfoil, a 6-inch-wide tape has an approximate chord-wise coverage of x/c = 0.056. Examples of the tapes applied to the leading edge of the NACA 64-618 airfoil are shown in Fig. 2.7.

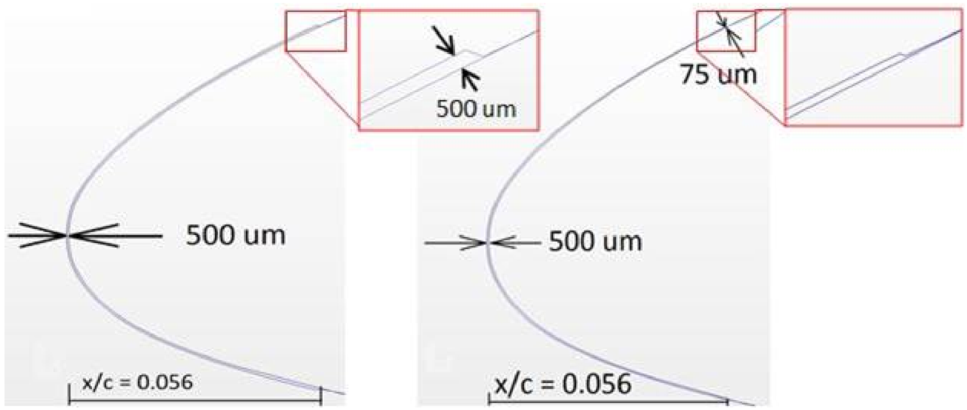

Figure 2.7. Example applications of a standard and a tapered LEP tape on the leading edge of the NACA 64-618.

In this example, compared to the standard tape of 500 μm thickness, the tapered profile is barely indistinguishable from the airfoil at the backward-facing step. The goal of the following analysis is to determine if this reduction in the tape profile is sufficient to reduce or even eliminate the impact of LEP tapes on the airfoil boundary layer.

2.4.1 Tape Grid Verification

Boundary-layer flow properties such as velocity and pressure, which determine the type of boundary layer over the airfoil surface and thus the forces on the airfoil, experience a sudden jump at the backward-facing step of the tape. With the addition of the tape to the 2-D airfoil cross-section, additional grid refinement is performed at the tape step to capture the flow phenomenon there with sufficient accuracy. Grid refinement around the tape step includes the number of cells across the tape step and the growth rate of the cells to the left and right of the step.

For all tapes, the step is not modeled as a sharp 90° transition, but rather as a 45° transition angle. Realistically, tape edges are unlikely to be perfectly square due to manufacturing tolerances. Additionally, the 45° step is easier to mesh in STAR-CCM+ using the directed mesh function where the structured grid is generated by-hand, and this angle still provides a sharp transition from the tape to the airfoil to accurately model the effect of real LEP tape.

The refinement procedure was conducted using the 350-6-0 as a representative sample where mesh results from this study are easily scaled to steps of different sizes. The first mesh iteration included a single cell spanning the tape step (Fig. 2.8a) with no alteration to the cell size upstream and downstream of the step. Starting with one cell over the tape step, cell size increases at a 1.2 growth rate for 14 cells upstream and downstream of the tape step to smooth the transition between the flow across the step (Fig. 2.8b). A final refinement added a second cell across the tape step while maintaining a cell growth rate below 1.2.

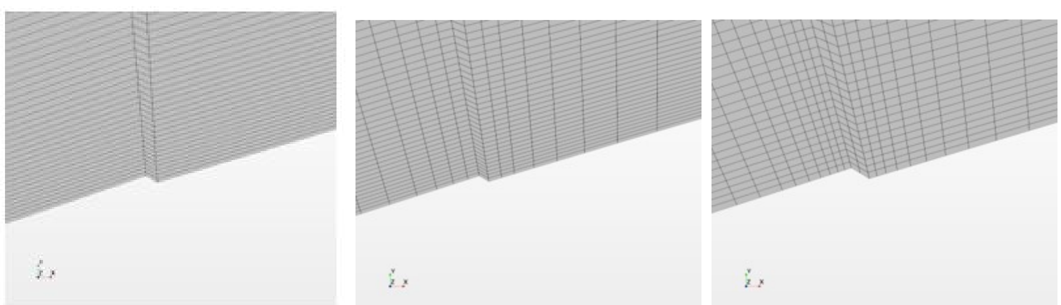

Figure 2.8. Mesh refinement over the backward-facing step of the 350-6-0 tape for (a) no refinement left and right of the step the step (b) one cell across the step with a 1.2 growth rate left and right (c) two cells across the step with a 1.2 growth rate.

Aerodynamic coefficients, at $\alpha = 0°$, for increasing cell number across the step and decreasing growth rate upstream and downstream of the step are tabulated below (Table 2.6). Two cells across the tape step falls between the underestimated values with no refinement and the over-estimated values for one step and a large cell growth rate upstream and downstream of the step. Further refinement beyond two cells across the step for a step height of 350 μm resulted in negligible difference between the values for the aerodynamic coefficients.

	No Refinement	One Cell	Two Cells
c_l	0.4605	0.4676	0.4645
c_d	0.01295	0.01224	0.01252
c_m	-0.1045	-0.1059	-0.1055

Table 2.6. Change in aerodynamic lift coefficients for mesh refinement across the backward-facing tape step.

The structured C-type mesh for an airfoil with LEP tapes applied is included in Fig. 2.9. Compared to the structured mesh for the clean NACA 64-618 airfoil (Fig. 2.3), a second dense clustering of cells is required on the upper and lower surfaces at the backward-facing step of the tape due to the mesh refinement study. Final meshes over tape steps of different heights are also included in Fig. 2.9.

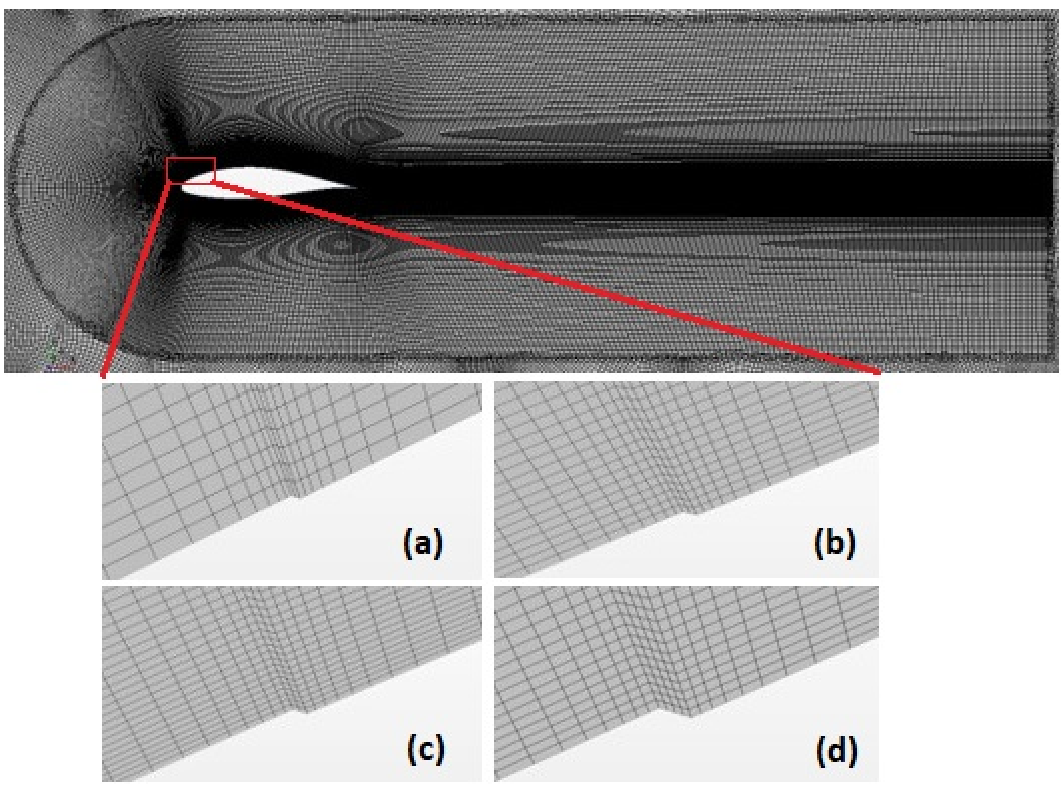

Figure 2.9. Structured C-type mesh for and airfoil with LEP tape including mesh specifics for a (a) 75 μm, (b) 200 μm, (c) 350 μm, and (d) 500 μm step height .

2.4.2 Aerodynamic Performance of LEP Tapes

Performance of the novel LEP tape designs outlined above is determined by the change in c_l, c_d, and c_l/c_d relative to two baselines. The novel tapes are compared to their respective standard LEP tape baseline of the same maximum thickness and to the performance of a clean airfoil.

2.4.2.1 Lift, Drag, and c_l/c_d

Comparison to an airfoil with a standard LEP tape applies is determined via

$$\%\Delta = \left(\frac{Standard - Tapered}{Standard}\right) * 100 \tag{2.1}$$

Assuming LEP tape is going to be used on a wind turbine blade, comparing the novel LEP tape designs to their respective standard LEP tape baseline determines the improvement in the aerodynamic performance of the sectional airfoil by switching to the novel LEP tapes. For the novel LEP tapes of T_{thick} = 200 μm, a negligible increase in the lift coefficient is observed (Fig. 2.10a). Across the operational range of this airfoil, only a 0.2% to 0.5% increase in lift compared to the standard 200-6-0 LEP tape occurs as a result of tapering the LEP tape profile. The observed variation in c_l increase is relatively constant over the angle of attack range, though slightly more c_l increase compared to the standard LEP tape is observed at higher angles of attack.

The effect on drag reduction compared to the standard LEP tapes is considerably larger for the family of 200 μm thick novel LEP tapes (Fig. 2.10b). Drag decreases 0% to 0.2% compared to the standard 200 μm thick LEP tape when tapering is applied. Combining the overall effect of tapering on c_l and c_d, c_l/c_d increases 0.05% to nearly 0.3% if a 200 μm thick tape is tapered.

Little difference in performance is observed when the design parameters of interest are isolated for comparison. Increasing W_{thick} from 1 inch to 2 inches has a small effect, showing slightly higher c_l increase, c_d reduction, and overall c_l/c_d increase compared to a tape of the same taper angle. With changes in aerodynamic performance at this order of magnitude, however, those differences are small and indicate the family of 200 μm tapes do not demonstrate significant performance change for different taper configurations.

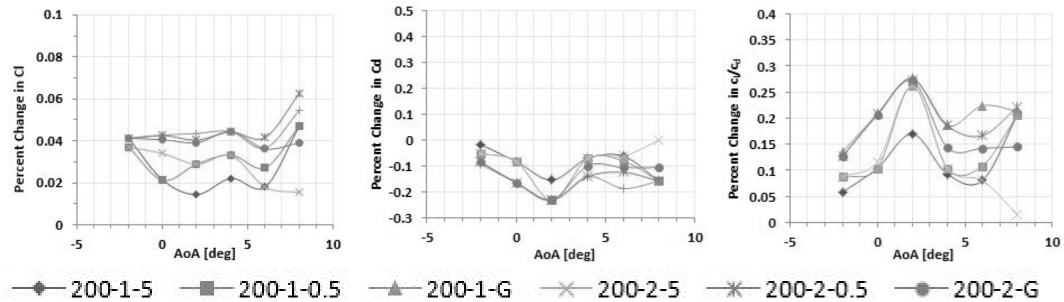

Figure 2.10. Aerodynamic performance of 200 μm thick tapes compared to the 200 μm baseline tape (a) $\%\Delta c_l$ vs α (b) $\%\Delta c_d$ vs α, and (c) $\%\Delta c_l/c_d$ vs α, fully turbulent, Re = $3x10^6$.

Looking at the effect of tapering on a standard LEP tape of 350 μm (Fig. 2.11), performance benefits are more significant and clear patterns emerge. Compared to standard LEP tapes, tapered 350 μm tapes demonstrate an increase in lift of 0.3% to 0.7%, drag decreases of 1.5% to 2.5%, and an overall c_l/c_d increase of 1.75% to 3%. The highest performing tape is the 350-2-0.5 taper configuration. However, the results are so closely clustered that even the tape with the lowest increase in c_l/c_d compared to the standard LEP tape would still make an excellent choice for a commercial product. The upward trend in c_l/c_d with angle of attack also indicates that the tapered LEP tapes have more benefit at higher angles of attack where standard LEP tape is most destructive to airfoil performance [19]. Similar to the case with the tapered 200 μm tapes, the range of deltas at one angle of attack between taper configurations is small, on the order of a 0.5% difference which is a whole order of magnitude less than the global change in lift, drag, and c_l/c_d.

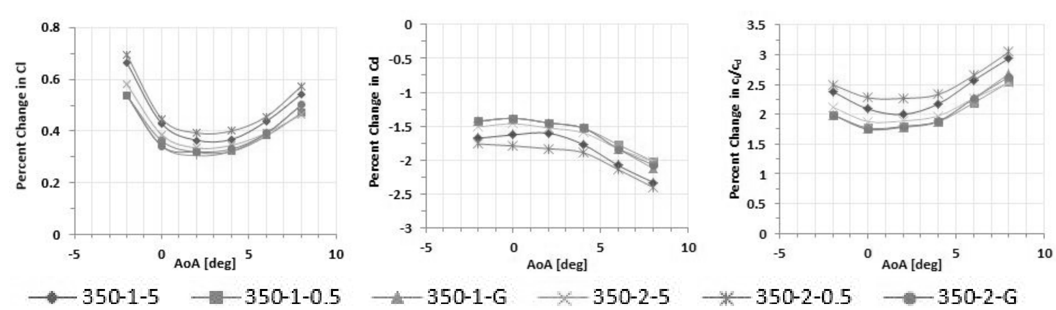

Figure 2.11. Aerodynamic performance of 350 μm thick tapes compared to the 350 μm baseline tape (a) $\%\Delta c_l$ vs α (b) $\%\Delta c_d$ vs α, and (c) $\%\Delta c_l/c_d$ vs α, fully turbulent, Re = $3x10^6$.

Finally, tapered LEP tapes of 500 μm maximum thickness display performance improvements of the same magnitude as the tapered 350 μm LEP tapes (Fig. 2.12). Lift increases compared to the a standard LEP tape of 500 μm maximum thickness range from 0.05% to 0.2% across the range of angles of attack considered. Drag reduction due to tapering varies from 0.2% to 0.8%. Overall c_l/c_d of an airfoil with a tapered LEP tape of 500 μm maximum thickness increases 0.3% to 1.0% compared to an airfoil with a standard LEP tape applied. Similar to the results in Fig. 2.11, tapering the LEP tape shows improved performance at reducing the magnitude of aerodynamic degradation as angle of attack increases.

Little difference in c_l, c_d, and c_l/c_d is observed here between each tape configuration at a constant angle of attack. The same trend was observed across all tapered LEP tapes of different maximum thicknesses, indicating that W_{thick} and θ_{taper} do not play a role in the results. The variation in the magnitude of the lift increase, drag decrease, and overall c_l/c_d increase compared to a standard LEP tape baseline is controlled by T_{thick} and the change in size of the backward-facing step between the standard and tapered LEP tapes.

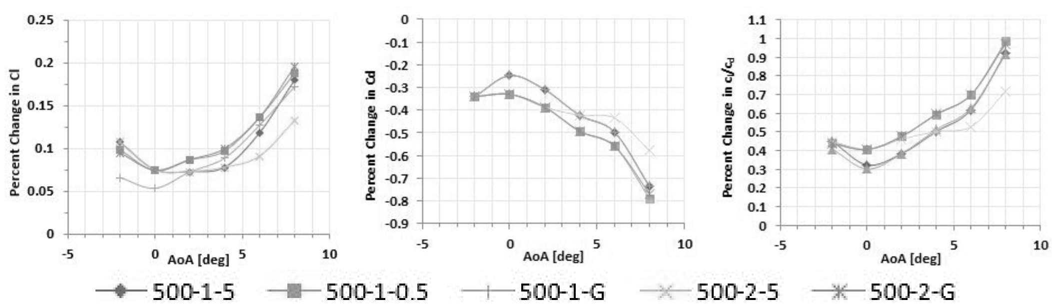

Figure 2.12. Aerodynamic performance of 500 μm thick tapes compared to the 500 μm baseline tape (a) $\%\Delta c_l$ vs α (b) $\%\Delta c_d$ vs α, and (c) $\%\Delta c_l/c_d$ vs α, fully turbulent, Re = $3x10^6$.

Comparison of the aerodynamic impact of the novel LEP tapes to the performance of the clean NACA 64-618 airfoil determines if tapering the LEP tape eliminates the effect of LEP tape application on a 2-D airfoil section. Similar to the comparison between tapered and standard LEP tapes, the change in c_l, c_d, and c_l/c_d between airfoils with tapered LEP tape applied and the clean airfoil are determined via

$$\%\Delta = \left(\frac{Clean - Taper}{Clean}\right) * 100 \tag{2.2}$$

Across the design matrix, little variation is observed between tapered LEP tape profiles with respect to the change in airfoil performance compared to a clean airfoil. For tapes of all maximum thicknesses, the addition of the LEP tape increases the 2-D c_l compared to the clean value by 2% to 15%, though that effect diminishes quickly as angle of attack increases. The largest percent lift increase of 15% occurs at α = -2°. This angle of attack is near the zero-lift value, which is α = -4° for the NACA 64-618 airfoil. At this angle of attack, the clean airfoil is more sensitive to even the smallest change in lift, explaining why Eq. 2.2 yields such high values at α = -2°.

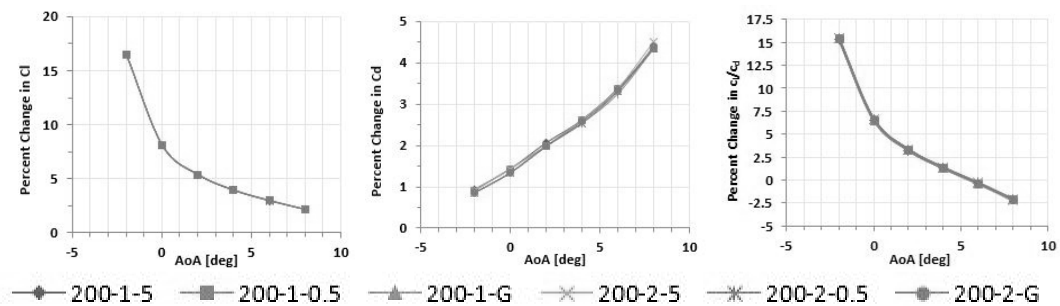

Figure 2.13. Aerodynamic performance of 200 μm thick tapes compared to clean baseline (a) $\%\Delta c_l$ vs α (b) $\%\Delta c_d$ vs α, and (c) $\%\Delta c_l/c_d$ vs α, fully turbulent, Re = 3x10^6.

Though the tapered LEP tapes decreased the airfoil drag compared to a standard LEP tape, significant drag increases are observed for an airfoil with a tapered LEP tape applied compared to the clean airfoil. Drag increases between 1% and up to 5% in the case of the family of 350 μm tapered LEP tapes (Fig. 2.14b). The impact of the tapered tapes noticeably increases with angle of attack as well for all tapes.

As angle of attack increases, the magnitude of the impact of tapered LEP tapes notably degrades 2-D airfoil c_l/c_d (Fig. 2.13c, 2.14c, and 2.15c). At low angles of attack, slight increases in c_l/c_d are observed where drag degradation is low and lift increases compared to the clean baseline are still relatively high. As angle of attack increases, airfoil drag increases significantly, while the increase in airfoil lift

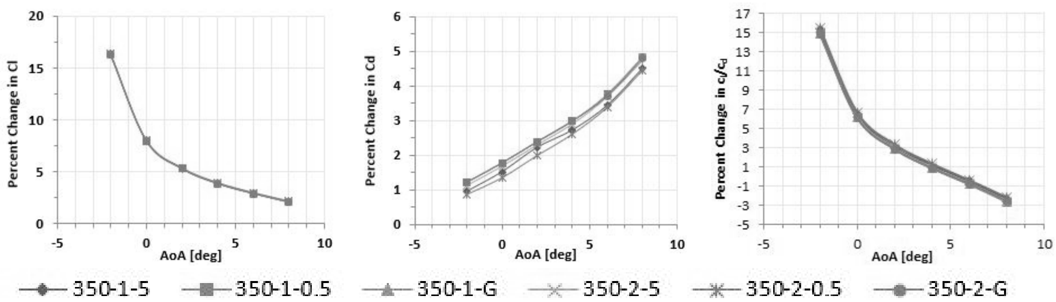

Figure 2.14. Aerodynamic performance of 350 μm thick tapes compared to clean baseline (a) $\%\Delta c_l$ vs α (b) $\%\Delta c_d$ vs α, and (c) $\%\Delta c_l/c_d$ vs α, fully turbulent, Re = 3x10^6.

drops. The result is actually a loss in c_l/c_d of up to 2.5% due to the application of a tapered LEP tape.

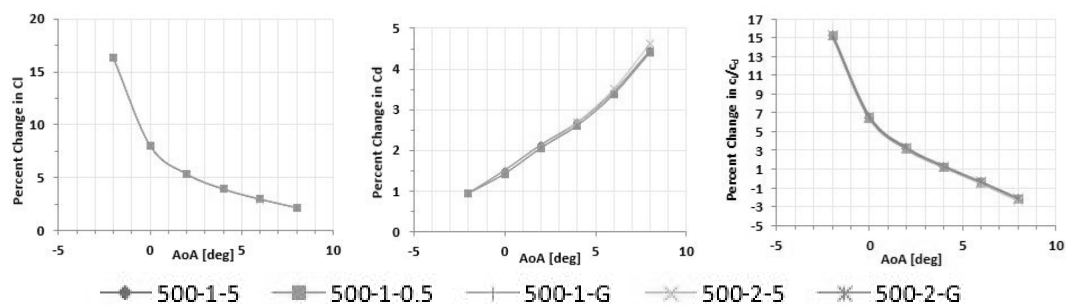

Figure 2.15. Aerodynamic performance of 500 μm thick tapes compared to clean baseline (a) $\%\Delta c_l$ vs α (b) $\%\Delta c_d$ vs α, and (c) $\%\Delta c_l/c_d$ vs α, fully turbulent, Re = 3x10^6.

From initial results of the change in 2-D aerodynamic coefficients, tapering LEP tapes has some benefit. Compared to their respective standard LEP tapes, tapering results in an increase in airfoil c_l, lower c_d, and overall higher c_l/c_d on the order of 1% across all 17 tapered LEP tape designs considered. However, these changes in 2-D airfoil performance were not enough to minimize the impact of LEP tapes on airfoil aerodynamic performance compared to a clean airfoil. Losses in c_l/c_d are observed at high angles of attack for an airfoil with a tapered LEP tape applied compared to a clean airfoil. The significant increase in drag at higher angles of attack was still observed with tapered LEP tape application, and negates the slight lift increase predicted. Though the performance degradation is relatively small, the application of tapered LEP tape may still be detrimental to overall wind turbine performance as the operational angle of attack for a tip-section airfoil is near 6°, exactly where LEP tape application begins to result in losses in airfoil c_l/c_d.

2.4.2.2 Pressure Coefficient Plots

The shape of the pressure coefficient, c_p, distribution over the surface of the airfoil determines the aerodynamic lift and drag forces acting on the body from the magnitude of the upper and lower surface pressure differential. The differences in aerodynamic performance observed above through an examination of c_l, c_d, and c_l/c_d can thus be explained by examining representative c_p plots for the clean airfoil and an airfoil with a standard and tapered LEP tape applied. For this comparison, only LEP tapes of T_{thick} = 350 μm and 500 μm are considered due to the negligible difference observed between tapered and standard 200 μm thick LEP tapes. Tapered LEP tapes chosen for comparison are 350-2-0.5 and 500-2-G. All c_p distributions shown for comparison are at $\alpha = 6°$ - the operational angle of attack for a tip-section airfoil on a wind turbine blade.

For the standard 350-6-0 and the tapered 350-2-0.5 LEP tapes, a slightly higher suction peak and c_p distribution are observed at the leading edge at this angle of attack compared to the clean NACA 64-618 airfoil (Fig. 2.16). The slight thickening of the leading-edge with LEP tape application changes the camber line, leading to the increased suction peak. Airfoil lift is strongly dependent on the upper and lower surface pressure differential, so the 2% increase in 2-D lift observed at this angle of attack for an airfoil with LEP tape applied is explained by the change in camber.

A distinct reduction in the sharp c_p peak is also observed when comparing the 350-6-0 and 350-2-0.5 LEP tapes in Fig. 2.16. The Δc_p over the tapered 350-2-0.5 step is nearly half that of the change over the 350-6-0 step. Additionally, the c_p distribution appears undisturbed by the change in c_p over the step for the 350-2-0.5 tape, where the upper surface distribution is continuous immediately upstream and downstream of the step. That is not the case for the standard 350-6-0 LEP tape, where the effect of the larger backward-facing step causes practically a discontinuity in the c_p distribution before and after the step.

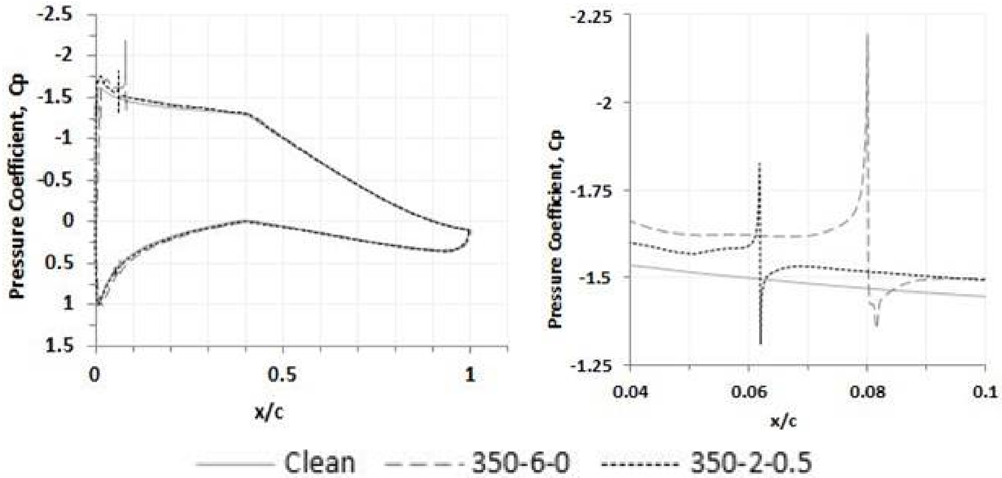

Figure 2.16. C_p distributions for 350 μm thick tapes compared to the clean airfoil at Re = 3x10^6 and $\alpha = 6°$.

The effect of the large backward-facing step is highlighted in a direct comparison of the two standard LEP tapes: 350-6-0 and 500-6-0 (Fig. 2.17). As the height of the backward-facing step increases, Δc_p over the step increases significantly as a higher c_p peak is observed for the 500-6-0 standard LEP tape. For both the 350-6-0 and the 500-6-0 LEP tapes, c_p drops suddenly downstream of the backward-facing step, explaining the significant drag increase and lift loss observed at this angle of attack compared to the clean airfoil.

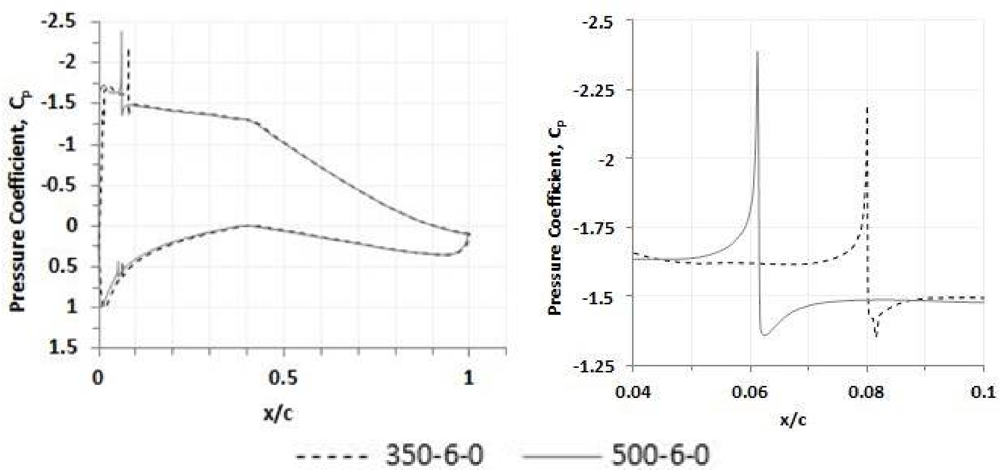

Figure 2.17. Pressure coefficient distribution for baseline tapes at Re = 3x10^6 and α = 6°.

A side-by-side comparison of the standard LEP tapes to the 350-2-0.5 and 500-

2-G tapered LEP tapes reveals the benefit of tapering and minimizing the height of the backward-facing step (Fig. 2.18). The sudden change in c_p over the tape step is reduced significantly for both tapered tapes, and it is on the same order of magnitude for both cases. There is negligible difference between the 350-2-0.5 and 500-2-G c_p distributions, indicating that the impact of a LEP tape on the 2-D aerodynamics of an airfoil is strongly dependent on the size of the backward-facing step. By tapering LEP tape, the discontinuity in c_p over the backward-facing step is eliminated, which increases c_l and decreases c_d compared to the effects of a standard LEP tape, for an overall increase in airfoil c_l/c_d.

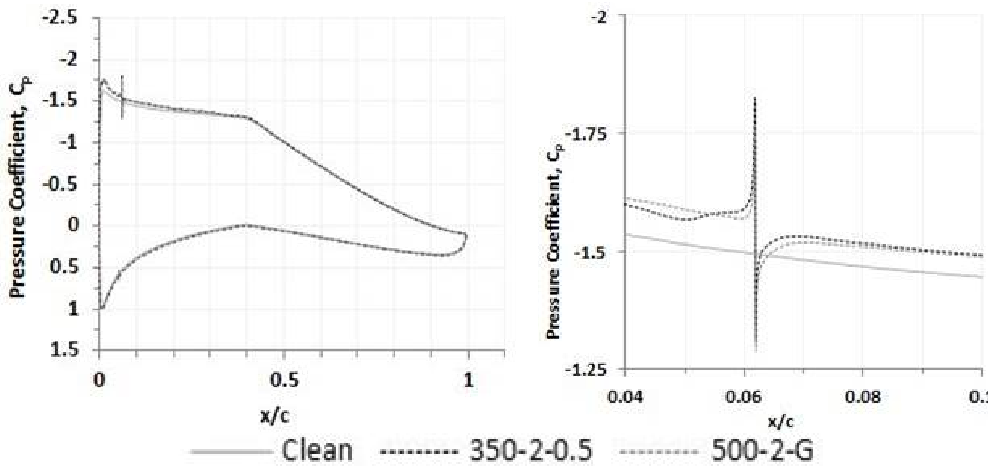

Figure 2.18. Pressure coefficient distribution for two tapered tape configurations at Re = $3\text{x}10^6$ and $\alpha = 6°$.

From the analysis of c_l, c_d, c_l/c_d, and surface c_p distributions, two LEP tapes are selected for further CFD and experimental testing. Down-selection of the designs involved a combination of aerodynamic performance and leading-edge erosion protection capability. Tapered LEP tapes of 200 μm were not considered due to a lack of erosion protection ability for such a thin tape. Tapes of $W_{thick} = 1$ inch were also eliminated from the list of possible choices as $W_{thick} = 2$ inches is preferred for maximizing the width of the protective region to cover the area of the leading edge most susceptible to severe erosion.

One tape is selected from the family of $T_{thick} = 350$ μm to provide a comparison to the standard 350 μm LEP tape on the market today. To verify any trends in increasing T_{thick}, the second tape is chosen from the family of 500 μm thick tapes. This has additional benefits because, should a 500 μm tape perform just as well as a 350 μm tapered LEP tape, erosion protection lifetime of the tape is increased with a 500 μm LEP tape. One tape was selected to have a gradual taper angle, and another with a 0.5° taper angle to confirm the negligible effect on performance of such gradual taper angles. Final tapes selected, based on erosion protection and aerodynamic performance, are therefore the 350-2-0.5 and the 500-2-G (Table 2.7).

Design:	350-2-0.5	500-2-G
T_{thick}	350	500
W_{thick}	2	2
θ_{taper}	0.5	0.543

Table 2.7. Down-selected tapered LEP tape designs for further analysis and testing.

2.5 Transition Modeling

The ultimate goal of this numerical study is to determine if the novel tape designs cause premature boundary-layer transition, which the standard tapes are known to cause. With the down-selected designs, 350-2-0.5 and 500-2-G, and their respective baseline tapes, 350-6-0 and 500-6-0, a more detailed numerical study was conducted on the boundary layer transition behavior of the tapes. If the backward-facing step height of 75 μm is below the critical roughness height at x/c = 0.056 for Re = $3x10^6$, the new tape designs are not predicted to trip the boundary layer, and airfoil lift and drag will not change drastically compared to the values for the clean NACA 64-618 airfoil.

Using the same computational scheme outlined in section 1.2, the Gamma Transition model is added to predict laminar-to-turbulent transition over the airfoil. The Gamma transition model is a simplified one-equation version of the two-equation Gamma-Re_θ transition model developed by Langtry and Menter that is coupled to the $k-\omega$ SST turbulence model. The two-equation model uses a criterion for both momentum-thickness Reynolds number and intermittency to determine if a boundary layer has transitioned from laminar to turbulent [37]. The simplified Gamma transition model only determines transition using the intermittency equation.

Intermittency, in the transition model, is used to trigger the production of turbulent kinetic energy in the boundary layer beyond the transition point [37].

The equation couples the strain rate Reynolds number and the critical Reynolds number [38] - denoted by Knox and Braslow [30] as the Reynolds number at which intermittency, via the production of new instabilities in the boundary layer, begins to grow. In the current implementation of the transition model in STAR-CCM+, once intermittency in the boundary layer reaches 1, the boundary layer is considered to be transitioned [38].

With the inclusion of the transition model, a distinct difference is immediately observed in the c_p distribution of the NACA 64-618 at the operational angle of attack of 6° (Fig. 2.19).

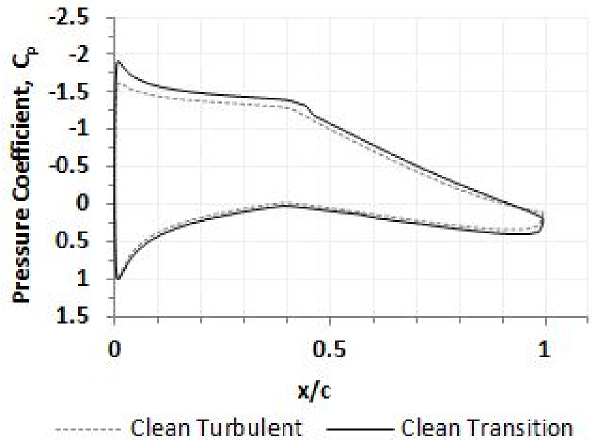

Figure 2.19. Fully-turbulent and Transition c_p for the clean NACA 64-618 airfoil at $\alpha = 6°$, Re = $3x10^6$.

Compared to the c_p distribution for a fully-turbulent boundary layer, the transition model picks up a distinct transition bubble at about 50%c. The suction peak of the airfoil is also noticeably higher when transition modeling is included. This indicates that the advantages of a laminar boundary layer on lift and drag are neglected when the simulations are run without the addition of a transition model. Fully turbulent simulation results, however, are still insightful. Analysis of fully turbulent results showed that there is negligible difference in performance relative to a clean airfoil for tapes with different maximum thicknesses, taper angles, and widths of maximum thickness. The fully turbulent results are also representative of the performance of LEP tapes after a few years in the field when the tape surface begins to deteriorate. Under damaged tape conditions, the boundary layer is fully turbulent, and CFD predicts that there is negligible difference between the performance of standard or tapered LEP tapes. Benefits of laminar-to-turbulent transition are only applicable early in the lifetime of LEP tapes when the surface remains un-damaged.

2.5.1 Grid Refinement for Transition Cases

To implement the Gamma transition model in STAR-CCM+, further grid refinement is necessary. Due to the dependence of the transition behavior on the local flow properties near the airfoil surface, more stringent requirements are placed on the size of the first cell at the wall. The transition model requires wall $y^+ = 1$ over the surface of the airfoil. To achieve this for an airfoil of chord length c = 1 operating at Re = 3×10^6, the first cell height is reduced by an order of magnitude from 2×10^{-4} m to 1×10^{-5} m. Refined structured grids in the C-type mesh for the clean and taped profiles are included in Fig. 2.20 and Fig. 2.21.

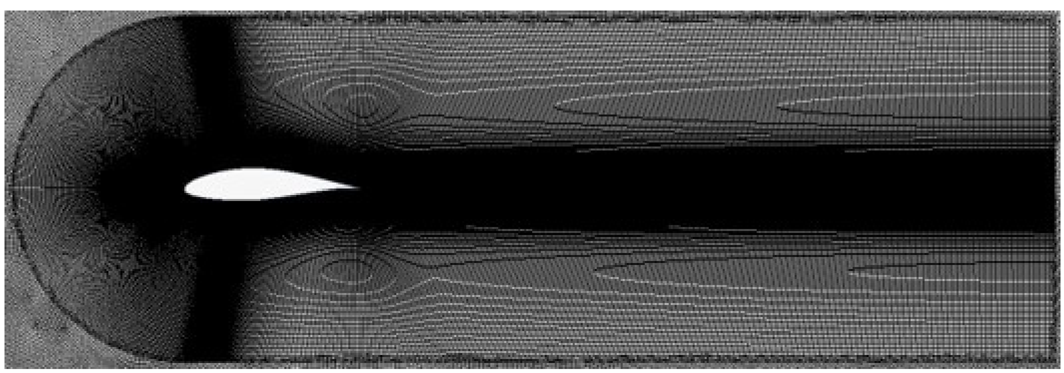

Figure 2.20. Refined overset mesh distribution for the clean airfoil for transition modelling.

A distinct increase in cell density around the airfoil is observed in the refined meshes compared to the mesh determined suitable for modeling without transition (Fig. 2.3 and Fig. 2.9). Cell density also increases on the upper and lower surfaces near the point of maximum thickness with the refined mesh for transition modeling. This is to accurately capture the transition location along the surface, which generally occurs near the maximum airfoil thickness.

To verify the validity of the refined C-type structured mesh, c_l and c_d data for the clean NACA 64-618 airfoil are once again compared to the experimental data

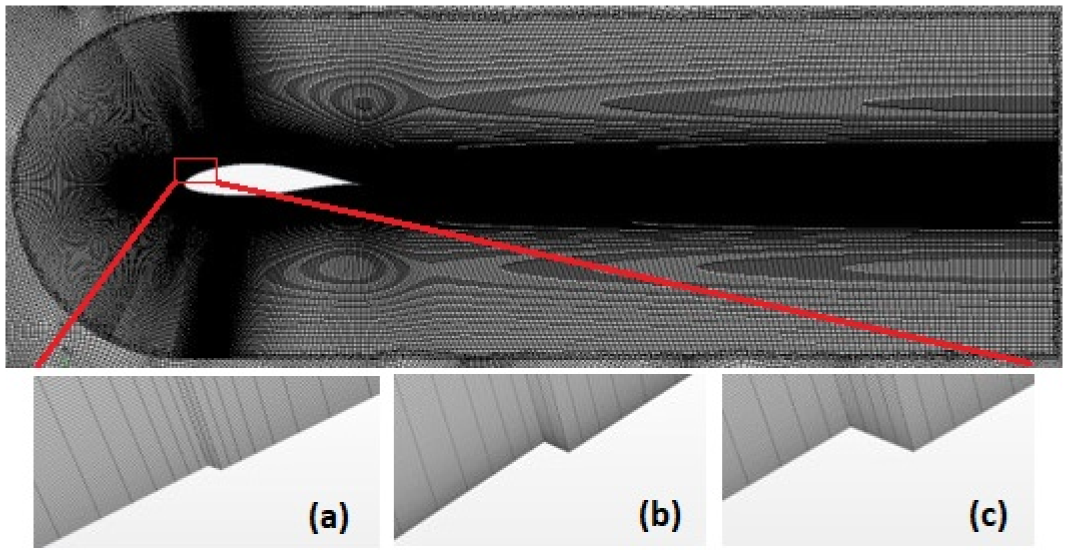

Figure 2.21. Refined overset mesh distribution for taped airfoils suitable for transition modelling and step meshes for (a) 75 μm, (b) 350 μm, and (c) 500 μm.

from XFoil and Abbott and von Doenhoff [20] (Fig. 2.22). Whereas lift was under-predicted without the transition model, lift is now over-predicted slightly, but is still close to the experimental data in the angle-of-attack range of interest to verify the accuracy of the mesh. With the transition model included, the data for c_d are now comparable to the experimental data for a clean airfoil in both magnitude of c_d and trend as angle of attack increases.

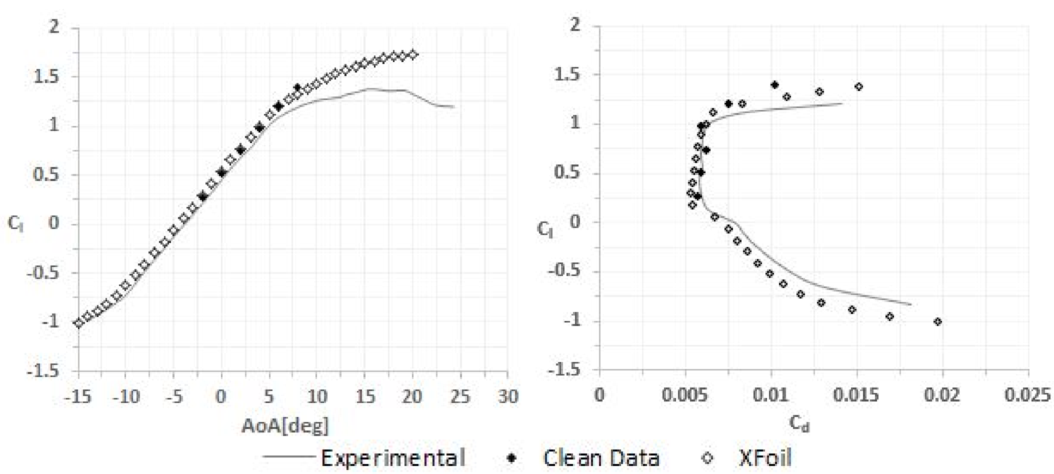

Figure 2.22. Comparison of numerical CFD data for lift and drag with transition modeling included to experimental data from XFoil and Abbott and von Doenhoff [20].

The consistency and accuracy of the mesh is verified for the clean NACA 64-618 airfoil. Applying the same mesh properties to the taped airfoils, and using the same backward-facing step meshing strategy described in Section 1.4.1, performance of the novel tapes to the clean airfoil and their respective standard tape configurations can once again be assessed to determine the effect of the tapes on boundary-layer transition.

2.5.2 Aerodynamic Performance with Transition

Similar to the analysis of various tape designs with the fully-turbulent CFD model, a number of comparisons will be made to identify the effect of different tape configurations on different flow properties. Transition behavior is identified from CFD renderings of pressure and velocity around the airfoil and intermittency in the boundary layer. Surface distributions of the pressure coefficient are compared across tapes to identify how changes in the flow field effect the pressure coefficient, which is used to calculate lift and drag forces on the airfoil. Finally, delta values for lift, drag, and c_l/c_d are presented to determine how the flow and transition phenomenon identified in the previous plots effects the aerodynamic performance of different tape designs.

2.5.2.1 Velocity, Pressure Distributions, and Intermittency

Initial effect of the tapes can be observed by examining the velocity flow field, pressure contours, and the intermittency in the boundary layer for the clean and taped profiles selected for transition modeling analysis. All observations are conducted at $\alpha = 6°$. This is the operational angle of attack for an airfoil at the tip section of a reference utility-scale 1.5 MW wind turbine blade, and the results below are thus representative of the operating conditions this airfoil will experience.

The clean NACA 64-618 airfoil displays a stagnation point on the lower surface, a velocity peak on the upper surface, and thin boundary layer that noticeably thickens beyond 50%c (Fig. 2.23). Pressure correspondingly reaches a maximum at the stagnation point and decreases over the upper surface where the flow accelerates and the highest velocities are seen. Flow remains attached to the airfoil, even up to the trailing edge, at this angle of attack.

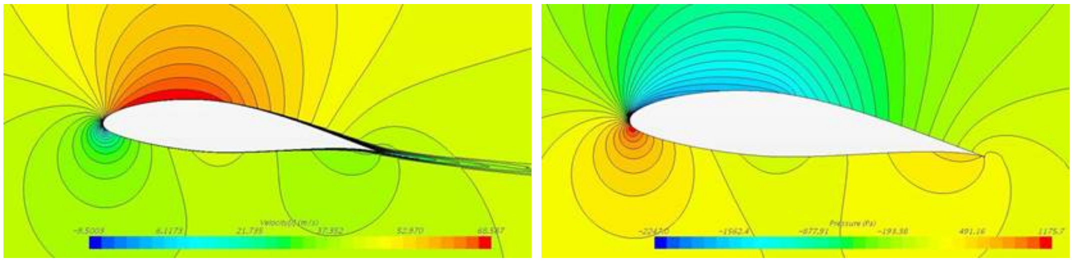

Figure 2.23. (a) Velocity and (b) pressure distributions over the clean airfoil at $\alpha = 6^{\circ}$.

The natural transition location for the clean NACA 64-618 airfoil is identified in Fig. 2.24. Transition occurs on the upper and lower surfaces via a separation bubble at roughly 50%c and 75%c on the upper and lower surfaces, respectively. The laminar boundary layer separates from the surface of the airfoil, and a turbulent boundary layer takes its place until the remaining instabilities in the laminar boundary layer cause complete transition of the boundary layer slightly downstream of the separation point.

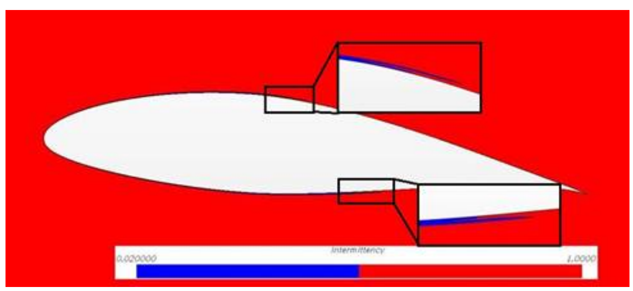

Figure 2.24. Clean NACA 64-618 boundary layer intermittency distribution.

A distinct thickening of the boundary layer velocity profile is immediately observed at this angle of attack for application of both the 350-6-0 (Fig. 2.25a) and 500-6-0 (Fig. 2.25b) to the NACA 64-618 airfoil. Looking at the velocity profile right behind the tape step, a region of stagnant flow occurs at tape steps of this height. The size of the stagnant region increases for larger steps, as observed when comparing the flow at a step height of 350 μm and 500 μm. At the tape step of a standard LEP tape, the boundary layer separates from the airfoil surface, causing the stagnant flow just behind the step.

Unlike the smooth pressure distribution over the clean airfoil, a sharp change in pressure is observed at the tape step for both standard LEP tapes (Fig. 2.26).

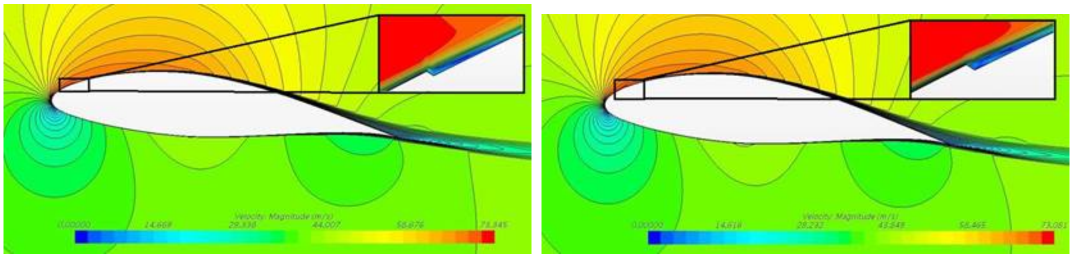

Figure 2.25. Velocity flow field over (a) 350 μm and (b) 500 μm step

The magnitude of the pressure change increases for increasing step height when comparing the distributions between Fig. 2.26a and Fig. 2.26b. This sudden drop in pressure experienced over the tape step has an additional adverse effect on the boundary layer stability, promoting early transition.

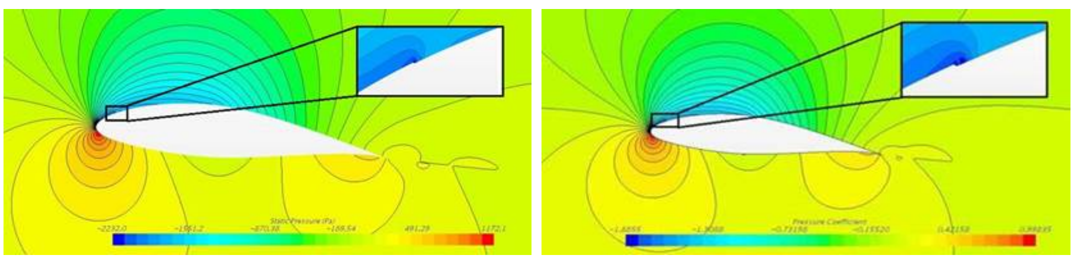

Figure 2.26. Pressure contours over (a) 350 μm and (b) 500 μm step

As expected, intermittency distributions in the boundary layer of the airfoil reveal that the boundary layer transitions prematurely at the backward-facing step on the upper surface (Fig. 2.27). The sudden change in pressure at the backward-facing step and the separation of the boundary layer from the airfoil surface introduce enough instabilities into the flow to cause premature separation. At the backward-facing step on the lower surface of the airfoil for the 500-6-0 tape, a small region of turbulent instability is introduced into the boundary-layer flow (Fig. 2.27b). Due to the size of the boundary layer on the lower surface at this angle of attack, that instability is not enough to transition the flow and the boundary layer still transitions naturally around 75%c.

By reducing the size of the backward-facing step, many of the adverse effects on the boundary-layer flow are eliminated. Compared to the velocity distributions in Fig. 2.25, there is negligible boundary-layer thickening ahead of the natural transition point for the 350-2-0.5 and 500-2-G tapes (Fig. 2.28). Velocity profiles,

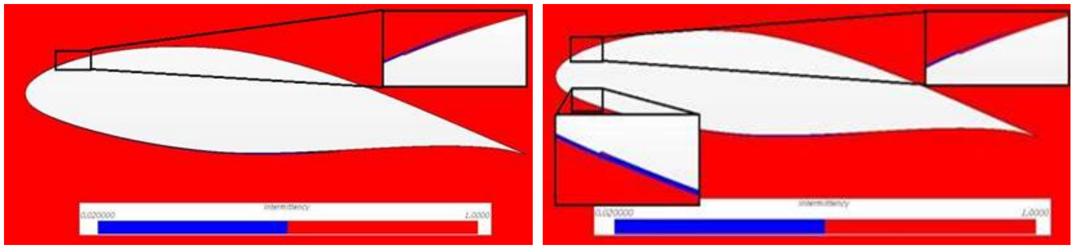

Figure 2.27. Boundary layer intermittency over (a) 350 μm and (b) 500 μm step

in distribution and magnitude, closely resemble the profile of a clean NACA 64-618 airfoil (Fig. 2.23a). The boundary layer remains attached to the surface as the flow passes over the backward-facing step. There is a slight thickening of the boundary layer closest to the surface at the backward-facing step, but this increase is not enough to separate the boundary layer from the airfoil.

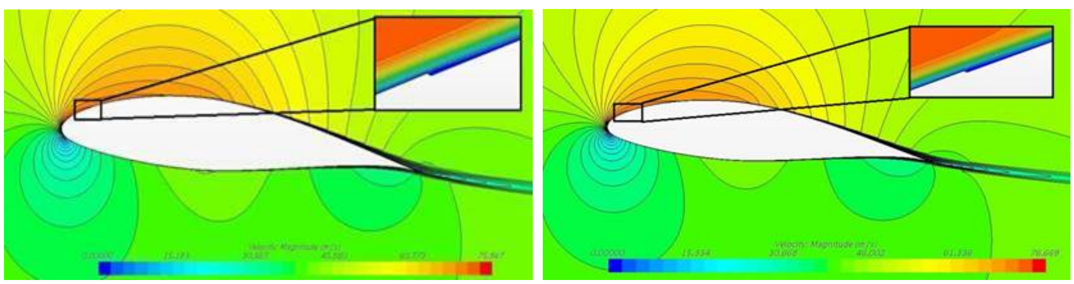

Figure 2.28. Velocity flow field over a 75 μm step for a tape of (a) 350 μm and (b) 500 μm maximum thickness

Without boundary-layer separation at the tape step, the pressure change at the tape step is eliminated. Pressure distributions are nearly constant over the backward-facing step, and any increase in pressure due to the presence of the step is small (Fig. 2.29). Maximum thickness appears to have little effect on pressure distribution at the step as the distributions are almost identical.

Reducing the size of the backward-facing tape step eliminates the boundary-layer separation and pressure drop seen in tapes with larger backward-facing steps. This reduces the transition inducing instabilities and allows the boundary layer to remain laminar until natural transition occurs at 50%c and 75%c (Fig. 2.30).

By reducing the backward-facing step height to 75 μm, the numerical model predicts that premature transition seen in standard LEP tapes is eliminated, and the flow over the airfoil surface resembles that of the clean NACA 64-618 profile.

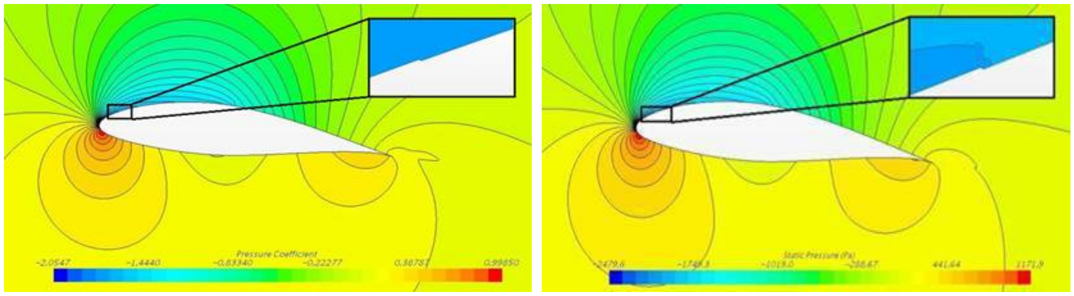

Figure 2.29. Pressure contours over a 75 μm step for a tape of (a) 350 μm and (b) 500 μm maximum thickness

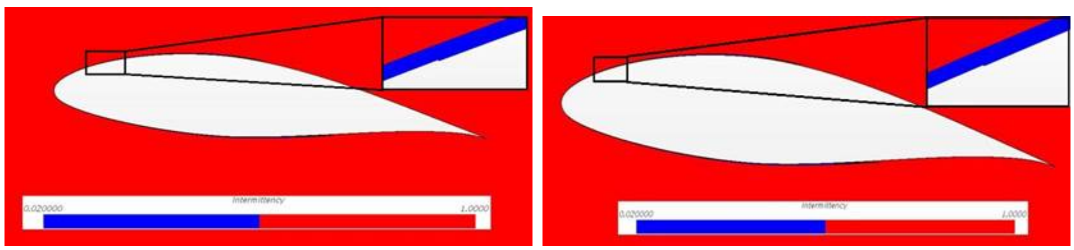

Figure 2.30. Boundary layer intermittency over a 75 μm step for a tape of (a) 350 μm and (b) 500 μm maximum thickness

Maintaining the long run of laminar flow of the NACA 64-618 by eliminating the premature transition behavior of standard tapes, a tapered LEP tape design may reduce or even eliminate the detrimental impact of standard LEP tapes on the aerodynamic performance of a wind turbine airfoil.

2.5.2.2 Transition Pressure Coefficient Plots

Changes in the boundary-layer flow profile between different tape designs are also clearly reflected in the c_p distribution over the airfoil surface. Comparing the 350-6-0 and 350-2-0.5 tapes to the clean c_p distribution (Fig. 2.31a) confirms that an airfoil equipped with the 350-2-0.5 tape performs just as well as the clean airfoil, while the 350-6-0 standard tape displays significant performance degradation. A slight thickening of the leading edge due to the application of either tape causes the slightly higher suction peak for those tapes compared to the clean distribution. The sudden pressure change over the tape step observed in Fig. 2.26a is reflected in the peak in c_p at $x/c = 0.056$. Beyond that peak, the 350-6-0 c_p distribution falls below the clean distribution along the airfoil upper surface, and the laminar transition bubble is completely eliminated - an effect of the premature transition of the flow at the backward-facing step on the upper surface.

Similar trends are observed for the 500-6-0 standard tape compared to the clean c_p distribution (Fig. 2.31b). The sharp jump in c_p denotes the sudden pressure change over the backward-facing step. Pressure fails to recover after the step due to the prematurely transitioned boundary layer, so the resulting c_p distribution along the upper surface falls noticeably below the clean distribution, and the transition bubble at 50%c is once again eliminated.

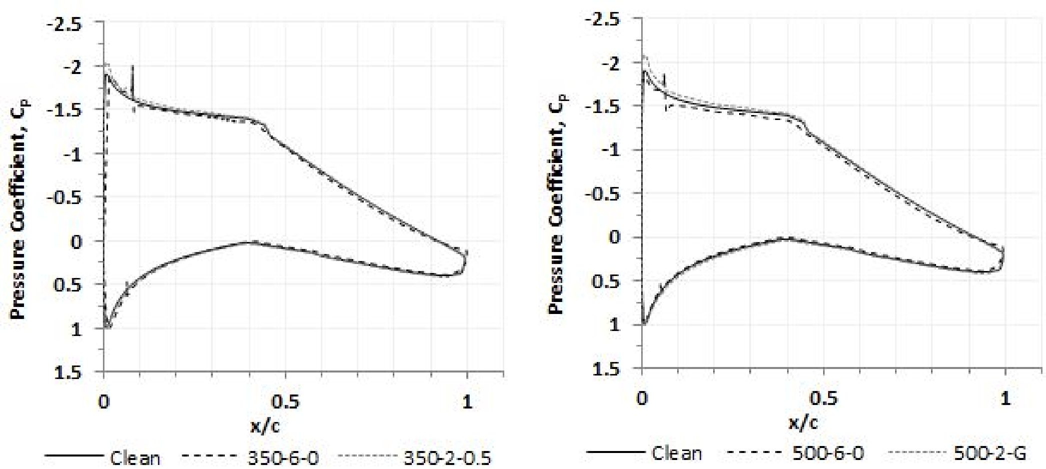

Figure 2.31. Comparison of c_p distributions between the clean, baseline, and down-selected tapered designs for 350 μm and 500 μm thick tapes at $\alpha = 6°$ and Re = 3x10^6.

For both the tapered LEP tapes, 350-2-0.5 and 500-2-G, their c_p plots closely follow that of the clean NACA 64-618 airfoil (Fig. 2.31). Unlike the standard tapes, the 75 μm tape step only causes a slight jump in c_p at the backward-facing step. The magnitude of the pressure change at the step does not change based on tape maximum thickness, indicating it is only a function of the backward-facing step height. Both tapes also exhibit a noticeable transition bubble on the upper surface at the same transition location of the clean airfoil. This indicates that the airfoil with either 350-2-0.5 or 500-2-G tape applied to the leading edge still experiences natural laminar-to-turbulent transition at this angle of attack. A final interesting feature to note in the c_p plots for the tapered profiles is the slight increase in the suction peak. Both tapes thicken the leading edge slightly where the tape reaches its maximum thickness of either 350 μm or 500 μm. This slight change in the leading-edge shape changes the camber line at the leading edge, which results in the slightly larger suction peak observed at the leading edge.

2.5.2.3 Lift, Drag, and c_l/c_d

Aerodynamic coefficients c_l and c_d are strongly dependent on the pressure coefficient distribution around the airfoil surface. The larger the difference between the upper and lower surface c_p, the higher the lift coefficient. The observed differences in the c_p distributions of both the standard LEP tapes (350-6-0 and 500-6-0) and the novel LEP tapes (350-2-0.5 and 500-2-G) indicate that there is a significant difference in expected performance based on the size of the backward-facing step.

Similar to the earlier analysis of the airfoil aerodynamic coefficients, performance of each tape design is quantified by the percent change in c_l, c_d, and c_l/c_d relative to the clean airfoil via

$$\%\Delta = \left(\frac{Clean - Tape}{Clean}\right) * 100 \tag{2.3}$$

Compared to the clean airfoil, c_l decreased anywhere from 1% to 5% for the standard 350-6-0 and 500-6-0 tapes (Fig. 2.32a). The loss in lift is expected for these tapes due to the prematurely transitioned boundary layer, which results in a slightly smaller difference between the upper and lower surface c_p distribution compared to the clean airfoil. Across the angle of attack range tested, larger c_l decreases are observed for the 500-6-0 LEP tape, which is expected due to the significantly lower upper surface c_p distribution for the 500-6-0 compared to the 350-6-0 tape. Lift increases are actually observed, on the other hand, for the tapered 350-2-0.5 and 500-2-G tapes, and range from 5% to 10% are are nearly identical for different values of maximum thickness. This is due to the slight increase in the suction peak observed for the tapered profiles. Another possibility is that the lift is slightly over-estimated in CFD. Lift of the clean baseline in CFD is over-estimated compared to the experimental data at the same Reynolds number, so it is possible that lift is over-estimated here as well.

The early onset transition of the standard tapes causes a significant increase in c_d compared to the clean airfoil (Fig. 2.32b). Drag increases range from 40% to almost 115% for standard LEP tapes, with larger drag increases observed for

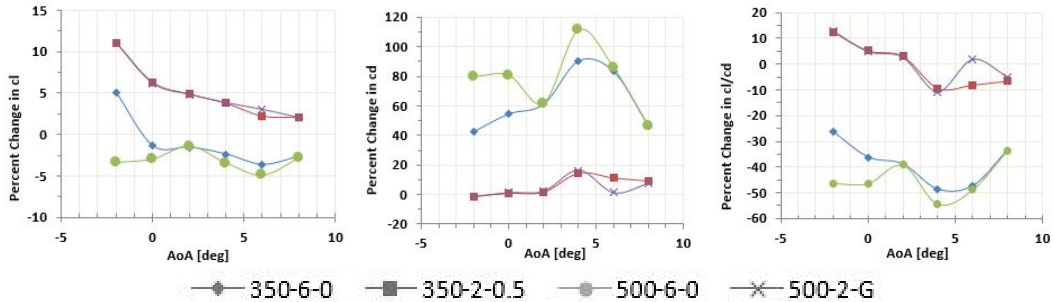

Figure 2.32. Aerodynamic performance of baseline and tapered tapes compared to the clean NACA 64-618 (a) c_l vs α (b) c_d vs α, and (c) c_l/c_d vs α with transition modeling at Re = $3\text{x}10^6$.

the thicker 500-6-0 tape due to the larger change in pressure over the backward-facing step. By comparison, c_d increases compared to the clean airfoil values are nearly eliminated for the 350-2-0.5 and 500-2-G tape designs. Drag increase is anywhere from 1% to 15%, which increases with angle of attack, and the values are comparable for tapes of different maximum thicknesses. Though transition occurs at the natural transition point, eliminating the increased profile drag of the standard LEP tapes due to a turbulent boundary layer, the slight change in pressure still observed across the backward-facing step causes the slight increase in drag.

Standard tapes, with the significant lift loss and drag increase due to early onset transition, significantly decrease the c_l/c_d of the airfoil across all angles of attack (Fig. 2.32c). Losses in c_l/c_d are anywhere from 25% to 55%, which increases with increasing backward-facing step height and tape maximum thickness. Comparatively, a nearly 12% increase in c_l/c_d is observed at low angles of attack for the 350-2-0.5 and 500-2-G tapes, but this effect diminishes as angle of attack increases, resulting a 5% to 10% loss in c_l/c_d at higher angles of attack. The benefit of increased lift diminishes as angle of attack is increased while the effect of the tapered LEP tapes on drag increases with angle of attack, resulting in the c_l/c_d losses observed beyond $\alpha = 2°$.

Relative performance of the tapered LEP tapes to their standard tape configurations can also be determined via

$$\%\Delta = \left(\frac{Baseline - Tapered}{Baseline}\right) * 100 \tag{2.4}$$

Compared to their respective baseline standard tape designs, airfoil c_l increases anywhere from 5% to 15% by simply tapering the profile and reducing the size of the backward-facing step (Fig. 2.33). Noted earlier, the 15% increase in lift is due to the sensitivity of the airfoil to small changes in lift at α = -2°. The airfoil is near the zero-lift angle of attack at α = -2°, so even a small increase in lift is large by relative comparison in this range. Profile drag is reduced by 25% to 50% compared to an airfoil equipped with a standard LEP tape. By tapering the profile of the LEP tapes, the airfoil c_l/c_d is thus increased 40% to 100% across the operating range of a wind turbine tip airfoil.

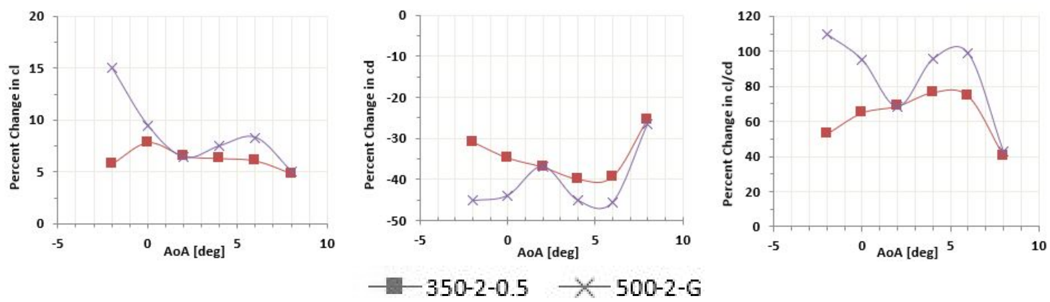

Figure 2.33. Aerodynamic performance of tapered tapes compared to their baselines (a) c_l vs α (b) c_d vs α, and (c) c_l/c_d vs α with transition modeling at Re = 3x10^6.

Including the effects of laminar-to-turbulent boundary-layer transition in the numerical model developed for LEP tape performance prediction demonstrated a significant benefit in tapering LEP tapes. For a sufficiently small backward-facing step, the boundary layer over a NACA 64-618 airfoil remains laminar until the natural transition point for all angles of attack considered here. Slight drag increases compared to a clean airfoil are still observed, however, at high angles of attack due to the effect of the LEP tape on the airfoil geometry, resulting in additional profile drag. Overall, the lift degradation and drag increase typically observed with LEP tape application on a wind turbine airfoil is nearly eliminated. By tapering LEP tapes, 2-D airfoil performance is thus comparable to the original clean airfoil.

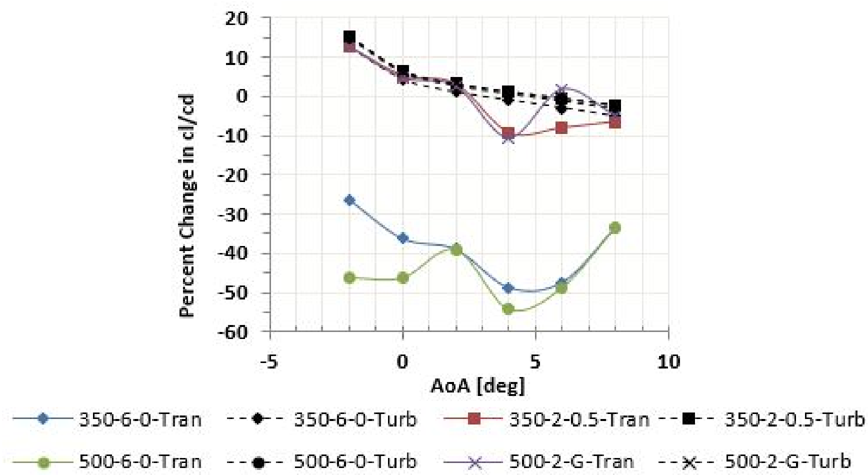

Figure 2.34. Percent change in c_l/c_d of LEP tapes compared to a clean NACA 64-618 airfoil for fully turbulent and transition modeling at Re = 3x10^6.

Comparing the CFD results with transition modeling included to the results of fully turbulent simulations represents the aerodynamic performance of LEP tapes over the product lifetime (Fig. 2.34). When LEP tapes are first applied to the rotor, the tape surface is pristine and the size of the backward-facing step controls the aerodynamic performance. After a few years of operation, the tape begins to erode, introducing significant surface defects that trip the boundary layer upstream of the backward-facing step, resulting in a fully-turbulent boundary layer. When a laminar boundary layer is present over the rotor blade, tapering LEP tapes provides notable aerodynamic performance improvements relative to standard LEP tapes by maintaining the laminar boundary layer. For a fully-turbulent boundary layer, however, the cross-sectional LEP tape profile does not impact 2-D airfoil aerodynamic performance. Despite the negligible performance difference when tapes are eroded, tapering LEP tapes still benefits lifetime aerodynamic performance by extending the operational time range over which natural laminar-to-turbulent transition occurs over the rotor blade.

Chapter 3

Verification of Numerical Models

The key leading-edge protection (LEP) tape design parameter, mentioned in [19, 18] and concluded from the CFD results, is the height of the backward-facing step. For tapes with a fixed chord-wise extent of x/c = 0.056, changes in T_{thick} and θ_{taper} have little effect on the lift and drag. Decreasing the backward-facing step height, however, demonstrates that airfoil performance close to clean conditions can be obtained. To verify the numerical performance predictions from CFD, wind tunnel experimental data are gathered for three LEP tapes of varying backward-facing step heights. With experimental data, an analytical boundary-layer method for estimating critical roughness height required to transition a boundary layer from laminar to turbulent is developed as a faster computational tool for appropriately sizing the height of the backward-facing step of LEP tapes.

3.1 Experimental Verification

Numerical results for the performance of tapered LEP tapes are verified against wind tunnel experiments using a full-scale chord model from the tip section of a wind turbine blade. Verification is achieved by comparing the change in profile drag coefficient between the clean blade section and the model with tape applied to the leading edge. Boundary-layer transition behavior is confirmed with oil visualization of the flow in the boundary layer over the upper surface of the model.

3.1.1 Wind Tunnel

Experiments are conducted in the Pennsylvania State University Low-Speed, Low-Turbulence Wind Tunnel (Fig. 3.1). It is a closed-circuit, single-return, atmospheric tunnel. The test section measures 1.013-m (39.9 in) high by 1.476-m (58.1 in) wide. Models are mounted vertically inside the test section, passing through two circular turntables that are flush with the top and bottom wall of the tunnel. The bottom of the model is attached to an electrically actuated turntable directly below the tunnel that rotates the model through a range of angles of attack. The top of the model connects to an I-beam above the tunnel. Custom wood inserts are machined to fill the gaps between the upper and lower surface of the model and the circular turntable. Remaining gaps between the wood inserts and the model are sealed with tape to prevent flow leakage into and out of the tunnel. Turbulence intensity in the test section is approximately 0.05% at 46 m/s.

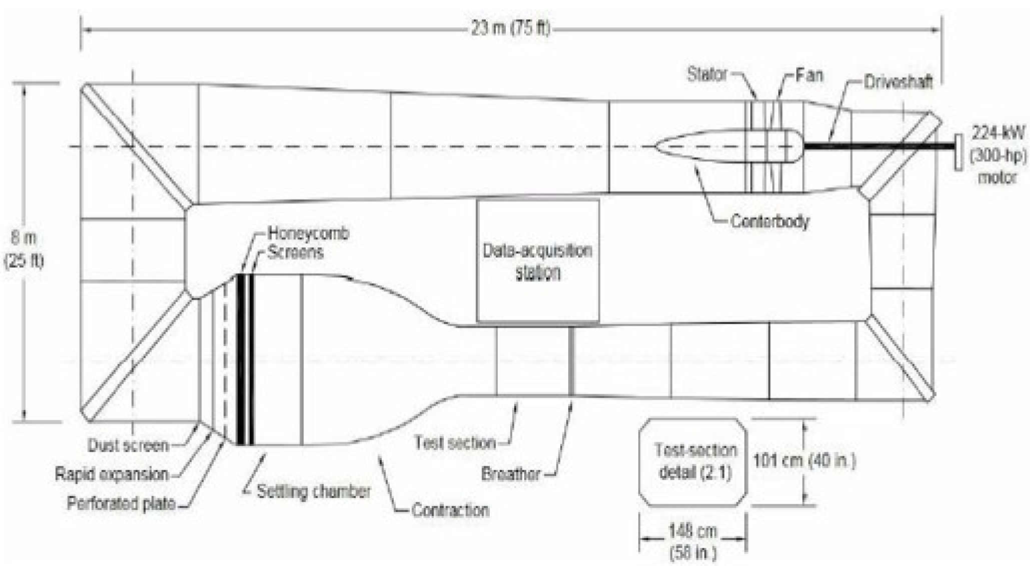

Figure 3.1. Schematic of the PSU low-speed, low-turbulence, subsonic wind tunnel.

3.1.2 Wake Probe

Drag coefficient of the full-chord model is measured with a total- and static-pressure wake-survey probe (Fig. 3.2). The probe is mounted to an actuating mechanism on the top wall of the tunnel to traverse the wake flow behind the model. It is positioned 0.53-m (21 in) from the top wall to line up with the mid-span of the model and the wake-centerline streamline. The probe incrementally traverses the width of the tunnel behind the model to survey the wake. Increment size is 1.27 mm for traversing distances less than 254.0 mm. The tip of the probe is positioned 0.3 (9-in) chord-lengths downstream of the trailing edge of the model. Tunnel and wake pressures are measured with precision transducers. Data are obtained and recorded with an electronic data-acquisition system.

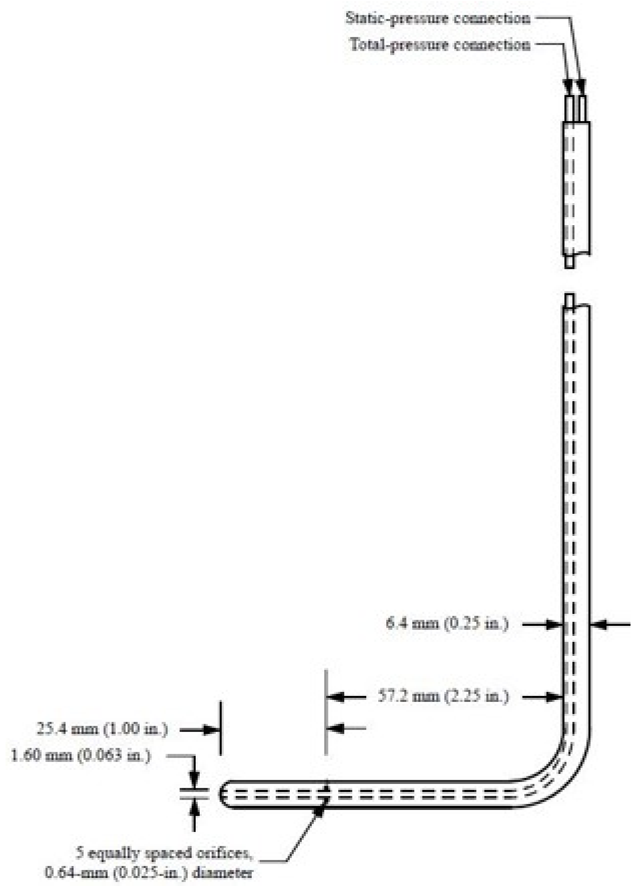

Figure 3.2. Wake probe schematic

3.1.3 Full-Scale Chord Model

A full-scale chord model is constructed for wind tunnel testing from an 8-ft tip section of a 2.5 MW wind turbine blade provided by EverPower Wind Holdings Inc. To minimize 3-D effects, a 49-in section is cut from the base of the blade to avoid the increasing taper ratio at the tip of the blade. The middle 39-in of the blade section will go into the tunnel with 5-in of the model passing through the top and bottom walls of the tunnel to connect to the mounting mechanisms. However, the chord at the top and bottom of the blade section are larger than the diameter of the holes in the top and bottom wall of the test section. To pass the model through the tunnel walls, two cuts of 5-in depth are made on the top and bottom of the model. Material is removed from the leading and trailing edges to expose the main spar, which passes through the tunnel walls and attaches to the mounting mechanisms (Fig. 3.3). The measured chords of the portion of the model inside the tunnel are approximately 34-in at the base and 29-in at the top.

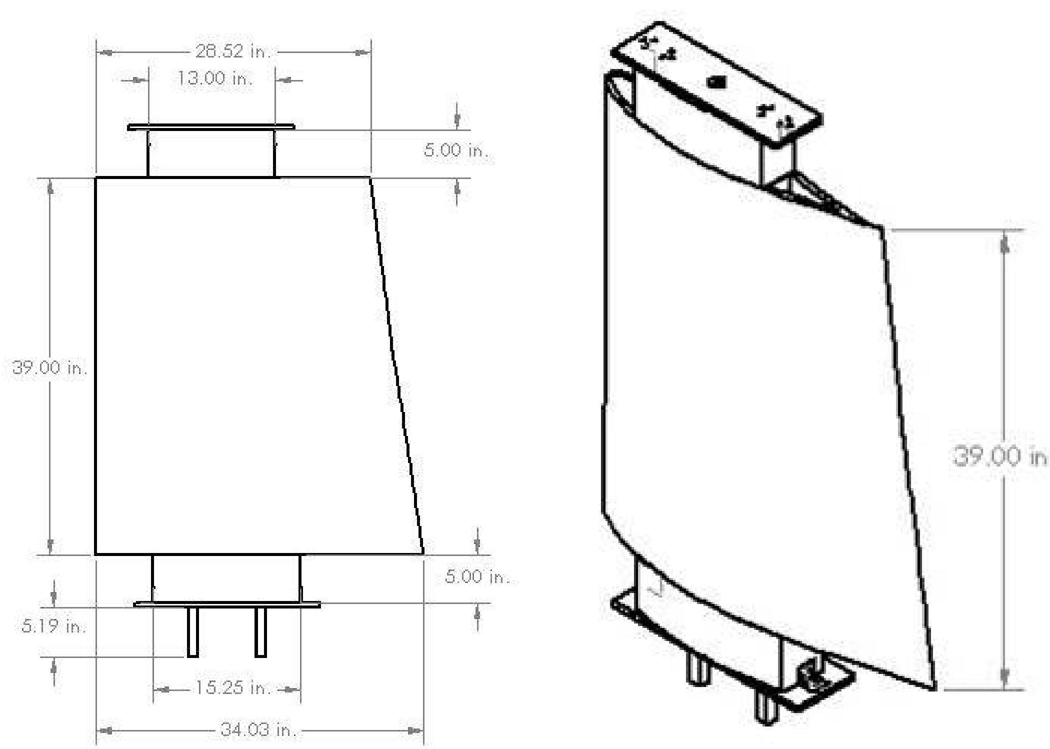

Figure 3.3. Full-scale chord wind tunnel model

To connect to the actuator disk under the tunnel and the I-beam above the tunnel, two custom 1/4-in thick steel plates are designed and mounted to the upper and lower spar (Fig. 3.4). The bottom plate has two 1.0-in^2 steel pipes welded to the surface. The pins are centered over the mid-chord of the model and spaced 6-in apart to mount into two square blocks screwed into the top of the actuator disk.

The top plate for mounting is 5-in wide and 17-in long. Four holes are drilled into the plate, spaced 5-in length-wise and 4-in width-wise, and tapped with a 1/2-in coarse thread to connect to the guidance mechanism above the tunnel. Both plates are welded to a custom frame made from 1-in^2 steel tubing that sits inside the spar cavity. The frame is epoxied and bolted to the model for stability against the high lift loads predicted for a model with such a large chord.

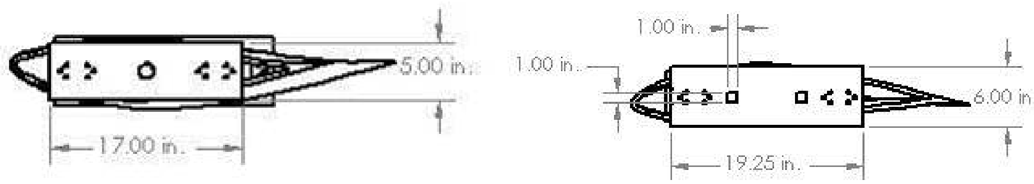

Figure 3.4. Schematic of the wind tunnel model top (left) and bottom (right) mounting plates.

Final assembly of the model in the Pennsylvania State University low-speed, low-turbulence wind tunnel is shown in Fig. 3.5. To further minimize 3-D effects on the flow over the model, custom wooden fillers are inserted between the model and the test section walls at the leading and trailing edges. Tape is applied around the top and bottom of the model to seal any remaining gaps to eliminate spanwise flow. A pre-existing leading-edge protection device applied by the manufacturer is removed from the model, and the leading edge is wet-sanded for an aerodynamically smooth finish.

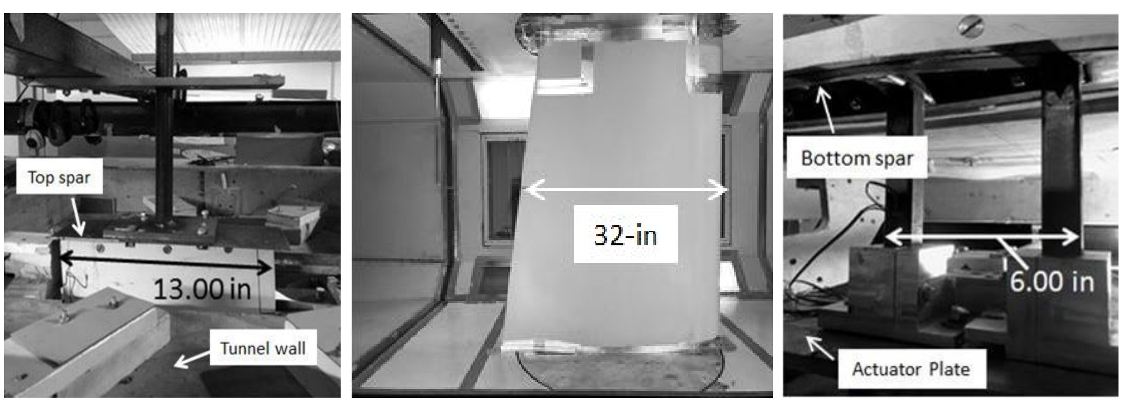

Figure 3.5. Complete assembly of the full-scale chord model in the PSU low-speed, low-turbulence wind tunnel.

3.1.4 Testing Procedure

Performance of the tapered LEP tapes is verified by the effect of the tape on sectional profile drag coefficient and transition location compared to the clean model. Tests are run at a chord Reynolds number of 3×10^6 to match the Reynolds number used for numerical simulations. Data for drag coefficient and transition location are only taken at $\alpha = 0°$ to avoid the effect of tunnel blockage on the data. According to the method of Pope and Harper [39], the blockage correction parameter, ε_t, is proportional to the ratio of the model frontal area and the test section area. For the 39.0-in full-scale chord model of an 18% thick airfoil, tunnel blockage correction parameter is approximately $\varepsilon_t = 0.024$ at $\alpha = 0°$.

For such a large model in a 39.9-in x 58.1-in test section, the tunnel walls limit the natural displacement of the flow around the model for any angle of attack beyond $\alpha = 0°$. Distortion of the flow over the upper and lower surface of the body at high angles of attack by the tunnel walls primarily effects the wake behind the body [40]. Since drag coefficient of the model is measured from the wake profile, any change in the wake profile impacts the data and hinders accurate verification of the numerical estimates at higher angles of attack.

Estimates for Δc_d are consistent across the small angle-of-attack range simulated in CFD (Fig. 2.32 & Fig. 2.33). At $\alpha = 0°$, both tapered LEP tapes (350-2-0.5 and 500-2-G) show negligible performance difference with respect to change in drag coefficient relative to the clean baseline. The comparable performance is maintained and independent of angle of attack for tapered LEP tapes. Thus, data at $\alpha = 0°$ are representative of the performance at the other angles of attack of interest in this study. Standard tapes also perform consistently across the range of angles of attack considered in the numerical study. A higher increase in drag coefficient compared to the clean airfoil is almost always observed for 500-6-0 compared to 350-6-0. The drag increase compared to the clean baseline is 30%, which is maintained between the two standard LEP tapes at low angles of attack

The two (2) down-selected tapered LEP tapes simulated in CFD with transition modeling and two (2) standard LEP tapes are individually applied to the clean model with a wet application technique. This allows for easy maneuvering in the early stages of application to guarantee correct alignment. The center of each tape is measured and marked along the length of the section to be applied to the model for consistent alignment with the approximate center of the leading edge. Each tape applied is 6-in wide and covers approximately 2-in of the upper and lower surface of the model (Fig. 3.6).

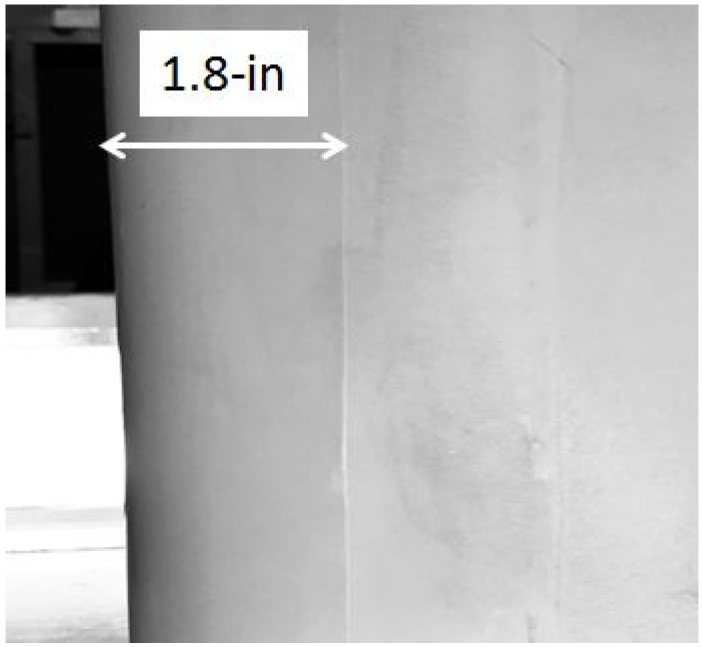

Figure 3.6. Standard 3M LEP tape applied to the wind tunnel model.

Using the wake probe, profile drag coefficient of the model is computed from the total and static pressures in the wake using the method of Pope [39]. The method compares the momentum in the flow ahead of and in the wake of the model. As the flow passes over the wind tunnel model, momentum is lost, and that momentum loss is directly proportional to the profile drag of the model via the velocity deficit [39]

$$D = \int\int \rho V(V_o - V)da \tag{3.1}$$

where V_o is the initial air speed, V is the air speed in the wake, and da is a small area of the wake perpendicular to the air flow. The drag force is transformed into the non-dimensional drag coefficient using

$$c_d = \frac{D}{\frac{1}{2}\rho V_o^2 S} \tag{3.2}$$

where S is a unit wetted area of the model. Using this transformation on Eq. 3.1,

c_d is estimated from momentum theory as

$$c_d = 2 \int \int \left(\frac{V}{V_o} \frac{da}{S} - \frac{V^2}{V_o^2} \frac{da}{S} \right) \tag{3.3}$$

Applying Bernoulli's equation, assuming the flow in the wind tunnel is irrotational, inviscid, incompressible, and allowed to come to steady-state, the velocities V and V_o can be directly estimated by the pressure difference in the free-stream and the wake. Using H_o and H as the total head in the free-stream and wake respectively, Bernoulli can be written as

$$H_o - p_o = \frac{1}{2} \rho V_o^2 \tag{3.4}$$

$$H - p = \frac{1}{2} \rho V^2 \tag{3.5}$$

Combining the relations Bernoulli relations and Eq. 3.3, the following relation can be used to directly estimate the profile drag coefficient of the wind tunnel model

$$C_d = 2 \int \left(\sqrt{\frac{H - p}{H_o - p_o}} - \frac{H - p}{H_o - p_o} \right) \frac{dy}{c} \tag{3.6}$$

The quantity (H - p) is measured directly with the wake probe at incremental locations as it traverses the wake. The integral above can then be evaluated as a simple summation of the incremental values at each point in the wake. Standard low-speed wind tunnel boundary corrections [41] are applied to the data. Wake-survey probe total-pressure-tube displacement correction is also applied [42].

Transition location of the boundary layer is observed with an oil visualization method. Aeroshell™W 80 Aviation Oil, which is luminescent under black light exposure, is applied to the upper surface of the model. The flow over the model is allowed to come to equilibrium at a given free-stream Reynolds number until the oil pattern is unchanging, and boundary-layer behavior can be assessed. The oil is thinned to reduce self-influencing effects, allowing the oil to flow freely with the stream-wise flow over the blade.

3.1.5 Results

Baseline data for the clean model are measured for computation of the change in profile drag from application of LEP tape to a wind turbine blade (Fig. 3.7). Consistency of the data-acquisition method and wind tunnel calibration is also assessed with the clean data. Two data points are taken at three Reynolds numbers: $1x10^6$, $2x10^6$, and $3x10^6$. Measured profile drag with the wake probe differs by no more than +/- 0.05%, and Reynolds number variations on the order of +/- 1.5% between each measurement. Data acquired for profile drag using wake probe measurements are consistent, and the clean data presented below can be used as a comparison for the change in profile drag when LEP tape is applied to the leading edge of a wind turbine blade.

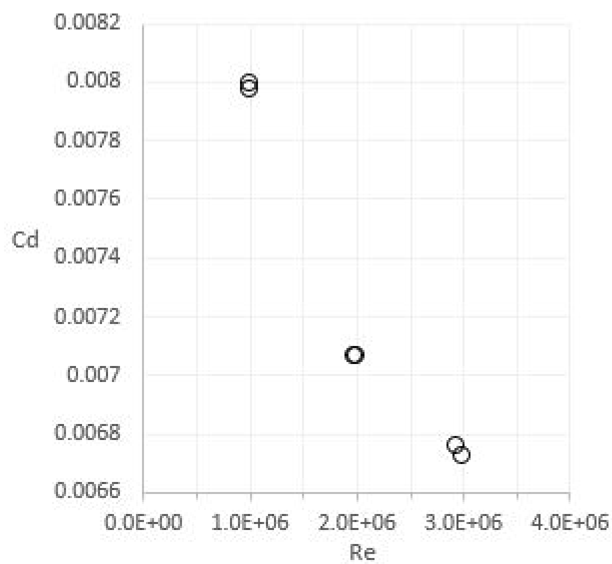

Figure 3.7. Measured profile drag of the clean model as a function of Reynolds number.

Drag data are acquired for three LEP tape applications: 350-6-0, 500-6-0, and a prototype 500-2-G tape developed by 3M. The 350-6-0 is based on the 3M^{TM}Wind Blade Protection Tape W8607, the standard LEP Tape on the market today [43]. The 500-6-0 is created by layering standard tapes together to achieve an approximate backward-facing step height of 500 μm. Percent Δcd relative to the clean data is calculated at three Reynolds numbers. Data are only acquired for 500-6-0 at Re = $3x10^6$ because of time constraints on testing and to verify the numerical data generated at the same Reynolds number.

At low Reynolds numbers, the presence of the backward-facing step of LEP tapes does not impact the boundary-layer of the model. Profile drag increases are at most 5% (for 350-6-0) at Reynolds numbers below 3x10^6, which is within the tolerance of the consistency study for the clean data (Fig. 3.8). At these Reynolds numbers, backward-facing steps of at most 350 μm are below the critical height required for premature boundary-layer transition.

At Re = 3x10^6, all three tapes appear to induce early-onset transition of the boundary-layer, noted by the dramatic increase in profile drag compared to the clean model (Fig. 3.8). Magnitude of drag increase relative to a clean model is also a function of step height. As the height of the backward-facing step increases, profile drag increases. The smallest step height of 75 μm increases drag by 30%, a step height of 350 μm results in a 60% increase, and a 500 μm step height increases drag 85% compared to the clean model. Though tapering the backward-facing step to a significantly smaller height still increases drag by 30% relative to a clean baseline, that is nearly half the drag increase for a standard LEP tape, indicating there is some benefit to a tapered LEP tape cross-section.

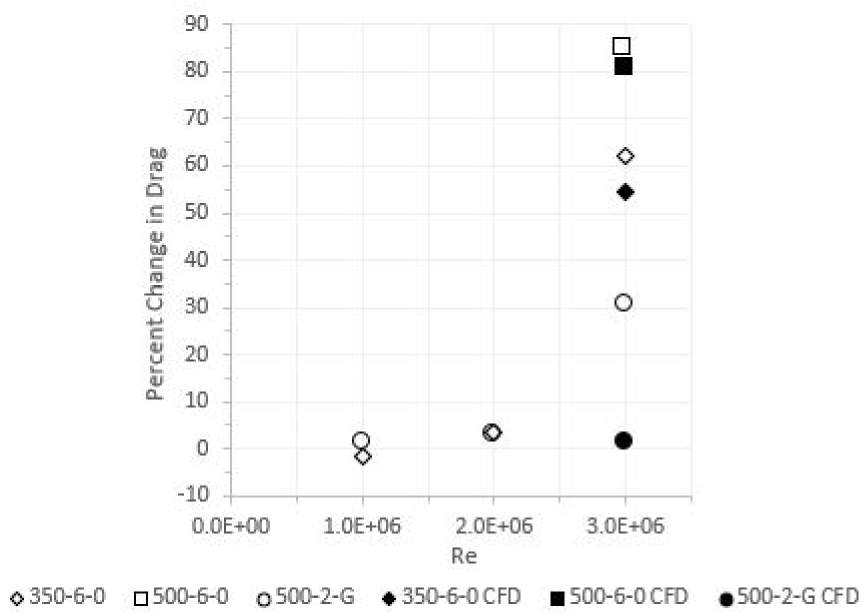

Figure 3.8. Percent change in Cd relative to the clean model as a function of Reynolds number.

Data generated using CFD methods for each tape configuration at Re = 3x10^6 are also included to verify the accuracy of the CFD models. For standard, un-tapered LEP tapes, experimental data sufficiently verify the quality of the CFD estimates at $\alpha = 0°$. Tapered LEP tapes are not predicted to trip the boundary layer, which results in negligible drag increase at this angle of attack using numerical methods. Experiments indicate, however, that a significantly higher increase in profile drag occurs for a tape with a 75 μm backward-facing step height. This indicates that the transition model used for the CFD analysis might not accurately predict the transition phenomenon for a backward-facing step below a certain height.

Details of the transition phenomenon for each tape are observed using oil visualization of the flow over the model. Oil visualization is also used to verify the two-dimensionality of the flow over the model, confirming that a comparison can be made between the experimental data and the 2-D CFD data. Flow over the clean model is visualized in Fig. 3.9a. Natural transition of the boundary layer from laminar to turbulent occurs around mid-chord, about 14.25-in from the leading edge. The transition point along the span of the model is roughly straight, indicating that the two-dimensional approximation is valid for these experiments.

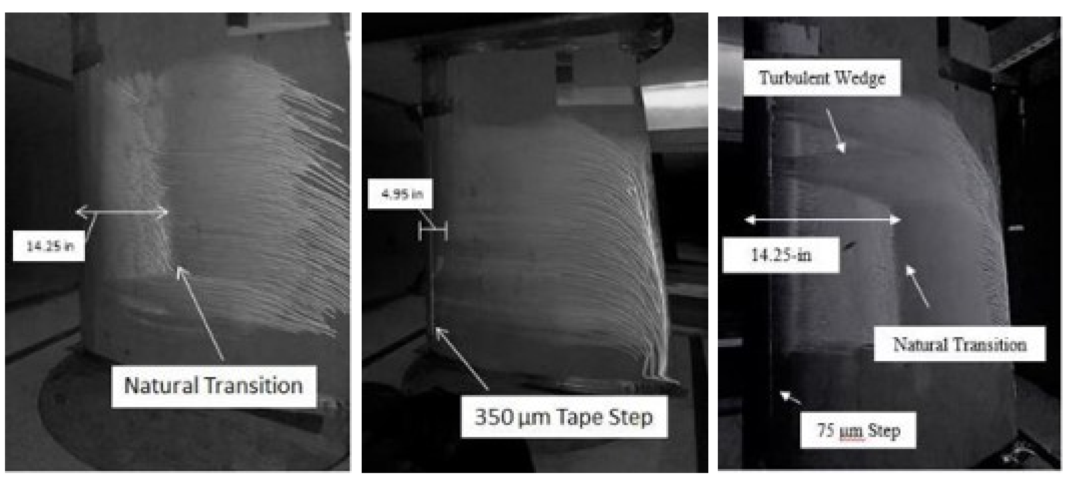

Figure 3.9. Oil visualization of transition location on the upper surface at $\alpha = 0°$ and Re = 3x10^6 for a) clean, b) 350-6-0, and c) 500-2-G.

Transition of the boundary layer for the standard LEP tape with a step height of 350 μm occurs at the backward-facing step (Fig. 3.9b). A small separation bubble occurs just behind the step, ending 4.25-in from the leading edge, where the boundary layer separates and then reattaches as a turbulent boundary layer. By the time the air flow reaches the trailing edge, gravitational effects now dominate the flow of the oil over the surface, as the model is mounted vertically in the test section. The premature transition of the boundary layer caused by the large backward-facing step reduces the momentum available in the boundary layer. When the flow reaches the trailing edge, there is little momentum left to keep the boundary layer attached, indicating that the premature transition also induces early separation of the boundary layer from the blade surface.

Contrary to the 30% drag increase for the 500-2-G tape, oil visualization reveals that the boundary layer remains attached in some locations (Fig. 3.9c). Natural transition, at the same stream-wise location as the clean model, is observed downstream of the lower half of the tape. At those locations, laminar separation of the flow is observed downstream of the tape step, followed by a 2-in separation bubble, then the flow reattaches as a laminar boundary layer just downstream of the bubble. Turbulent wedges forming at the tape step are observed at other locations, eliminating the natural transition observed in other areas. These wedges form directly in the plane of the wake probe, explaining the significant increase in drag observed for the LEP tape with a 75 μm backward-facing step height. Without the presence of turbulent wedges, natural transition will occur along the span of the model, and little to no change in profile drag compared to the clean model should occur, validating the CFD result for tapered LEP tapes plotted in Fig. 3.8.

When observed with a magnifying glass, small defects in the tape and patches of debris downstream of the tape are observed where turbulent wedges form. For these tests, the prototype tape is applied with spray-on adhesive, which leaves a residue on the surface of the model downstream of the edge of the tape. Debris trapped by the residue that is not removed, if large enough, can cause premature boundary-layer transition, eliminating the benefit of a tapered backward-facing step. Without the presence of the debris and defects, though, oil visualization of the flow over the upper surface confirms the CFD prediction that premature boundary-layer transition does not occur for a 75 μm backward-facing step height at Re = 3x10^6. If applied cleanly and correctly, tapered LEP tapes demonstrate the potential to eliminate the lift and drag penalty documented for standard LEP tapes.

3.2 Critical Roughness Height Model

Using the experimental results obtained for three LEP tapes of various backward-facing step heights, an analytical model is developed to size the height of the backward-facing step found on LEP tapes to prevent premature boundary-layer transition. Knox and Braslow [30] developed a simple method to estimate the critical height of a roughness element, at a chord-wise location x along the surface, needed to induce early-onset transition. The method reduces to a single equation that relates the characteristics of the flow at the height of the roughness element, k, to a critical Reynolds number:

$$\frac{Re_k}{\sqrt{Re_x}} = 2\eta_k \left(\frac{u_k}{u_x}\right)\left(\frac{\mu_o \rho_k}{\rho_o \mu_k}\right) \tag{3.7}$$

The local Reynolds number, Re_x, is a function of chord-wise location along the span, x, and the edge velocity at that location, u_e, and is computed as

$$Re_x = \frac{\rho u_x x}{\mu}. \tag{3.8}$$

The parameters u_k, μ_k, and ρ_k in Eq. 3.7 are the velocity, absolute viscosity, and density at the height of the roughness element inside the boundary layer. At low Mach numbers, dynamic viscosity is assumed to be constant inside and outside of the boundary layer. The velocity at the top of the tape step, u_k, is estimated using the Blasius solution for the boundary layer velocity profile over a flat plate (Fig. 3.10). The Blasius solution is just one method for determining the local laminar boundary-layer velocity profile, and it is a simple method because it is a known solution. An exact estimate for the laminar boundary-layer velocity profile at the tape step for the NACA 64-618 airfoil can be determined with other integral boundary layer methods, but at a high computational cost. For the purpose of this work, the Blasius solution is a sufficient and conservative approximation.

In the Blasius approximation, the velocity inside the boundary layer at the height of a roughness element is a function of the non-dimensional height above the surface of the body, η, which is given by

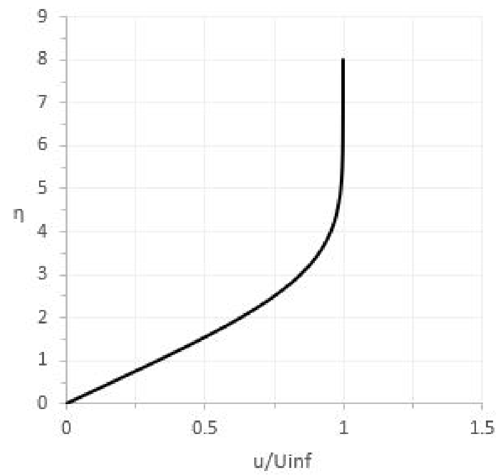

Figure 3.10. Blasius solution for the boundary-layer velocity profile over a flat plate [9].

$$\eta = \frac{y}{\delta} \tag{3.9}$$

where δ is the boundary-layer thickness, and y is approximated by the height of the LEP tape backward-facing step.

With the Knox and Braslow method and the wind tunnel results, the critical Reynolds number at the height of the tape step, $\mathrm{Re}_{k,crit}$, for a 2-D backward-facing step is determined. Once the critical transition criterion is determined, the Re_k for a 75 μm backward-facing step for a given free-stream Reynolds number and local angle of attack is compared to the critical value, $\mathrm{Re}_{k,crit}$. If Re_k for a given backward-facing step height is below the critical value, then premature boundary-layer transition at the backward-facing step for an LEP tape will not occur.

In Fig. 1.16 from von Doenhoff and Horton [10], for a 2-D trip with a forward-facing step, $\mathrm{Re}_{k,crit} = 600$ is the standard approximation. The adverse pressure gradient over a backward-facing step, however, makes the boundary layer more susceptible to premature transition. For a backward-facing step, then, the critical Reynolds number at the top of the step height is lower than 600 for a standard trip. Oil visualization for the standard 3M LEP tape with a 350 μm backward-facing step confirmed that the boundary layer transitions at the tape step at Re = 3x10^6. Transition was not observed, based on delta drag data, at Re = 2x10^6 for the same LEP tape. Computing Re_k at the top of the backward-facing step for both free-stream Reynolds numbers, at $\alpha = 0°$, identifies a range for $\mathrm{Re}_{k,crit}$ for a backward-facing step.

For a 6-in wide LEP tape, the backward-facing step is located at x/c = 0.06. Local edge velocity, u_e, and the local boundary-layer thickness, δ, at x/c = 0.06 are determined from XFoil boundary layer data for the NACA 64-618 airfoil at $\alpha = 0°$ and at Re = $2\text{x}10^6$ and $3\text{x}10^6$. With δ, the non-dimensional height of the tape step, η, in the boundary layer is computed with Eq. 3.9, where y is the height of tape step. The velocity at the top of the backward-facing tape step is found using η and the Blasius solution for the boundary-layer velocity profile. The Reynolds number at the height of the tape step, Re_k, is then computed using

$$Re_k = \frac{\rho_k u_k k}{\mu_k} \tag{3.10}$$

The value of Re_k is computed with this method for a range of backward-facing step heights, from k = 0 μm to 350 μm. To isolate the critical Reynolds number at the top of the tape step required for premature boundary-layer transition, Re_k is plotted as a function of tape step height, k, at different free-stream Reynolds numbers (Fig. 3.11). An additional Reynolds number, Re = $5.5\text{x}10^6$, is included as the maximum Reynolds number that occurs along the span of an utility-scale wind turbine blade at the highest free-stream wind speed. Since the likelihood for premature transition due to a roughness element increases with Reynolds number, this represents a worst-case-scenario check for a tape design to verify that a given design will not trip the flow through the full range of Reynolds numbers experienced by a wind turbine.

For a step height of k = 350 μm, premature boundary-layer transition on the full-scale chord model occurred for a free-stream Reynolds number between Re = $2\text{x}10^6$ and $3\text{x}10^6$ during wind tunnel experiments. The roughness height Reynolds number, according to Knox and Braslow, for that step height at those Reynolds numbers is Re_k = 150 and 275, respectively (Fig. 3.11). In that range exists a critical value, $\mathrm{Re}_{k,crit}$, where a small increase in Re_k above that value results in a fully-transitioned boundary layer downstream of the roughness element [30]. Conservatively, $\mathrm{Re}_{k,crit}$ = 200 is identified as the critical roughness Reynolds number above which a 2-D backward-facing step will initiate premature boundary-

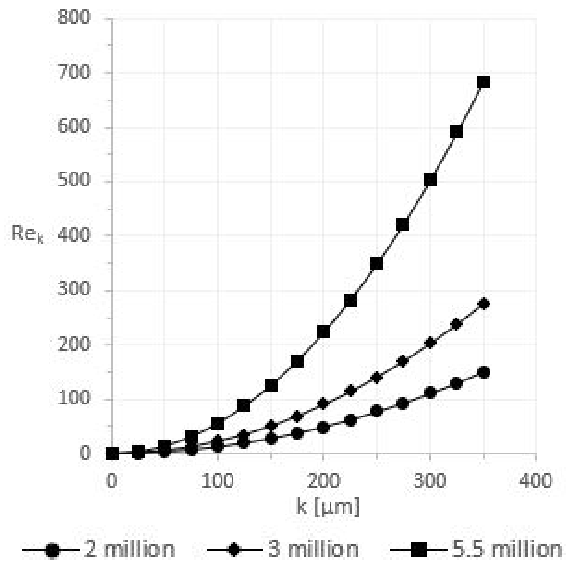

Figure 3.11. Roughness Reynolds number as a function of roughness height for a 6-in wide LEP tape.

layer transition.

After determining $Re_{k,crit}$, the size of the backward-facing step for a 6-in wide LEP tape can be sized to ensure the boundary layer does not transition at the edge of the tape. For a 75 μm backward-facing step height, the approximate height of step on the prototype 500-2-G LEP tape, $Re_k = 12$, at Re = 3x10^6 in the free-stream (Fig. 3.11). This is well below the critical value, verifying that the prototype 500-2-G LEP tape will not prematurely transition the boundary layer because of the presence of a backward-facing step. A backward-facing step of this height is also insufficient to cause premature boundary-layer transition at the highest Reynolds number along the span of a small utility-scale wind turbine blade, with $Re_k = 30$ at a free-stream Reynolds number of 5.5x10^6.

To increase erosion protection capability and reduce the risk of premature boundary-layer transition, increasing the chord-wise extent of the LEP tape is beneficial [18, 19]. The same procedure is repeated for a new tape extent of x/c = 0.102 for 10-inch-wide LEP tapes (Fig. 3.12).

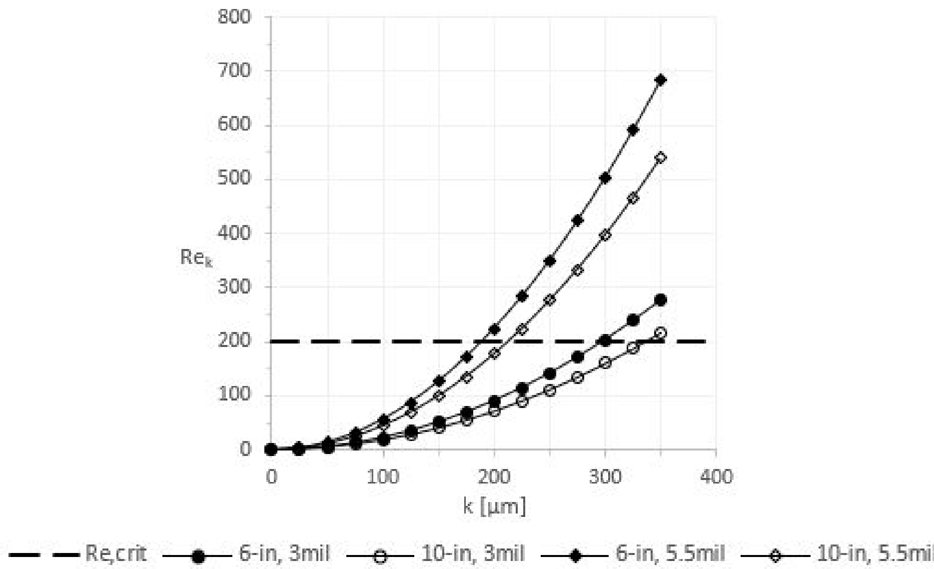

Figure 3.12. Comparison of Re$_k$ as a function of roughness height, k, for 5-in and 10-in wide LEP tapes.

The benefit of widening the LEP tape increases as the height of the backward-facing step of an LEP tapes increases. The roughness Reynolds number for a 350 μm step is well above the critical value for a 6-in tape, but is only slightly higher than the critical value when the location of the step is moved further downstream in the chord-wise direction. When free-stream Reynolds number increases to 5.5x10^6, the benefit of increasing the tape width is insufficient to eliminate premature boundary-layer transition for a LEP tape with a 350 μm backward-facing step.

A 75 μm backward-facing step height remains insufficient to cause premature boundary-layer transition at all free-stream Reynolds numbers considered. By increasing the width of a tapered LEP tape, the width of the protective region of maximum thickness, W$_{thick}$, increases while the height of the backward-facing step remains below the critical value required for premature transition. This increases the overall erosion protection capability of the LEP tape, while maintaining the requirement that the backward-facing step not prematurely transitions the boundary layer.

The method of Knox and Braslow, along with experimental data for a standard LEP tape configuration, identifies a critical roughness Reynolds number of Re$_{k,crit}$

= 200 for backward-facing steps found on LEP tapes, see Fig. 3.12. From calculations of the roughness Reynolds number using boundary-layer flow properties, results from the Knox and Braslow method correlate to experimental observations. The analytical method developed predicts that the novel tapered LEP tape shapes investigated in this work will not transition the flow. Eliminating the premature boundary-layer transition minimizes the lift and drag penalties on the airfoil, verifying the results obtained in CFD numerical simulations.

Increasing the width of a novel tapered LEP tape does not impact the premature transition condition, but erosion protection capability is increased. Experimental observations of the flow over the model surface using oil visualization indicate that the aerodynamics of a wind turbine rotor blade is sensitive to the quality of the manufacturing and tape application. In the presence of debris accrued when adhesive is applied and defects in the tape surface, benefits of tapering are eliminated. For a tapered LEP tape that transitions at the tape step when debris or defects are present, however, the profile drag increase is nearly half that measured for a standard LEP tape. This verifies that tapering the cross-sectional profile provides significant aerodynamic benefits, even with the presence of application and manufacturing defects.

Chapter 4

Impact on Annual Energy Production of a Wind Turbine

The final objective of this work is to estimate the impact of tapering LEP tapes on wind turbine Annual Energy Production (AEP). Standard LEP tapes have been shown to cause a 0.3% to 1.8% reduction in wind turbine AEP due to the degradation in airfoil lift and drag caused by premature boundary-layer separation at the backward-facing step [17, 18]. Tapered LEP tapes, by comparison, already demonstrate significant aerodynamic improvements by eliminating premature boundary-layer transition for a backward-facing step height that is less than the critical roughness height required for transition. By tapering LEP tapes, it is possible that a loss in AEP due to the application of LEP tape can be eliminated. To investigate this hypothesis, the wind turbine design and analysis code XTurb-PSU [44] is used to calculate the power output of a 1.5 MW wind turbine. A Weibull distribution is applied to the representative power curves and AEP is calculated from the resulting distribution.

4.1 Wind Turbine Definition

The representative wind turbine used for AEP estimation is the PSU 1.5 MW wind turbine. It is designed to have optimal airfoil, twist, and chord distributions. The original wind turbine is composed of the Delft University family of optimal wind turbine airfoils (Fig. 4.1). PSU-Tape is based on the PSU 1.5 MW design, but includes the NACA 64-618 as the tip section (span location F & G) airfoil.

Blade Span Location	A	B	C	D	E	F	G
PSU 1.5 MW	Cylinders	00-W2-401	00-W2-350	97-W-300	91-W2-250	93-W-210	95-W-180
PSU-Tape	Cylinders	00-W2-401	00-W2-350	97-W-300	91-W2-250	NACA 64-618	

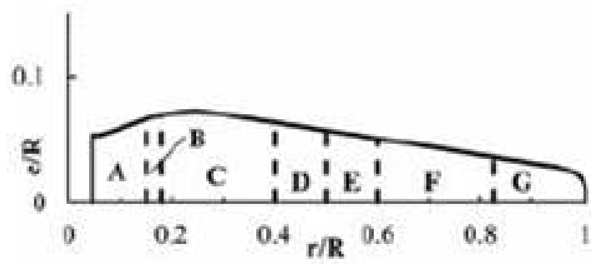

Figure 4.1. Wind turbine airfoil definition at each spanwise location [21].

For the following analysis, the effect of LEP tape application is only modeled at the outboard 40% of the wind turbine blade. Typically, LEP tapes are applied at the outboard 33% of the rotor blade where it is most susceptible to erosion and produces more than half of the rotor torque. The spanwise torque distribution for the original PSU 1.5 MW wind turbine at an incoming air speed of 8 m/s is given in Fig. 4.2. The kink in the torque distribution at r/R = 0.825 corresponds to the location where the blade transitions from the DU 93-W-210 to the DU 95-W-180.

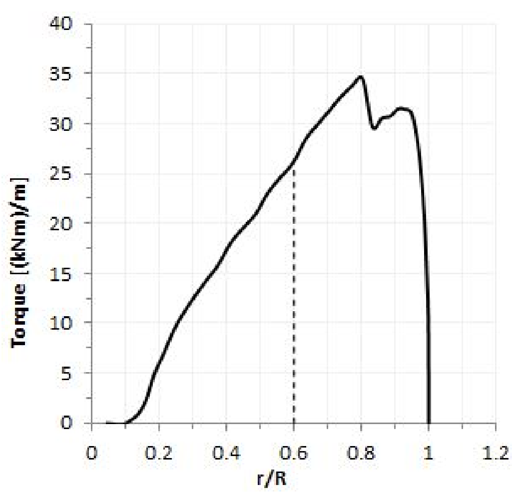

Figure 4.2. spanwise torque distribution for the PSU 1.5 MW wind turbine.

Beyond r/R = 0.6, peak torque is achieved around 80% span and the torque generated by this section of the blade is more than 50% of the total torque. In the classical Blade Element Momentum (BEM) theory, wind turbine power is computed by integrating the product of the rotor rpm and the spanwise elemental torque, dQ, over the blade from root to tip via

$$P = \int_{r_h}^{R} \Omega dQ. \tag{4.1}$$

For a rotor with B blades, the torque for a given blade element segment at a distance r from the root (with local blade flow angle ϕ and velocity, V_{rel}, and chord length, c) is given by

$$dQ = B\frac{1}{2}\rho V_{rel}^2 (C_l sin\phi - C_d cos\phi) crdr \tag{4.2}$$

Elemental torque is strongly dependent on the local lift and drag properties of that segment. Any increase in drag or reduction in lift for a blade segment reduces the elemental torque produced at that location, which impacts rotor power production. With the application of LEP tape to an airfoil, the lift loss and drag increase both work against rotor torque and power production. Those effects will be most detrimental at the highest torque producing segments, which are those beyond 60% span where the definition of the new PSU-Tape wind turbine begins.

Even with the new tip-section definition, the operating conditions of PSU-Tape remain relatively unchanged from those of the PSU 1.5 MW wind turbine. Technical specifications, adapted from the operating conditions of the PSU 1.5 MW, of the new PSU-Tape wind turbine are outlined in Table 4.1.

Number of Blades	3
Rotor Diameter	77 m
Rated Power	1.5 MW
Cut-in V_o	2 m/s
Cut-out V_o	25 m/s
Tip Speed Ratio	2.2 - 13.9
Power Control	Rotor speed and blade pitch

Table 4.1. Technical summary of the PSU-Tape wind turbine [21].

4.2 Power Estimates

To estimate the effect of LEP tape on power output and AEP degradation for a 1.5 MW scale wind turbine, an in-house wind turbine design and analysis code, XTurb-PSU [44], is used. XTurb-PSU computes wind turbine power, torque, and thrust via the Blade Element Momentum (BEM) theory equations with a structure based on NRELs AeroDyn [45] code, and also includes a solution-based stall delay model [46]. Power estimates below for each variation of the PSU-Tape wind turbine are based on the 2-D aerodynamic coefficients computed in CFD with the transition model implemented.

4.2.1 Clean Baseline

Wind turbine AEP analysis for a rotor equipped with LEP tape is quantified by the change in AEP relative to a clean rotor with un-taped blades. By changing out the tip-section airfoil with the NACA 64-618 to create the new PSU-Tape wind turbine, a new baseline clean power curve is established for later comparison. The PSU-Tape wind turbine uses the same elemental discretization of c/R and r/R as the PSU 1.5 MW configuration.

To generate power curves for PSU-Tape, c_l, c_d, and c_m data generated in CFD, with transition modeling applied, for α = -2° to 8° are used as an input for the data at the tip of the rotor blade, beginning at 80% span. The narrow range of the polar data are expanded to cover α = -180° to 180° by turning on the VITERNA correction option.

Using XTurb-PSU's design feature, pitch and twist of the PSU-Tape wind turbine can be adjusted to control the rated power output to 1.5 MW. Pitch settings at the tip of the blade, where the new airfoil is used that defines the unique PSU-Tape configuration, are adjusted until rated power of 1.5 MW is reached at the same nominal wind speed of 12 m/s as the original PSU 1.5 MW wind turbine. For each wind speed beyond 12 m/s, a range of twist settings near the original PSU 1.5 MW settings are used to find the optimal twist setting to achieve the power coefficient required for a power output of 1.5 MW for that wind speed. The new pitch- and twist-optimized clean PSU-Tape power distribution is compared to the PSU 1.5 MW distribution in Fig. 4.3.

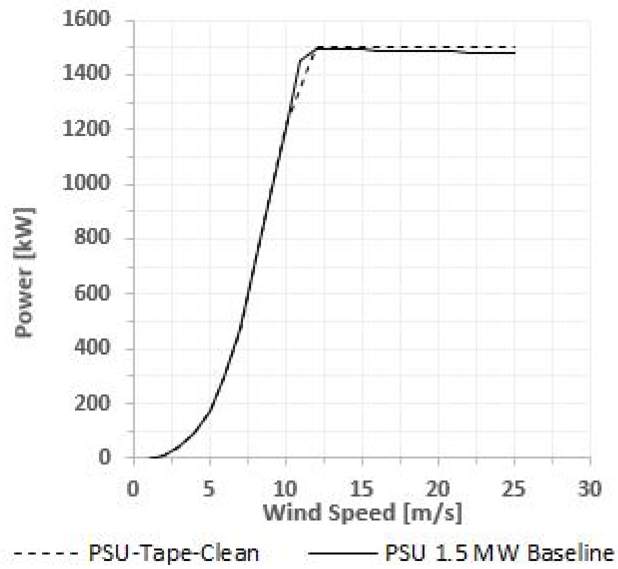

Figure 4.3. Power curves for PSU 1.5 MW and the new PSU-Tape-Clean wind turbine.

Some power loss compared to the original PSU 1.5 MW wind turbine configuration is observed near the rated power wind speed. Though the rotor is still chord, twist, and pitch optimal, the airfoils are no longer optimal with the change in tip-section airfoil to the NACA 64-618. The slightly lower aerodynamic performance of the NACA 64-618 with the PSU-Tape pitch and twist settings compared to the performance of the original PSU 1.5 MW airfoil distribution results in the slight differences observed. Despite the slight discrepancy observed near the rated wind speed, the PSU-Tape rotor configuration is representative of a utility-scale 1.5 MW wind turbine, and the PSU-Tape power curve can be used as the baseline for AEP comparison.

4.2.2 Eroded Blades

To get another visual comparison for the significantly improved performance of the tapered LEP tapes on wind turbine power production, wind turbine power is also estimated for an eroded blade. A two-dimensional erosion model, based on the works of [8, 16, 17], is applied to the leading edge of the NACA 64-618 airfoil. The final distribution includes 1-inch of leading-edge delamination, of 2.5 mm depth, with pits also of 2.5 mm depth left and right of the delaminated region that follow an approximately Gaussian distribution (Fig. 4.4). Additional material is removed between the pits to model the gouging of the airfoil surface that modifies the shape of the leading edge in field observations of wind turbine leading-edge erosion. The leading-edge erosion covers x/c = 0.056, to compare the power output of a taped blade to a blade with erosion where the protective tape would be.

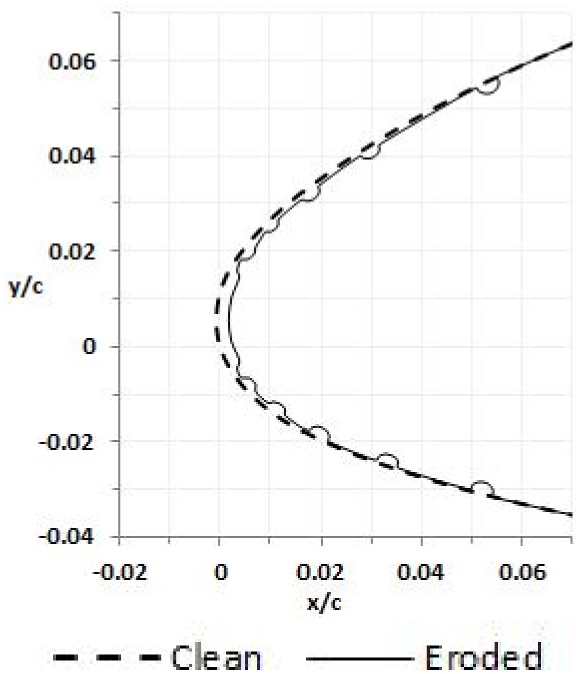

Figure 4.4. Power curves for a wind turbine blade with leading-edge erosion compared to a clean blade

Techniques developed to mesh an airfoil with LEP tape applied are used to mesh the eroded airfoil (Fig. 4.5). The forward-facing step of the delaminated leading edge is meshed as if it were the backward-facing step of an LEP tape with multiple cells over the step to sufficiently resolve the flow in that region. Pits are meshed according to the meshing technique from Wang et al. [16]. Their selected pit grid, after the appropriate sensitivity study for different meshing techniques was conducted, included an unstructured quadrilateral mesh with 15 nodes around the semicircle pit cavity. The regular structured mesh of the clean airfoil begins immediately above the pit opening, with only some refinement in the width of the cells over the width of the pit. Irregularity in the densest portions of the final structured grid around the leading edge are a result of maintaining perpendicular grid lines to the airfoil surface for each pit refinement.

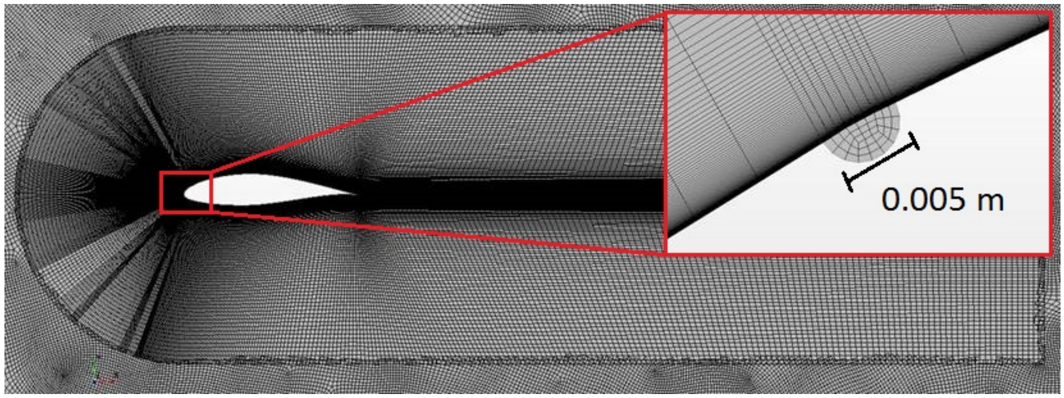

Figure 4.5. Power curves for a wind turbine blade with leading-edge erosion compared to a clean blade

A polar from α = -2° to 8° is generated for the eroded NACA 64-618 airfoil. The generated data for c_l, c_d, and c_l/c_d at Re = 3x10^6 are compared to the clean NACA 64-618 airfoil to quantify the performance degradation due to leading-edge erosion (Table 4.2). Compared to the relative performance of any of the LEP tapes, erosion severely degrades 2-D airfoil aerodynamics.

α	%Δ c_l	%Δ c_d	%Δ c_l/c_d
-2	-5.229	88.360	-49.686
0	-4.579	89.626	-49.679
2	-4.649	97.360	-51.687
4	-5.764	132.316	-59.437
6	-7.799	121.485	-58.372
8	-8.037	104.016	-54.924

Table 4.2. Change in lift coefficient, drag coefficient, and c_l/c_d of the NACA 64-618 airfoil due to an eroded leading edge.

Lift losses due to this particular leading-edge erosion model peak at 8%, more than twice the lift degradation of the 500-6-0 LEP tape at α = 8°. As angle of attack increases, loss in lift increases. The same trend is observed for drag, though a slight drop is observed when the airfoil exits the constant region of minimum drag around maximum c_l/c_d at $\alpha = 6°$. Just before the drag increases, due to separation of the flow at the trailing edge, peak drag increase from an eroded leading edge is nearly 135%.

Replacing the data for the clean NACA 64-618 baseline, polar data for c_l and c_d for the eroded airfoil are used for the tip-section airfoil data in the XTurb-PSU input file. The new rotor configuration is denoted PSU-Tape-Eroded, and the following power curve for an eroded blade is generated with un-adjusted pitch and twist settings (Fig. 4.6). Losses occur in both Region II and III due to an eroded wind turbine blade, including a noticeable drop in rated power at lower wind speeds in Region III.

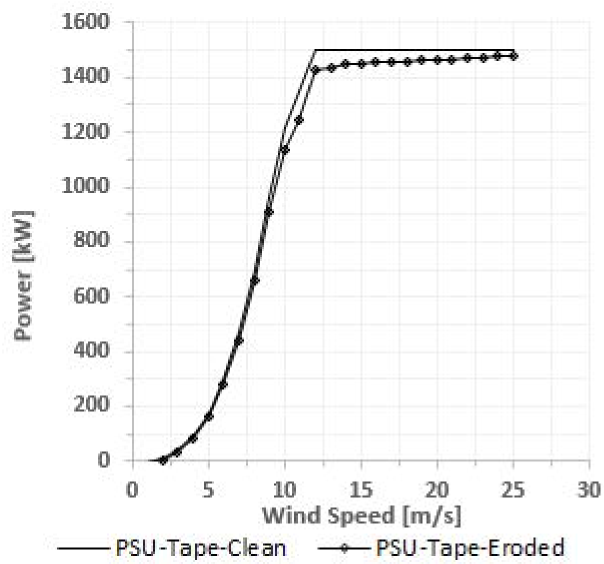

Figure 4.6. Power curves for a wind turbine blade with leading-edge erosion compared to a clean blade

Despite a nearly 135% increase in drag and 8% decrease in lift, relative power loss is small with a maximum power loss of 7% in Region II. In Region III, power loss is as high as 5% at rated power, which drops to only 1% at the cut-out wind speed. In this range, the local angle of attack of each blade element beyond 60% span is relatively small. The largest positive observed angle of attack for any element at all wind speeds near rated power is only 6°. Most blade stations operate in a small range near 0° in this region where some of the smallest losses occur for both lift and drag, resulting in the relatively small power losses observed for this rotor configuration.

4.2.3 Tape Performance

Power curves for the down-selected LEP tapes and their respective LEP tape baseline configurations are generated by supplying the c_l and c_d data generated in CFD as the airfoil data for the blade sections of PSU-Tape where the effect of the tape is to be considered. Similar to the PSU-Tape-Eroded curve, twist and pitch settings remained unchanged from the original PSU-Tape-Clean distribution.

By applying a standard LEP tape (350-6-0 or 500-6-0), power losses are reduced compared to an eroded blade (Fig. 4.7). Losses are still observed in Region II, but the drop in rated power in Region III is reduced due to the lower drag and lift penalty of a standard LEP tape on airfoil performance. As thickness of the standard LEP tape increases, higher power losses are observed due to the slightly larger lift loss and drag increases due to the larger backward-facing step.

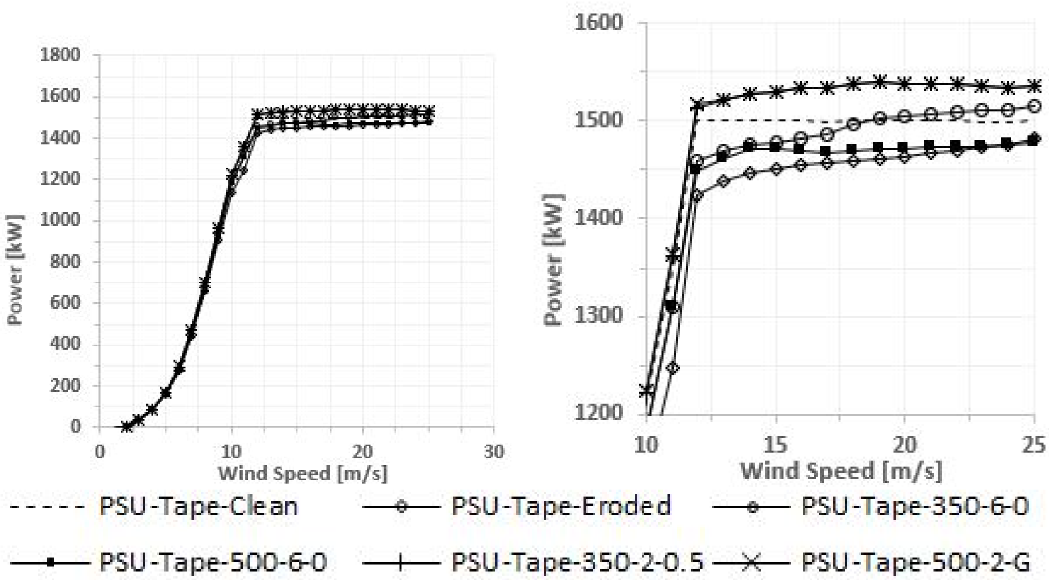

Figure 4.7. Effect of various LEP tape configurations on wind turbine power output.

By comparison, tapered LEP tapes demonstrate significant improvement in rotor performance. Tapering LEP tapes eliminates power losses in Region II observed for standard LEP tapes, and even result in a slight increase in power production for PSU-Tape in Region III. The increased rated power is a result of the increased lift compared to the clean airfoil observed for tapered tapes, which thicken the leading edge slightly and change the camber distribution. Though the rated power is above 1.5 MW in Region III, the pitch-controlled system of the PSU-Tape wind turbine will pitch out the blades at the outboard sections to bring the rotor back down to rated power to reduce the generator loads. The result is a power distribution identical to PSU-Tape-Clean. There is also negligible difference between the power curves for PSU-Tape-350-2-0.5 and PSU-Tape-500-2-G, indicating that the thickness has negligible effect on wind turbine power, but rather the size of the backward-facing tape step controls the impact of LEP tapes on wind turbine power output.

The final objective of this work is to estimate the effect of tapering LEP tapes on wind turbine Annual Energy Production (AEP). From the power curves in Fig. 4.7, AEP for each PSU-Tape rotor configuration is estimated by applying a Weibull curve to the power output. The Weibull curve is a probability distribution determined by the shape factor, k, and the scaling parameter, λ (Fig. 4.8). The Weibull curve estimates the probability of each wind speed occurring at the wind turbine site over the course of a day. The standard Weibull distribution for a wind turbine site is defined by a shape factor of k = 2, which reduces the Weibull distribution to a Rayleigh distribution. The scaling parameter is chosen as the average site wind speed, which is approximated as λ = 8 m/s for the following analysis.

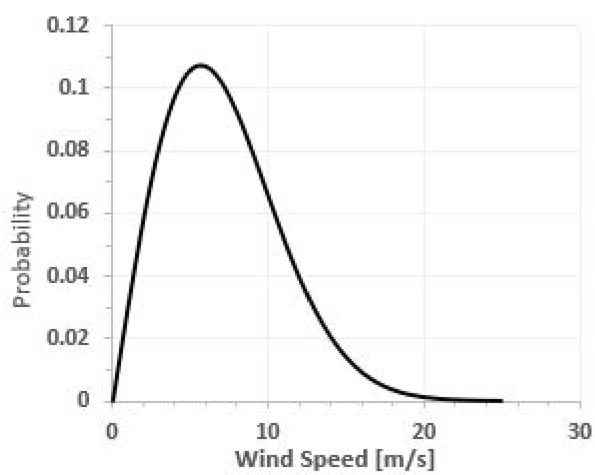

Figure 4.8. Weibull probability distribution of wind speeds for k = 2, λ = 8 m/s.

Wind turbine AEP at a given wind speed, V_o, is the power generated at each wind speed, Power(V_o), multiplied by the probability that wind speed occurs from the Weibull distribution, p(V_o), multiplied by the number of hours in a year, 5780 hours. Total AEP is the summation of all power produced at each possible site wind speed, V_o = 0 m/s to 25 m/s:

$$AEP = \left(\sum_{V_o=0}^{25} P(V_o) * p(V_o) \right) * 5780 \tag{4.3}$$

The computed AEP (in MWh) values for the eroded and taped blades is compared to the AEP generated by PSU-Tape-Clean to determine the change in AEP for different rotor configurations (Table 4.3).

Tape Configuration	Δ AEP (Clean) [MWh]	%Δ AEP (Clean)	Δ AEP (Baseline) [MWh]	%Δ AEP (Baseline)
Eroded	-279.969	-5.434%	-	-
350-6-0	-135.029	-2.621%	-	-
500-6-0	-155.564	-3.019%	-	-
350-2-0.5	38.101	0.740%	173.129	3.451%
500-2-G	46.904	0.910%	202.468	4.052%

Table 4.3. Effect of erosion and different tape configurations in wind turbine AEP.

Eroded wind turbine blades result in the largest loss in AEP for PSU-Tape at almost 5.5%. Applying a standard LEP tape to the leading edge of the rotor blades provides erosion protection and halves the percent AEP loss to 2.5% - 3%, depending on the LEP tape configuration. Percent AEP loss compared to PSU-Tape-Clean is nearly eliminated by careful design, with aerodynamic consideration of the cross-sectional profile of the LEP tapes and reducing the magnitude of the backward-facing step. With negligible difference in percent change in AEP for the 350-2-0.5 and 500-2-G tapered LEP tapes, thicker tapes can be produced to prolong LEP tape erosion protection lifetime at no aerodynamic cost to the wind turbine operator.

To investigate the effect of increased profile drag when LEP tapes are applied to rotors, AEP loss is plotted versus the average profile drag increase estimated in CFD over the angle of attack range α = -2 ° to 8° (Fig. 4.9). Profile drag increase compared to a clean blade is a function of backward-facing step height, as observed from CFD results and verified by wind tunnel experiments on a full-scale chord model. The lowest average increase is consistent with a 75 μm backward-facing step height. Profile drag increases on average 63% and 78% for a 350 μm and 500 μm backward-facing step height, respectively. The highest average increase is observed for an eroded 2-D airfoil profile at 106% compared to clean. For increasing values of average percent change in profile drag, AEP loss increases approximately linearly in this range.

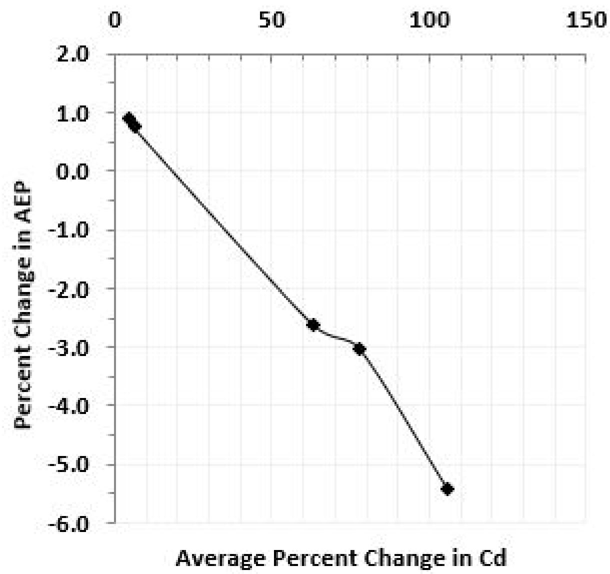

Figure 4.9. Percent change in AEP as a function of average percent change in Cd.

From experimentally measured data for a prototype LEP tape with a backward-facing step height of 75 μm, profile drag increases by 30% compared to clean at Re = $3x10^6$, half that of the increase measured for a standard LEP tape. The profile drag increase, however, was not from premature boundary-layer transition caused by the presence of the backward-facing step, but caused by debris just behind the tape and defects in the tape surface. Under these conditions, based on AEP loss versus average percent change in profile drag, AEP loss around 1% is expected, which is more than half the AEP loss of a standard LEP tape. Depending on the quality of the tape application to the rotor blades, predicted AEP loss for tapered LEP tapes is anywhere from 0% to 1%, a significant performance improvement over rotors equipped with the standard LEP tapes on the market today.

Chapter 5

Conclusion and Future Work

Partnering with 3M, an investigation of the impact of Leading-Edge Erosion Protection (LEP) tape on the Annual Energy Production (AEP) of a utility-scale wind turbine rotor was conducted. The goal of the study was to design a tapered cross-sectional profile that eliminates the aerodynamic degradation observed for a wind turbine rotor when a currently available LEP tape product is applied to the blades. To assess and verify the performance of the new LEP tape profiles, numerical, experimental, and analytical methods were developed.

Design parameters of interest were identified from published work on the aerodynamics of LEP tapes and leading-edge erosion. The maximum thickness, T_{thick}, and extent of the maximum thickness, W_{thick}, were selected for erosion protection capability. The height of the tape at the edge, T_{thin}, and the severity of the transition from T_{thick} to T_{thin} were also selected. From manufacturing limitations, T_{thin} was fixed at 75 μm. Three values of maximum thickness were selected, i.e. 200 μm, 350 μm, and 500 μm, where 350 μm is the thickness of standard LEP tapes on the market today. Extent of the maximum thickness was chosen to be either 1- or 2-in, where all tapes were a total of 6-in wide. The transition from maximum to minimum thickness of 5°, 0.5°, and a gradual taper were chosen for analysis. Combined, there were a total of seventeen (17) tapered LEP tape design variations considered in this study.

Computational Fluid Dynamics (CFD) models were developed to predict the impact of the different LEP tape configurations on the aerodynamics of the NACA 64-618 airfoil. Lift, drag, and lift-over-drag ratio for each configuration was compared to the clean airfoil and the performance of a standard, un-tapered LEP tape. Results show that variation in T_{thick}, W_{thick}, and θ_{taper} do not significantly impact aerodynamic performance. The largest change in lift, drag, and c_l/c_d compared to the clean airfoil is controlled by the height of the backward-facing step.

For backward-facing steps above a certain height, CFD predicts that the boundary layer separates laminar at the tape step, reattaches turbulent, causing premature transition of the boundary layer. Premature transition decreases lift, increases drag, and overall decreases c_l/c_d compared to a clean airfoil. For standard LEP tapes with backward-facing step heights of 350 μm and 500 μm, this premature transition behavior is observed. Drag increases compared to the clean airfoil anywhere from 40% to 115%, lift decreases 1% to 5%, and c_l/c_d decreases 25% to 55% for standard LEP tapes. When the cross-sectional profile of a LEP tape is tapered, drag increases 1% to 15%, and c_l/c_d decreases 5% to 10% overall. Tapered LEP tapes do not prematurely trip the boundary layer, resulting in the significantly improved 2-D aerodynamic performance compared to standard LEP tapes on the market today.

The behavior of the tapered LEP tapes predicted using CFD methods was verified with wind tunnel experiments. Experiments were conducted on a full-scale chord model of a utility-scale wind turbine blade. Profile drag of the model was measured at $\alpha = 0°$ and at free-stream Reynolds numbers of $1x10^6$, $2x10^6$, and $3x10^6$ using a wake probe. Below Re = $2x10^6$, profile drag compared to the clean model does not change significantly for both standard and tapered LEP tapes. Standard tapes of 350 μm and 500 μm thickness trip the boundary layer at Re = $3x10^6$, and profile drag increases 50% and 80% respectively compared to the clean model. For the tapered LEP tape with a 75 μm backward-facing step, by comparison, profile drag increased 30% compared to the clean model. Oil visualization of the flow in the boundary layer over the model reveals that local areas of natural transition occur for the tapered LEP tape. Turbulent wedges, initiated by debris trapped in the adhesive and defects in the tape surface, prematurely transition the boundary layer in the plane of the wake probe, increasing profile drag compared to the clean model. Without the presence of the turbulent wedges, natural transition occurs along the span of the model, and the profile drag remains unchanged compared to the clean model.

Using wind tunnel data for the performance of both standard and tapered LEP tapes, the Knox and Braslow method for determination of a critical roughness height for premature boundary-layer transition is modified to develop an analytical model to size the appropriate height of the LEP tape step. The critical roughness Reynolds number required at the height of the tape step to prematurely transition the boundary layer is approximately $\mathrm{Re}_{k,crit} = 200$. The roughness Reynolds number at the top of a 75 μm tape step for a 6-in wide LEP tape is below the critical roughness Reynolds number across the full range of free-stream Reynolds numbers seen along the span of an utility-scale wind turbine blade. This prediction is verified by the local areas of natural transition seen with oil visualization for the tapered LEP tape. The computationally fast Knox and Braslow method can thus be used to correctly size the height of the backward-facing step at the edge of a LEP tape so that it does not trip the boundary layer for a given wind turbine application.

Impact of LEP tapes on Annual Energy Production of a utility-scale 1.5 MW wind turbine was estimated with the wind turbine design and analysis code XTurb-PSU and the 2-D aerodynamic force coefficient data from CFD simulations. An eroded model was also introduced for comparison, which results in the highest AEP loss of 5% compared to a clean rotor configuration. Standard LEP tapes of 350 μm and 500 μm thickness decrease AEP by 2% and 3%, respectively.

Tapered LEP tapes demonstrate no significant change in rotor performance compared to a clean rotor, eliminating losses in Region II seen for standard LEP tapes. The computed 0.7% increase in AEP, all from gains in Region III, small for a pitch-controlled rotor designed to maintain rated power at 1.5 MW. For precisely applied LEP tapes with a 75 μm backward-facing step height, there is no significant impact on AEP of a utility-scale wind turbine. Even for a tape applied with some defects, the trend of change in AEP compared to the average change in profile drag of an airfoil section predicts that the 30% increase in drag measured experimentally reduces AEP by 1%. At half the AEP loss compared to standard LEP tapes, tapered LEP tapes provide a significantly measurable benefit, nearly independent of the quality of the tape application.

In the United States, the average price of electricity is approximately 12.5 cents/kWh as of December 2018 [47]. The AEP loss incurred for eroded blades means roughly \$35,000 in annual revenue loss per 1.5 MW rated wind turbine. With a standard LEP tape applied, blades remain undamaged for longer, but aerodynamic penalties from the backward-facing step at the edge of the tape result in some AEP loss. At half the loss compared to eroded blades, annual revenue loss drops to \$16,800 or \$19,400 per wind turbine for LEP tapes with a 350 μm and 500 μm step height, respectively. For cleanly applied tapered LEP tapes, annual revenue lost per wind turbine is eliminated. Even a 1% AEP loss for incorrectly applied tapered LEP tapes reduces revenue loss to only \$6,400. Tapered LEP tapes, compared to standard LEP tapes currently used today, provide significant monetary benefit for electricity companies that operate wind farms.

Not only do companies see the benefits of the tapered LEP tapes, but reductions in AEP loss means more energy generated per wind turbine. The average annual electricity consumption for a single U.S. household is 10,400 kWh [47]. For a rotor with a standard LEP tape applied, roughly 155,000 kWh of annual energy produced is lost to aerodynamic penalties. By tapering the LEP tape profile to a backward-facing step height that does not prematurely trip the boundary layer, as many as fifteen more households can be powered annually by a single 1.5 MW utility-scale wind turbine.

Improvements in AEP of utility-scale wind turbines by tapering LEP tapes found on most rotors in erosion-prone locations directly impacts achieving the UN Sustainable Development Goal SDG7 [25]. Increasing AEP generated per wind turbine by switching to a novel tapered LEP tape design increases the fraction of global energy provided by wind. Wind farm efficiency improves with AEP improvements by eliminating losses from LEP tape application. These benefits meet two of the three benchmark goals set under SDG7 to achieve prosperous and sustainable living for people and planet.

Before this tape is commercially ready, however, additional wind tunnel testing is required. Tapered LEP tapes tested are difficult to apply to a small section of a rotor blade inside a wind tunnel. The thin edges of the tapered design are prone to wrinkling during application, which caused premature boundary-layer transition in localized areas during initial wind tunnel tests. To address this problem, new prototype tapes are being manufactured with thicker tape edges. The new backward-facing step height will be selected from the results of the Knox and

Braslow critical roughness height calculations such that the roughness Reynolds number is within a safety factor of the critical value for backward-facing steps at the largest free-stream Reynolds number along the span of a utility-scale wind turbine blade. To improve erosion protection lifetime by increasing the width of the region of maximum thickness for the tapered design, the width of the LEP to be marketed will be increased from 6-in to 10-in. To verify that the new designs are comparable to the 500 μm thick prototype tapered LEP tape evaluated in this work, future wind tunnel testing is required.

Preliminary CFD analyses of the finalized tape design to estimate the performance can also be conducted using the model developed in this work for a 6-in tape with a 75 μm backward-facing step. For improved prediction of the transition phenomenon for a backward-facing step, the second iteration of CFD models can include efforts to implement the $\mathrm{Re}_{k,crit}$ transition criterion into the STAR-CCM+ code. Once a method for implementing the critical roughness Reynolds number transition criterion using boundary-layer data extracted from the flow field computed with RANS equations is developed, results can be verified for a known step height that causes premature boundary-layer transition on a wind tunnel model. This work would expand the ability of CFD codes to predict premature transition phenomenon for a wider range of roughness element types.

Once a final design is selected and manufactured that is shown to prevent premature transition of the boundary layer in wind tunnel tests, erosion protection capability of the design must be assessed with rain erosion testing. A successfully designed tapered LEP tape must have a sufficient erosion protection lifetime, in addition to improved aerodynamics, to be competitive with standard LEP tapes in use on utility-scale wind turbine rotors today. Efforts are almost complete to equip The Pennsylvania State University AERTS (Adverse Environment Research Test) facility with rain erosion capabilities. Should the novel tapes demonstrate an erosion protection lifetime comparable to that of a standard LEP tape, significant improvements in rotor performance are achievable by switching to tapered LEP tapes.

Should it prove difficult to improve the application technique for tapered LEP tapes to eliminate the aerodynamic impact of tape defects and adhesive debris, additional studies can be conducted to incorporate the aerodynamic impact of standard LEP tapes into the design of a utility-scale wind turbine rotor. For a given standard LEP tape configuration with known lift and drag performance degradation characteristics, it may be possible to inversely design the rotor to make it less sensitive to premature separation of the boundary layer with better airfoil selection. Using an iterative design process and the capabilities of XTurb-PSU, the spanwise twist and chord distributions as well as the pitch settings can also be optimized to compensate for the lift loss and drag increase observed for standard LEP tapes. Whether by tapering LEP tapes or redesigning the rotor to compensate for standard LEP tape aerodynamic performance degradation, improvement in utility-scale wind turbine rotor performance is achievable. Improved rotor performance increases revenue for wind turbine operating companies and means more available energy generated from wind resources to power homes, directly contributing to advancing globally established goals of achieving sustainable and prosperous living.

Bibliography

[1] Wilcox, B. and E. White (2016) "Computational analysis of insect impingement patterns on wind turbine blades," *Wind Energy*, **19**, pp. 483–495.

[2] Fortin, G. and J. Perron (2009) "Wind Turbine Icing and De-Icing," in *47th AIAA Aerospace Sciences Meeting*, AIAA, Orlando, FL.

[3] Hu, L., X. Zhu, J. Chen, and Z. Du (2017) "Calculation of the Water Droplets Local Collection Efficiency on the Wind Turbines Blade," *Journal of Energy Resources Technology*, **139**.

[4] Castorrini, A., A. Corsini, F. Rispoli, P. Venturini, K. Takizawa, and T. Tezduyar (2016) "Computational analysis of wind-turbine blade rain erosion," *Computers and Fluids*, **141**, pp. 175–183.

[5] Corsini, A., A. Castorrini, E. Morei, F. Rispoli, F. Sciulli, and P. Venturini (2015) "Modeling of Rain Drop Erosion in a Multi-MW Turbine," in *Proceedings of ASME Turbo Expo 2015: Turbine Technical Conference and Exposition*, ASME, Montréal, Canada.

[6] Cortés, E., F. Sanchez, A. O'Carroll, B. Madramany, M. Hardiman, and T. Young (2017) "On the Material Characterisation of Wind Turbine Blade Coatings: The Effect of Interphase Coating-Laminate Adhesion on Rain Erosion Performance," *Materials*, **10**(10).

[7] Gaudern, N. (2014) "A practical study of the aerodynamic impact of wind turbine blade leading edge erosion," *Journal of Physics: Conference Series*, **524**(012031).

[8] Sareen, A., C. A. Sapre, and M. S. Selig (2012) "Effects of Leading-Edge Protection Tape on Wind Turbine Blade Performance," *Wind Engineering*, **36**(5), pp. 525–534.

[9] Schlichting, H. and K. Gersten (2017) *Boundary-Layer Theory*, 9th ed., Springer Berlin Heidelberg.

[10] von Doenhoff, A. and E. Horton (1958) *A Low-Speed Experimental Investigation of the Effect of a Sandpaper Type of Roughness on Boundary-Layer Transition*, *Tech. Rep. NACA-TR-1349*, National Advisory Committee for Aeronautics, Langley Field, Va.

[11] Braslow, A., R. Hicks, and R. Harris (1966) *Use of Grit-Type Boundary-Layer-Transition Trips on Wind-Tunnel Models*, *Tech. Rep. NASA-SP-124*, National Aeronautics and Space Administration, Langley Field, Va.

[12] Soltani, M. R., F. Askari, and V. Sadri (2016) "Roughness and turbulence effects on the aerodynamic efficiency of a wind turbine blade section," *Scientia Iranica*, **23**(3), pp. 927–941.

[13] Soltani, M. R., A. H. Birjandi, and M. Seddighi Moorani (2011) "Effect of surface contamination on the performance of a section of a wind turbine blade," *Scientia Iranica*, **18**(3), pp. 349–357.

[14] Darbandi, M., A. Mohajer, A. Behrouzifar, R. Jalali, and G. Schneider (2014) "Evaluating the effect of blade surface roughness in megawatt wind turbine performance using analytical and numerical approaches," in *International Conference on Heat Transfer, Fluid Mechanics and Thermodynamics*, vol. 37, Journal of Heat Transfer Engineering, Orlando, FL, pp. 800–805.

[15] van Rooij, R. P. J. O. M. and W. A. Timmer (2003) "Roughness Sensitivity Considerations for Thick Rotor Blade Airfoils," *Solar Energy Engineering*, **125**, pp. 468–477.

[16] Wang, Y., R. Hu, and X. Zheng (2017) "Aerodynamic Analysis of an Airfoil With Leading Edge Pitting Erosion," *Journal of Solar Energy Engineering*, **139**.

[17] Schramm, M., H. Rahimi, B. Stoevesandt, and K. Tangager (2017) "The Influence of Eroded Blades on Wind Turbine Performance Using Numerical Simulations," *Energies*, **10**(1420).

[18] Sareen, A., C. A. Sapre, and M. S. Selig (2014) "Effects of leading edge erosion on wind turbine blade performance," *Wind Energy*, **17**, pp. 1531–1542.

[19] Giguère, P. and M. S. Selig (1999) "Aerodynamic Effects of Leading-edge Tape on Aerofoils at Low Reynolds Numbers," *Wind Energy*, **2**, pp. 125–136.

[20] Abbott, I. and A. von Doenhoff (1959) *Theory of Wing Sections, Including a Summary of Airfoil Data*, Dover Publications.

[21] Blasco, P., J. Palacios, and S. Schmitz (2017) "Effect of icing roughness on wind turbine power production," *Wind Energy*, **20**, pp. 601–617.

[22] Oteri, F., R. Baranowski, I. Baring-Gould, and S. Tegen (2017) *2017 State of Wind Development in the United States by Region*, *Tech. Rep. NREL/TP-5000-70738*, National Renewable Energy Laboratory, Golden, CO.

[23] (2017) *Global Wind Report: Annual Market Update 2017*, *Tech. rep.*, Global Wind Energy Council.

[24] IPCC (2014) "Summary for Policymakers," in *Climate Change 2014: Synthesis Report*, World Meteorological Organization, Geneva, SWI, pp. 1–32.

[25] (2017), "Sustainable Development Knowledge Platform," Web.
URL `http://sustainabledevelopment.un.org`

[26] Duncan, J. (2016), "Rhode Island offshore wind farm, first in the U.S., to power thousands of homes." web.

[27] Shohag, M., E. Hammel, D. Olawale, and O. Okoli (2017) "Damage mitigation techniques in wind turbine blades: A review," *Wind Engineering*, **41**(3), pp. 185–210.

[28] Ehrmann, R. S., E. B. White, D. C. Maniaci, R. Chow, C. M. Langel, and C. P. van Dam (2013) "Realistic Leading-Edge Roughness Effects on Airfoil Performance," in *Fluid Dynamics and Co-located Conferences*, AIAA, San Diego, CA.

[29] Kim, S. D. and D. J. Song (2005) "Computations of Droplet Impingement on Airfoils in Two-Phase Flow," *Journal of Mechanical Science and Technology*, **19**(12), pp. 2312–2320.

[30] Braslow, A. and E. Knox (1958) *Simplified Method for Determination of Critical Height of Distributed Roughness Particles for Boundary-Layer Transition at Mach Numbers from 0 to 5*, *Tech. Rep. NACA-TN-4363*, National Advisory Committee for Aeronautics, Langley Field, Va.

[31] H.M. Slot, E. G., C. Rentrop, and E. van der Heide (2015) "Leading edge erosion of coated wind turbine blades: Review of coating life models," *Renewable Energy*, **80**, pp. 837–848.

[32] Valaker, E. A., S. Armada, and S. Wilson (2015) "Droplet Erosion Protection Coatings for Offshore Wind Turbine Blades," *Energy Procedia*, **80**, pp. 263–275.

[33] (2016) *3M^{TM}Wind Protection Tape 2.0 W8750 Technical Bulletin*, *Tech. rep.*, 3M Renewable Energy Division.

[34] (2014) *3M^{TM}Wind Blade Protection Coating 4600*, *Tech. rep.*, 3M Renewable Energy Division.

[35] Siemens (2017) "Siemens PLM Software: Simcenter STAR-CCM+," .

[36] Ren, K., J. Hu, X. Xiong, L. Zhang, and J. Wei (2009) "Validation of Turbulence Models in STAR-CCM+ by N.A.C.A. 23012 Airfoil Characteristics," in *2009 ASEE Northeast Section Conference*, Bridgeport, CT, USA.

[37] Langtry, R. and F. Menter (2005) "Transition Modeling for General CFD Applications in Aeronautics." *AIAA*, (AIAA-2005-552).

[38] Menter, F., R. Langtry, S. Likki, Y. Suzen, P. Huang, and S. Volker (2006) "A Correlation-Based Transition Model Using Local Variables - Part I: Model Formulation." *Journal of Turbomachinery*, **128**, pp. 413 – 422.

[39] Pope, A. and J. Harper (1966) *Low-Speed Wind Tunnel Testing*, John Wiley & Sons, Inc.

[40] Maskell, E. (1965) *A Theory of the Blockage Effects on Bluff Bodies and Stalled Wings in a Closed Wind Tunnel*, *Tech. Rep. R&M-3400*, Ministry of Aviation.

[41] Allen, H. and W. Vincenti (1944) *Wall Interference in a Two-Dimensional-Flow Wind Tunnel, With Consideration of the Effect of Compressibility*, *Tech. Rep. NACA/TR-782*, National Advisory Committee for Aeronautics.

[42] Parkhurst, R. and D. Holder (1965) *Wind-Tunnel Technique*, Sir Isaac Pitman & Sons, Ltd.

[43] 3M (2019), "3M(TM) Wind Blade Protection Tape W8607," .
URL `https://www.3m.com/3M/en_US/company-us/all-3m-products/~/3M-TM-Wind-Blade-Protection-Tape-W8607-Colorless-Splice-Free-Poly-Liner-10-in-x-36-yd-1-per-case/?N=5002385+4294876526rt=d`

[44] Schmitz, S. (2012), "XTurb PSU: a wind turbine design and analysis tool," The Pennsylvania State University.

[45] Moriarty, P. and A. Hansen (2005) *Aerodyn Theory Manual*, *Tech. Rep. NREL/TP-500-36881*, National Renewable Energy Laboratory, Golden, CO.

[46] Dowler, J. and S. Schmitz (2017) "A solution-based stall delay model for horizontal-axis wind turbines." *Wind Energy*, **18**(10), pp. 1793 – 1813.

[47] (2019) *Electric Power Monthly: with Data for December 2018*, *Tech. rep.*, U.S. Energy Information Administration.